USCIPI REPORT #920

Improved Computer-Generated Holograms for Optical Filtering

by

Chung-Kai Hsueh

October 1979

Signal and Image Processing Institute
UNIVERSITY OF SOUTHERN CALIFORNIA
Department of Electrical Engineering-Systems
3740 McClintock Avenue, Room 404
Los Angeles, CA 90089-2564 U.S.A.

ACKNOWLEDGEMENTS

I am indebted to Dr. Alexander A. Sawchuk, my thesis advisor, for his support and guidance throughout the course of this work. I am deeply grateful to Dr. Tim C. Strand for his many helpful discussions and suggestions. Without his help some experimental work may not have been completed. I also appreciate Dr. Dennis R. Estes for serving as a member in my dissertation committee.

I would like to thank the staff of the Image Processing Laboratory, especially Mr. Ray R. Schmidt, for their help in using image processing equipment. The excellent typing of this manuscript by Ms. Amy Yiu is also appreciated.

TABLE OF CONTENTS

APPENDICES

LIST OF FIGURES

LIST OF TABLES

ABSTRACT

Several improvements in computer-generated holograms (CGH) are presented. Among these are a phase coding technique, a new type of binary hologram and a way of making continuous holograms. Emphasis is given to holograms that are used in a filtering system with a large input format.

CGH's are widely used in optical filtering systems. However, due to the sampled nature of the CGH, several diffraction orders occur in the output plane. This may result in overlapping of different orders in the output plane if the size of the input object is large. This problem can be avoided by sampling the filter at a rate determined by the sum of the input size and the impulse response size. This is essentially an oversampling in the transform domain. To eliminate the need for oversampling we describe a way of making continuous holograms. Two binary patterns corresponding to the amplitude and phase parts of the Fourier transform are made according to the sampling rate determined by the extent of the impulse response. These two patterns are low-pass filtered and recorded on color film by using illuminations of different

colors. A complex-valued hologram is thus made. Pure amplitude or pure phase holograms can be made in a similar manner. This hologram reconstructs only a single order. When used as a filter, the limitation on the input size is therefore eliminated. However due to the non-ideal interpolation, background noise and some high order artifacts are present.

The oversampling problem can also be alleviated by using two other methods described in this thesis. They are the cell size expansion method and hologram interpolation with the discrete Fourier transform (DFT). The cell size expansion method reduces the intensity at the high orders but works only for small impulse responses. Hologram interpolation with the DFT increases the separation of different orders and therefore allow a larger input format. A correct procedure for doing interpolation by the DFT is presented.

Binary holograms have the advantages of easy fabrication and high signal-to-noise ratio. A new binary hologram called the double-phase hologram (DPH) is described. In one of the configurations, the reconstruction appears further away from the central bright spot. It is therefore more suitable than other binary holograms for a filtering system with a large input format although the efficiency is lower.

Phase coding methods and their effects are also studied. When the hologram is used for reconstructing an image or is used in an incoherent system, only the intensity is of concern. The phase of the impulse response can be manipulated in order to reduce the dynamic range of the Fourier transform. However due to the use of the DFT in making the hologram, the phase coding increases the aliasing errors and the impulse response has speckle-like noise. An iterative phase coding method is described which uses constrained bandwidth and discards the high frequency components. This method is capable of reducing the speckle-like noise while the dynamic range is also considerably reduced.

To demonstrate the application of CGH's, a character recognition system is presented. The phase-only matched filter is shown to be better than the matched filter in both efficiency and discrimination power. The phase-only matched filters are implemented by both the sampled kinoform method and continuous kinoform method. Experimental results are shown.

CHAPTER 1

INTRODUCTION

Optical signal processing offers the advantages of inexpensive, fast parallel processing of two-dimensional signals [1-1]. In contrast to digital processing, optical signal processing avoids the expense of scanning, serial processing by large digital computers and serial display. However, optical processing is also limited by its slow input-output and the restricted choice of linear operations such as convolution, correlation and Fourier transformation. The precision and dynamic range are also reduced compared with digital processing. Recent advances have been made towards extending these capabilities. Electrically or optically controlled real-time input transducers are being developed [1-2] and general nonlinear operations are available [1-3,1-4]. Most recently some simple space-variant processing techniques have also been proposed [1-5]. Although the precision of optical processing can never reach that of the digital computer, lower precision is sometimes acceptable especially with data intended for the human observer.

A major step towards extending the usefulness of optical processing has been the use of the computer in making holograms or filters. Using a computer, a hologram or filter can be made without a physical specimen of the impulse response. Compensation for nonlinear film effects, finite cell size and other flexibility is possible. In Section 1.1 we first review some previous methods of making computer-generated holograms and their applications. Some problems associated with the computer-generated holograms when used in a filtering system are discussed in Section 1.2. Finally in Section 1.3 we given an overview of this thesis and summarize the contributions.

1.1 Review of previous computer-generated holograms and their applications

1.1.1 Computer-generated holograms

The most straightforward computer-generated hologram is a simple simulation of interferometrically generated holograms. We compute the wave $H(u,v)=A(u,v)\exp(j\theta(u,v))$ due to the object and add a reference wave $R(u,v)$ to it. The squared modulus of this sum is then plotted on the film or plate. If the reference wave is a plane wave $B\exp(jbu)$ then the function to be recorded is

$$I(u,v) = A^2(u,v)+B^2+2BA(u,v)\cos(bu-\theta(u,v)). \qquad (1\text{-}1)$$

Physically, the sole purpose of the first two terms is a bias to make I(u,v) non-negative. Some modifications of this method are possible. Burch [1-6] suggested the use of a constant to replace the first two terms so that the noise component is a plane wave. Huang and Prasada [1-7] used the expression

$$I(u,v) = 2BA(u,v)+2BA(u,v)\cos(bu-\theta(u,v)). \qquad (1-2)$$

to make a hologram. This method makes the fringe contrast higher than the other two methods. These methods need a large amount of computation and require a large number of resolution points to encode the high frequency interference fringes and are not attractive.

The flexibility of the computer calculation allows other methods for making holograms. Among these methods, the binary detour-phase hologram of Lohmann [1-8,1-9] is the most popular one. This hologram has the advantages of easy synthesis and high signal-to-noise ratio due to its binary transmittance. The Lohmann hologram consists of an array of Fourier component cells. In each cell a transparent slit on an opaque background represents the value of the Fourier component. The amplitude is determined by the area of the slit while the phase is determined by the position of the slit (the detour-phase

effect). Upon illumination the reconstruction appears at the first diffraction order and therefore has low light efficiency. Another disadvantage of the Lohmann hologram is the use of many resolution points in representing a Fourier component. Lee [1-10] has used four non-negative quantities ($\pm$ real, $\pm$ imaginary) to represent each Fourier component. If each resolution point is allowed to have a variable grey level then only four resolution points per Fourier component are required. Binary implementation of the Lee Hologram is also possible, although this requires more resolution points. A simplified version of the Lee hologram that uses three components along the directions of angle 0, $2\pi/3$, $-2\pi/3$ to represent each Fourier component was described by Burckhardt [1-11]. Chavel and Hugonin [1-12] have proposed a binary hologram which also consists of three apertures per cell. They use three Fast Fourier Transforms (FFT's) to compute the value at the center of each aperture. True phases are therefore obtained and the quality of the reconstruction is improved. There are many ways to encode these three apertures in each cell. Different methods affect the complexity of the computation and the hologram efficiency. The appearance of the zero order reconstruction is also changed by these different methods while the first order remains the same. The same algorithm can be applied to binary holograms with more than

three apertures per cell.

Other binary detour-phase holograms have been proposed. Haskell and Culver [1-13] have used two equal size apertures per cell to represent each Fourier component. Their implementation may result in the overlap of the two apertures. Although this problem can be avoided by limiting the size of the apertures and the minimum distance between them, diffraction efficiency and dynamic range are reduced. Haskell [1-14] also proposed a hologram with 8x8 subcells per Fourier component. By appropriately controlling the opening of these subcells, a desired complex value can be obtained with less quantization error than the Lohmann hologram. These methods are more efficient in using the space-bandwidth of the hologram than the Lohmann approach.

Recently Allebach and Keegan [1-15] have described a binary hologram using ordered dither. They applied this method to encoding binary Lee holograms. Instead of assigning a block of resolution points to each quadrature component, they computed the Fourier transform at each resolution point and compared the appropriate quadrature component with a position-dependent threshold in order to determine the on/off state at that point. This method has been shown to reduce the error due to the binary

approximation of an analog signal.

Off-axis holograms have the main disadvantage of low light efficiency. On the other hand, on-axis holograms have their reconstruction at the zero order and have high efficiency. On-axis holograms also have smaller space-bandwidth requirements than binary holograms. The simplest on-axis hologram is a phase only hologram called the kinoform [1-16]. When the object is well diffused, the Fourier spectrum is approximately constant and can be discarded without significant degradation in the reconstruction [1-17]. Therefore only the phase pattern is exposed on the film and then bleached to produce the pure phase effect. Due to the lack of amplitude information minor degradations still occur. Other on-axis holograms which use phase-only material are the parity sequence hologram [1-18] and synthetic coefficient hologram [1-19]. Both methods use a parity term to level the spectrum and therefore have constant amplitude. These two methods are different in the arrangement of the components. The parity sequence hologram has the reconstruction interlaced with a noise term and is primarily used as a holographic memory. The synthetic coefficient hologram on the other hand has noise terms appearing off-axis.

The method which comes closest to total complex value control is the Referenceless On-Axis Complex Hologram (ROACH) [1-20]. The ROACH uses the wavelength-dependent absorbing and phase-shifting property of ordinary multiemulsion color film to synthesize a complex value transparency. Amplitude and phase can be controlled independently with some precompensation for cross talk. Although the color film has a low space-bandwidth product, it is satisfactory for an on-axis hologram.

1.1.2 Applications

The ability of the computer-generated hologram to reconstruct a wavefront enables us to use it for display purposes. Three-dimensional objects can also be reconstructed by computer-generated holograms [1-21, 1-22]. These techniques are also very valuable in acoustical and microwave holography. Color images can be obtained by making three separate holograms for red, green and blue and combining their reconstructions [1-23].

A unique application of the computer-generated hologram is in optical surface testing. A computer-generated hologram is made of a standard wavefront calculated in the computer. Errors of the optical element can be detected by observing the interference pattern between the reconstructed wavefront and the wavefront from

the surface under test [1-24]. In fact computer-generated holograms can be used as optical elements themselves. These include computer-generated Fresnel lenses, diffraction gratings, zone plates and diffusers.

Due to the ability to synthesize complex valued functions, computer-generated holograms can be used as spatial filters in optical filtering systems. The computer-generated hologram provides more flexibility than optically generated holograms in designing complex pupil functions. These filters have been widely used in image enhancement [1-25], matched filtering [1-8], code translation [1-26] and image restoration [1-27].

Another possible use of computer-generated holograms is for holographic memories [1-28, 1-29]. They have the advantages of high storage density and quick accessibility due to the parallel processing nature of optics.

1.2 Problems with computer-generated holograms when used in filtering systems

When a transparency recorded with holographic information is used for reconstruction purposes, the transparency is called a hologram. The reconstruction is called the object or image. However when the same transparency is used in the frequency domain of a filtering

system, we called it a filter while the reconstruction is called the impulse response. In the following discussion and throughout this thesis, the terms "object," "image" and "impulse response" will be used interchangeably depending on the particular application. The usage should be clear from the context. The terms "hologram" and "filter" will be used in a similar way.

When making a computer-generated hologram (or filter) let us assume that the continuous Fourier transform of the impulse response is available. The continuous Fourier transform is sampled at finite number of points and then recorded on the film according to one of the methods we discussed in Section 1.1.1. The sampling interval D is determined by the extent X_n of the impulse response and is given by

$$D < \frac{1}{X_n} \tag{1-3}$$

according to the sampling theorem [1-30]. Here we have neglected any constant factor associated with the particular set-up. When reconstructed the impulse response has an extent X_n with the distance between adjacent orders given by

$$X = \frac{1}{D} > X_n \quad . \tag{1-4}$$

Therefore different orders do not overlap assuming no

orders have an extent larger than X_n. The appearance of different orders varies depending on the particular method we use although the separation of these orders are all the same. When this filter is used in a filtering system, the output is the above reconstruction convolved with the input. Due to the presence of other undesired orders overlapping may occur. If the filter is made by using the detour-phase technique, the desired response appears at the first diffraction order, adjacent to the central bright spot. The proximity of the central bright order can be a serious problem. For an on-axis filter the desired order is the zero order and the other orders are attenuated by a sinc function due to the finite cell size. The overlapping problem is less severe but is not negligible in general unless the high orders can be further suppressed.

When the high orders are non-negligible and the input has a spatial extent of X_0, then we need a sampling interval of

$$D < \frac{1}{X_n+X_0} \tag{1-5}$$

in order to avoid any overlap of different orders in the filtered result. Generally X_n is much smaller than X_0 and therefore the condition becomes

$$D < \frac{1}{X_0} \quad . \tag{1-6}$$

The sampling interval is then determined by the extent of the input rather than by the impulse response. This is essentially an oversampling in the transform domain. The complexity of making computer-generated holograms (filters) is thereby increased. This problem can be alleviated by using a two-step method [1-31, 1-32]. In this method a computer-generated hologram is made at the sampling interval determined by the impulse response. The desired order of the reconstruction is then selected and interfered with a separately generated reference wave. A desired filter with a high carrier frequency is thus recorded optically. Bartelt et al. [1-33] developed a technique that uses a step-and-repeat camera to replicate a binary hologram in order to increase the carrier frequency of the filter. Yatagai [1-34] has described an interpolation method to achieve the same goal.

At the beginning of this section we assumed that a continuous Fourier transform was available and the continuous Fourier transform was sampled in order to make a computer-generated hologram (filter). In reality we actually have an array of points representing the impulse response. This is either an artificial impulse response (object) or a sampled real object. The Fourier transform components are then computed by using the discrete Fourier

transform (DFT).

The use of the DFT assumes the given array as a periodic function. Therefore what we actually have are the sampled values of an aliased version of the continuous Fourier transform [1-35]. The reconstruction obtained from the hologram thus made only has correct values at the sampling points. Between the sampling points the intensity varies and appears as speckle noise. When phase coding [1-36, 1-37] is used this noise becomes worse. This problem is of interest when the filtering operation is smooth in nature such as the cubic B-spline interpolation over an array of discrete data. Aliasing error and its reduction have been studied by Allebach et al. [1-35].

1.3 Overview of the thesis and summary of contributions

In applications where the intensity of the reconstruction is the only concern, phase coding is usually applied in order to reduce the dynamic range in the Fourier transform plane. In Chapter 2 we review different phase coding methods and discuss problems associated with phase coding. Although the phase coding reduces the dynamic range in the transform plane and therefore reduces the quantization error and increases the efficiency of the hologram, aliasing errors occur due to the use of the DFT in computation. Iterative phase coding methods with

constrained bandwidth [1-35] are employed to reduce the aliasing error at the expense of lower efficiency. A modified method which also uses constrained bandwidth but discards the high frequency components is proven to be better. Computer simulations of the effects of different phase coding methods on the reconstruction and filtering are performed.

In Chapter 3 we introduce a new way of making binary holograms. Instead of decomposing each component in the Fourier plane into four or three non-negative quantities as in the Lee hologram [1-10] or Burckhardt hologram [1-11], we decompose each Fourier component into two phase quantities. These phase quantities are implemented by the detour-phase method [1-9]. This new binary hologram is called the double-phase hologram (DPH) [1-38]. A consequence of the DPH method is a parity term which produces noise in the reconstruction. This error can be either reduced by using more subcells or eliminated by using the value calculated from the center of each subcell rather than the center of the overall cell. The reconstruction is either at (0,1) order or a higher order (n,1) when 2n subcells are used. The one at (0,1) order has better efficiency and a better signal-to-noise ratio. However the one at the higher order is further away from the central bright spot and is more suitable for a

filtering system with a large input format.

Although the binary hologram is easy to make and has the advantage of a large signal-to-noise ratio, it works off-axis and has low light efficiency. Furthermore the binary hologram needs more resolution points to represent a Fourier component and requires a large space-bandwidth product for the plotter and recording medium. The on-axis hologram, on the other hand, reconstructs at the zero order (0,0) and has better efficiency. Each Fourier component can be represented by one resolution point and is more efficient in using the limited space-bandwidth product of the plotter and recording material. In Chapter 4 we discuss the on-axis hologram and its use in filtering. Due to the finite cell size, the high orders are attenuated. This is a desired property since ideally we want only one order present in the filtering system. However the high orders are still not negligible and might create overlap problems in the filtering output. Two methods are discussed in Chapter 4 to either reduce the high orders further or move them further away from the zero order. The cell size expansion method effectively expands the cell size without affecting the actual resolution size. The high order is reduced considerably while the desired order is also distorted. By compensating for the distortion we also increase the high orders again. Therefore this method

works only for a small impulse response. Another method uses the shift property of the Fourier transform to perform interpolation [1-12, 1-34] and increases the separation of the orders. The correct interpolation procedure is presented. It is shown that this interpolation is indeed a sinc interpolation assuming that the function is periodic. This method is shown to be more economical when other intermediate processing, such as phase coding, is required.

In Chapter 5 we introduce a method of making continuous holograms. This method is capable of making a complex hologram, amplitude-only hologram, or phase-only hologram. As an example a continuous ROACH is made on Kodachrome 64 film. Two binary patterns, one for amplitude and one for phase control are made. These patterns are illuminated by different wavelengths, spatially low-pass filtered and then recorded on the color film. Calibration procedures are also discussed. This method essentially performs sinc interpolation on the sampled amplitude and phase quantities separately rather than on the complex value, therefore the result is non-ideal. The hologram reconstructs only a single order. However due to the non-ideal interpolation, background noise and some high order dots are also present.

A character recognition problem is presented in Chapter 6. We found that the phase-only matched filter performs better than the matched filter. It has the advantages of high efficiency and better response. The phase-only matched filter is also easier to make. The effects of quantization, phase mismatch and phase coding are also studied. These effects are found to be minor. The phase-only matched filters are implemented by a sampled kinoform and a continuous kinoform. The experimental results are shown.

In Chapter 7 we summarize the conclusions and make suggestions for future work.

CHAPTER 2

PHASE CODING

The large dynamic range of the Fourier transform of a zero phase object always presents a problem in holography due to the limited dynamic range available on the recording medium. In many applications only the intensity of the reconstruction is of interest, for example, when reconstructing an image or when the hologram is used as a filter in an incoherent system. Therefore the phase of the object (or the impulse response if the hologram is used as a filter) can be chosen to shape the Fourier transform spectrum in order to match the characteristics of the recording medium better. Different phase coding methods have been used for this purpose. However due to the use of the DFT in computing the Fourier transform, the phase coding increases the aliasing error [2-1] and therefore produces speckle-like noise. In this chapter we will review different phase coding methods. Then we will explain how the speckle-like noise is produced and discuss methods of suppressing this noise. Cubic B-spline interpolation of an array of data points will be used to

demonstrate the problem of noise and the effects of different phase coding methods.

2.1 Review of phase coding methods

In conventional holography, holograms have been made by using a diffuser in order to distribute the energy over the whole recording plane and therefore reduce the dynamic range [2-2,2-3]. In digital holography, this can be done by assigning random phases to the given object array. Deterministic phase codes [2-4] can also be used for this purpose. The random phase code does not necessarily produce a very uniform spectrum and also produces severe aliasing errors as will be explained in the next section. The deterministic phase codes generally produce noise-like artifacts [2-5] and may look more noisy to a human observer than the random phase coded images.

In addition to random phase codes and deterministic phase codes, other iterative methods [2-6 to 2-13] can also be applied to phase coding. In general, these iterative methods are more flexible and give better control of the Fourier spectrum. This is also an advantage of digital holography since there is no counterpart of these methods in conventional holography. The basic idea of the iterative phase coding methods is to modify the phase of the object (or even the amplitude in some cases) so that

the spectrum is close to the desired one while the reconstruction is the ideal object. This problem is very closely related to another problem called phase retrieval. The phase retrieval problem has occurred in many areas such as speckle interferometry [2-14] and electron microscopy [2-8]. In all these problems, either the moduli in the space and transform domains are available or only one of them is available with some constraints. The goal is to find the phase in one domain and therefore in the other domain through the Fourier transform relationship. In general the solution of phase retrieval is not unique. When applying these methods to phase coding, the solution may not even exist at all. For instance, given a uniform spectrum (kinoform) the solution does not exist except for some trivial cases. However since these iterative methods converge [2-8, 2-15] we can either set the spectrum to a constant when the fluctuation of the spectrum is small and get an approximate result or allow small variation in the Fourier transform. Therefore the existence and uniqueness of the solution in the iterative methods are not of great concern to the phase coding as long as the methods converge.

Here we will divide these iterative phase coding methods into three categories:

(1) Space-transform iterative phase coding method [2-6, 2-7, 2-8].

(2) Input-output approach [2-9, 2-10, 2-11].

(3) Gradient search method [2-12, 2-13].

The block diagram of the first method is shown in Fig. 2.1. We first assign a random phase ϕ to the ideal object h and get $he^{j\phi}$. A Fourier transform is performed by using the FFT to obtain $He^{j\theta}$. Then the Fourier spectrum H is modified to an ideal spectrum H' (in the case of a kinoform we have H'=constant). Then we perform the inverse Fourier transform to obtain $h'e^{j\phi}$, where ϕ is different from the original phase ϕ. In general h' is different from h and therefore we change h' to h and repeat the procedure again. Besides changing the spectrum we can also include the phase quantization in the loop [2-7]. This method has been shown to be convergent [2-8, 2-15]. The procedure stops when the error criterion is satisfied or the number of iterations exceeds a certain limit. The error at each iteration can be either computed in the space domain or the transform domain. This method does much better than random phase codes in spectrum shaping. Gallagher and Sweeney [2-16] have compared the probability density of the spectral magnitude and the dynamic range of the spectra for random phase coded and iterative phase coded objects. The result shows that the iterative phase coding gives more uniform

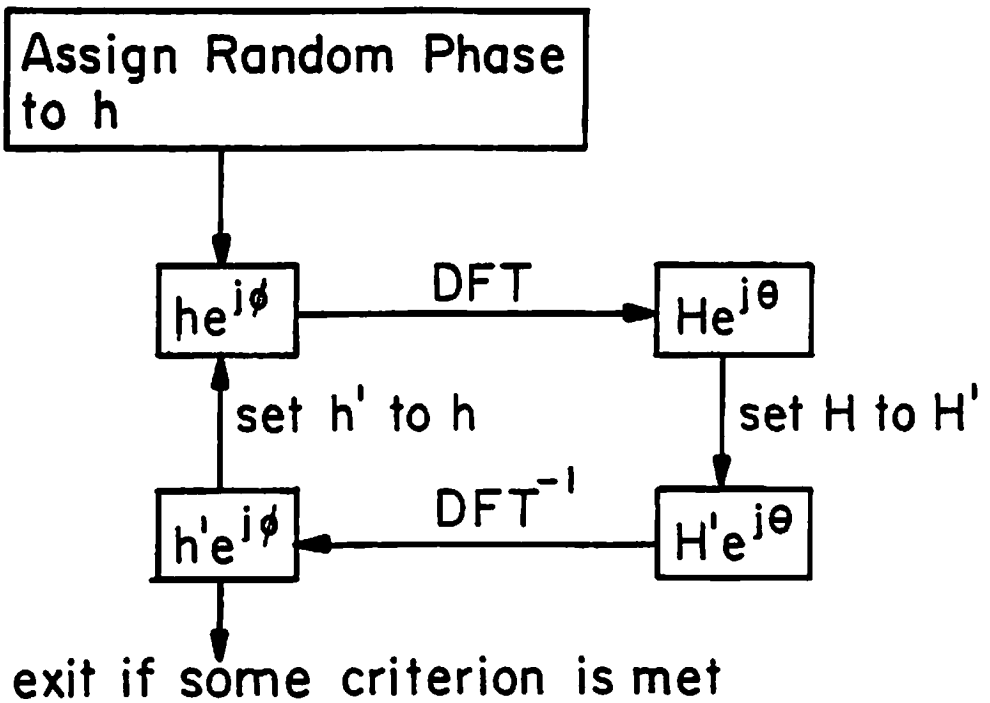

Fig. 2.1 Space-transform iterative phase coding

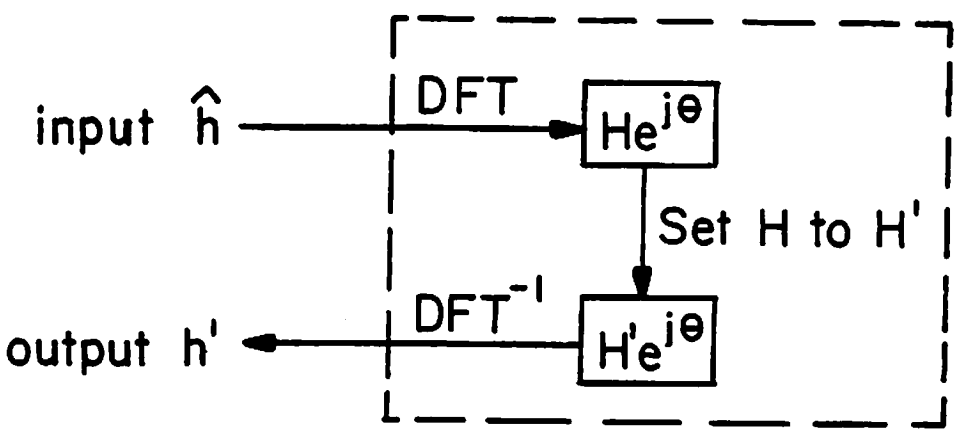

Fig. 2.2 Input-output approach

distribution and lower dynamic range.

The input-output approach also uses the Fourier transform relationship, however, it considers the process as a nonlinear system with $\hat{h}$ and h' as the input and output respectively as shown in Fig. 2.2. Fienup [2-9] has found in the study of the space-transform iterative method that although the method converges very fast at the beginning, it tends to stabilize at a certain minimum value due to the fact that the error at some points fail to decrease as the number of iterations increases. Instead of just modifying the phase of the input and setting $\hat{h}$ equal h at each iteration, in the input-output approach, Fienup also modifies the input amplitude $\hat{h}$ in order to optimize the output h' so that it is close to the desired object h. This method has been proved to converge faster. A modified method with constraints in the space domain has also been applied to interferometer data obtained from large telescopes in order to reconstruct a high resolution image [2-11].

The third method uses the technique in nonlinear programming [2-17] to optimize the result. Allebach and Liu [2-12] use the Fletcher-Powell algorithm to minimize the maximum of the Fourier spectrum with a bandwidth constraint. Gonsalves [2-13] assumes the phase to be a

polynomial with unknown parameters in a phase retrieval problem. A metric function is formed which measures the difference of autocorrelations obtained from the ideal Fourier transform and the computed Fourier transform. The Fletcher-Powell algorithm is used to adjust the parameters until the metric function is minimized.

The iterative phase coding methods are much more time consuming than random phase coding and deterministic phase coding. However they can generate phase codes which produce a more desirable spectrum. For example, to obtain a kinoform, iterative phase coding method is more effective than random phase codes. The spectrum thus obtained is more uniform and has a lower dynamic range.

2.2 Phase coding noise and its reduction

2.2.1 Speckle-like noise

Different phase coding methods have successfully reduced the dynamic range in the Fourier transform domain. However due to the use of the DFT we only obtain the sampled values of an aliased version of the continuous Fourier transform of the object [2-1]. The reconstruction obtained from the hologram thus made will only have correct values at the sampling points. Between the sampling points the intensity varies and appears similar to speckle noise.

For some applications, such as holographic memories, only the sampling points are to be detected and this noise does not cause any problem. However in many other applications, it is desirable to have the correct reconstruction throughout the spatial domain.

To illustrate how the speckle-like noise occurs [2-18], let us consider an object coded with some phase coding method (for example, random phase). The reconstruction is identical to the original object only at the sampling points due to the use of the DFT. The reconstruction is composed of the sampling points convolved with a sinc function. Due to the use of phase coding, two adjacent points will have different phases in general. In the extreme case, they may have a phase difference of π. The intensity values between these two points are influenced mostly by these two points and deviate considerably from the desired ones.

Figure 2.3(a) shows a desired object and its sampled version. A possible reconstruction in amplitude after phase coding is shown in Fig. 2.3(b). For simplicity and easier illustration we have assumed phases of 0 or π and linear interpolation is used rather than sinc interpolation. The intensity is shown in Fig. 2.3(c) which is the magnitude squared of Fig. 2.3(b). It is obvious

(a) desired object

(b) reconstruction in amplitude

(c) reconstruction in intensity

Fig. 2.3 Effect of phase coding

that the intensity of the reconstruction is different from the ideal object. If the hologram is used as a filter in an incoherent processing system, Fig. 2.3(c) is exactly the impulse response of the system. If we consider the incoherent input as an array of uncorrelated point sources, then the output is the convolution of the point sources with the degraded impulse response. Although there may be some smoothing due to the incoherent summation of the weighted impulse responses, the degradation may remain.

It is well known that the aliasing error can be reduced by using a higher sampling rate. However, this is not true when random phase codes are used. It has been shown [2-19] that when an object is coded with random phase the bandwidth increases with the sampling rate. Therefore, aliasing error does not decrease by using more sampling points and some other methods are required for noise suppression.

2.2.2 Reduction of noise

To reduce the speckle-like noise in the case of random phase coding, it is possible to reduce the range of the random phase distribution at the expense of increasing dynamic range. Fienup [2-5] has proposed a Checkerboard Real-Imaginary Phase code (CRIP) which consists of a checkerboard pattern of ± 1 (pure real) and $\pm j$ ($j=\sqrt{-1}$, pure

imaginary) where the signs are chosen quasi-randomly. This is based on the observation that when considering only two adjacent points of the same amplitude, the sinc interpolation will have a more uniform curve in between these sample points when these two points have a phase difference of $\pi/2$. The contribution from other points can be reduced by using an appropriate weighting function, such as a Gaussian function, at the hologram plane. Comparing with the random phase code with a reduced distribution range, this method is found to be more favorable in terms of noise reduction and efficiency.

Since the noise is the result of aliasing, it is reasonable to believe that we can reduce this noise by properly changing the shape of the spectrum. Iterative methods seem to be the only way to achieve this. Basically all three of the iterative methods discussed in Section 2.1 can be used for this purpose. Here we only consider the space-transform iterative phase coding method since it is the easiest to perform.

The space-transform iterative phase coding method with a constant spectrum in the transform domain can be used to reduce the dynamic range effectively. However the phase thus produced still looks random and the aliasing error is severe. Instead of using a constant spectrum, Allebach et

al. [2-1] have constrained the bandwidth so that the aliasing error is significantly reduced at the expense of lower efficiency. This method can be modified as follows [2-18]. Suppose we are to make a hologram with a bandwidth of W. Then instead of using an ideal bandwidth of W directly in the iterative method, we use a spectrum of width 2W with the bandwidth constrained to W as shown in Fig. 2.4(a). After several iterations the actual spectrum may converge to the one shown in Fig. 2.4(b). Although the bandwidth is about the same as when we use the constant spectrum of width W in the iterative method, the aliasing error is expected to be reduced through the manipulation of the high frequency components beyond the bandwidth W. Then we can use the central part of the spectrum shown in Fig. 2.4(b) in making the hologram or filter. By doing this we have thrown away some high frequency components. However these high frequency components are small and can be neglected without severe degradation in the reconstruction. Furthermore the aliasing errors are mostly contained in the high frequency region and the speckle-like noise may be reduced by discarding these high frequency components. Therefore this modification not only reduces the aliasing error but also preserves the light efficiency. The computation time is increased since we are using a larger array in the iterative method while the plotting

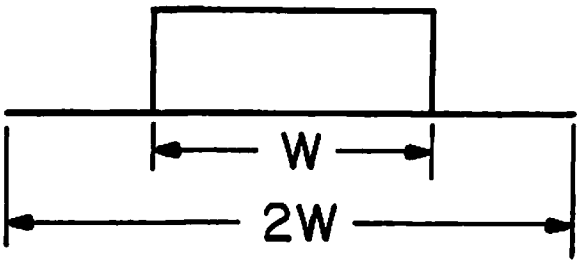

(a) ideal spectrum

(b) resulting spectrum

Fig. 2.4 Modified space-transform iterative phase coding with constrained bandwidth

complexity remains the same.

This modification can also be applied when the other two iterative phase coding methods are used. In the next section we will use examples to illustrate the problem of speckle-like noise and to examine the effects of different phase coding methods in reducing this noise while maintaining the light efficiency.

2.3 Computer simulations

2.3.1 Description of the simulation

Here we will examine the effects of different phase coding methods on the reconstruction (or the impulse response) of a computer-generated hologram and even more importantly on the filtering result when the hologram is used as a filter. Since the speckle-like noise looks grainy, the function we choose for this test should be smooth in order to see this effect easily. The particular example we use here is the cubic B-spline interpolation [2-20, 2-21, 2-22]. For simplicity only one-dimensional examples are given.

The cubic B-spline function s(x) is shown in Fig. 2.5 and it is equal to the self-convolution of four rect($\frac{x}{\Delta}$) functions or two $\Lambda(\frac{x}{\Delta})$ functions as expressed by

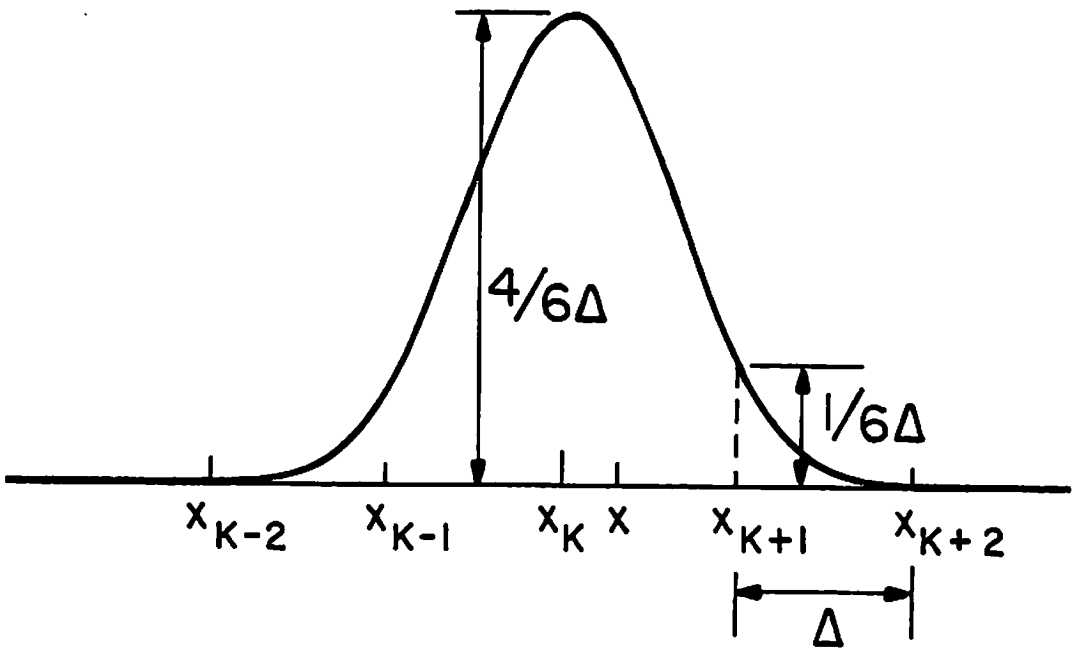

Fig. 2.5 Cubic B-spline function

$$s(x) = \text{rect}(\frac{x}{\Delta}) * \text{rect}(\frac{x}{\Delta}) * \text{rect}(\frac{x}{\Delta}) * \text{rect}(\frac{x}{\Delta}) \qquad (2\text{-}1)$$
$$= \Lambda(\frac{x}{\Delta}) * \Lambda(\frac{x}{\Delta})$$

where

$$\text{rect}(\frac{x}{\Delta}) = \begin{cases} 1 & |x| \leq \Delta/2 \\ 0 & \text{otherwise,} \end{cases} \qquad (2\text{-}2)$$

$$\Lambda(\frac{x}{\Delta}) = \text{rect}(\frac{x}{\Delta}) * \text{rect}(\frac{x}{\Delta}) \qquad (2\text{-}3)$$

and * denotes convolution. The cubic B-spline function can also be represented by cubic polynomial as follows

$$s(x) = \frac{1}{6\Delta^4}[(x-x_{K-2})_+^3 - 4(x-x_{K-1})_+^3 + 6(x-x_K)_+^3 - 4(x-x_{K+1})_+^3 + (x-x_{K+2})_+^3] \qquad (2\text{-}4)$$

where the x_i's are the nodes of the data points with even spacing Δ as shown in Fig. 2.5 and $(x-x_i)_+^3$ is defined by

$$(x-x_i)_+^3 = \begin{cases} (x-x_i)^3 & \text{if } x \geq x_i \\ 0 & \text{otherwise.} \end{cases} \qquad (2\text{-}5)$$

A one-dimensional cubic B-spline interpolation problem can be stated as following: given a one-dimensional data array g_i, i=1,...,N, we are to find another one-dimensional data array c_i, i=1,...,N, such that the convolution of the c_i's with the cubic B-spline function gives the original value g_i at the nodes. The interpolation values between

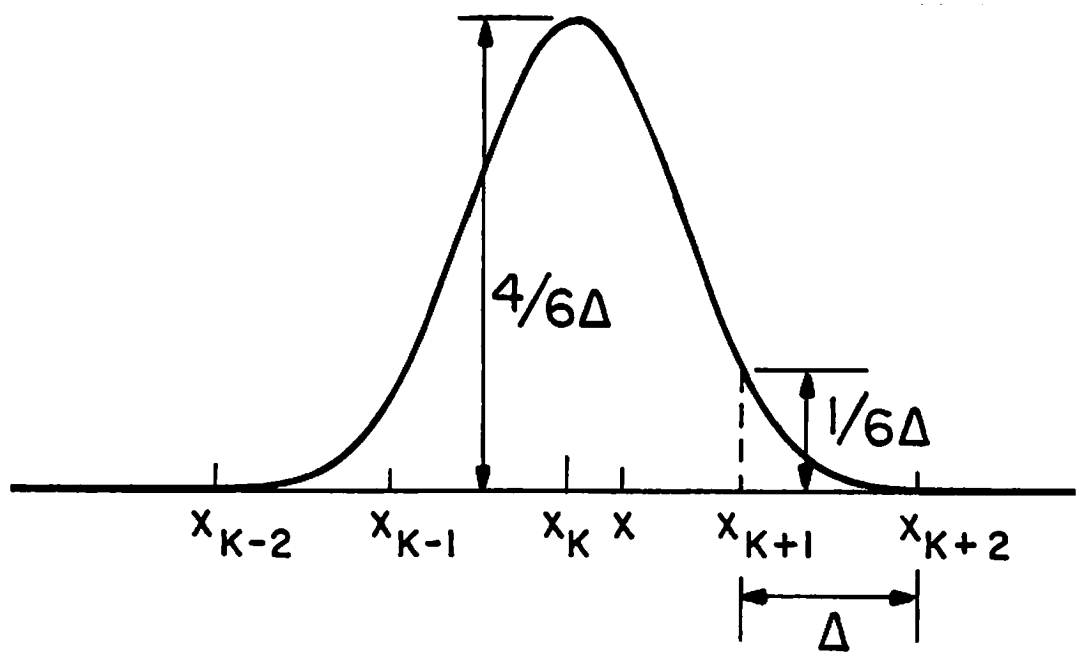

Fig. 2.5 Cubic B-spline function

$$s(x) = \text{rect}(\frac{x}{\Delta}) * \text{rect}(\frac{x}{\Delta}) * \text{rect}(\frac{x}{\Delta}) * \text{rect}(\frac{x}{\Delta}) \qquad (2\text{-}1)$$
$$= \Lambda(\frac{x}{\Delta}) * \Lambda(\frac{x}{\Delta})$$

where

$$\text{rect}(\frac{x}{\Delta}) = \begin{cases} 1 & |x| \leq \Delta/2 \\ 0 & \text{otherwise,} \end{cases} \qquad (2\text{-}2)$$

$$\Lambda(\frac{x}{\Delta}) = \text{rect}(\frac{x}{\Delta}) * \text{rect}(\frac{x}{\Delta}) \qquad (2\text{-}3)$$

and * denotes convolution. The cubic B-spline function can also be represented by cubic polynomial as follows

$$s(x) = \frac{1}{6\Delta^4}[(x-x_{K-2})_+^3 - 4(x-x_{K-1})_+^3 + 6(x-x_K)_+^3 - 4(x-x_{K+1})_+^3 + (x-x_{K+2})_+^3] \qquad (2\text{-}4)$$

where the x_i's are the nodes of the data points with even spacing Δ as shown in Fig. 2.5 and $(x-x_i)_+^3$ is defined by

$$(x-x_i)_+^3 = \begin{cases} (x-x_i)^3 & \text{if } x \geq x_i \\ 0 & \text{otherwise.} \end{cases} \qquad (2\text{-}5)$$

A one-dimensional cubic B-spline interpolation problem can be stated as following: given a one-dimensional data array g_i, i=1,...,N, we are to find another one-dimensional data array c_i, i=1,...,N, such that the convolution of the c_i's with the cubic B-spline function gives the original value g_i at the nodes. The interpolation values between

the nodes are thus obtained. In matrix form we have

$$G = \frac{1}{6\Delta}\begin{bmatrix} 4 & 1 & & & & 0 \\ 1 & 4 & 1 & & & \\ & 1 & 4 & 1 & & \\ & & & \ddots & \ddots & \\ & & & 1 & 4 & 1 \\ 0 & & & & 1 & 4 \end{bmatrix} C = AC \quad . \tag{2-6}$$

To interpolate the image g we need to find the c_i first. From Eq. (2-6) we can solve for C

$$C = A^{-1}G \quad . \tag{2-7}$$

To simplify the notation we will drop the factor $\frac{1}{6\Delta}$ and consider

$$A = \begin{bmatrix} 4 & 1 & & & & 0 \\ 1 & 4 & 1 & & & \\ & 1 & 4 & 1 & & \\ & & & \ddots & \ddots & \\ & & & 1 & 4 & 1 \\ 0 & & & & 1 & 4 \end{bmatrix} \quad . \tag{2-8}$$

A^{-1} can be found by a recursive formula [2-23]. Let $b_{k\ell}$ be the element of A^{-1} at the kth row and ℓth column; then

$$b_{k\ell} = b_{\ell k} = \frac{(-1)^{k+\ell}\mu_\ell \mu_{N-k+1}}{4\mu_N - \mu_{N-1}} \qquad \text{for } \ell \leq k$$

$$\mu_1 = 1 \tag{2-9}$$

$$\mu_2 = 4$$

$$\mu_i = 4\mu_{i-1} - \mu_{i-2} \qquad i = 3,4,\ldots,N.$$

An alternative method of inverting A can be obtained by adding 1 to the upper right and bottom left corners of the matrix and making A circulant. By modifying A we can invert A by Fourier transformation at the expense of

introducing error at the two ends. It has been shown [2-24] that a circulant matrix A can be diagonalized by Fourier transformation. Let F and F^{-1} be the Fourier transform and inverse Fourier transform kernel matrices respectively, i.e.,

$$[F_{k\ell}] = \exp(-j\frac{2\pi}{N}k\ell) \tag{2-10}$$

and

$$[F^{-1}_{k\ell}] = \exp(j\frac{2\pi}{N}k\ell) \tag{2-11}$$

then

$$FAF^{-1} = D = \begin{bmatrix} d_1 & & 0 \\ & d_2 & \\ & & \ddots \\ 0 & & d_N \end{bmatrix} \tag{2-12}$$

where D is a diagonal matrix with the diagonal components equal to the one-dimensional Fourier transform of the first row or the first column of A. Therefore we can obtain A^{-1} from Eq. (2-12)

$$A^{-1} = F^{-1}D^{-1}F \tag{2-13}$$

where

$$D^{-1} = \begin{bmatrix} \frac{1}{d_2} & & 0 \\ & \frac{1}{d_2} & \\ & & \ddots \\ 0 & & \frac{1}{d_N} \end{bmatrix} . \tag{2-14}$$

In our simulation, the image g_i is embedded in a larger zero array and the introduction of two 1's in the matrix A does not contribute significant error. Furthermore since the convolution will be done in the transform domain by using the DFT, the function g_i is considered periodic. Therefore the Fourier transform method is actually used in computing the coefficients c_i.

The input image array g_i to be filtered consists of 64 points with the center 32 points being a triangular function with different slopes on the two sides as shown in Fig. 2.6(a). The c_i's are computed according to Eqs. (2-7) and (2-13) and are shown in Fig. 2.6(b). In order to do the cubic B-spline interpolation these 64 points are then interlaced with zeros to form a 1024 array as shown in Fig. 2.6(c). Note that although all three curves in Fig. 2.6 have the same length, each consists of a different number of points. The reason for using 1024 points in Fig. 2.6(c) will become clear in the following discussion. As shown in Fig. 2.6(c) there are a few negative components which should not exist if incoherent filtering is considered. However since these negative coefficients are small we can either set them to zero or add a small constant bias to all coefficients without affecting the

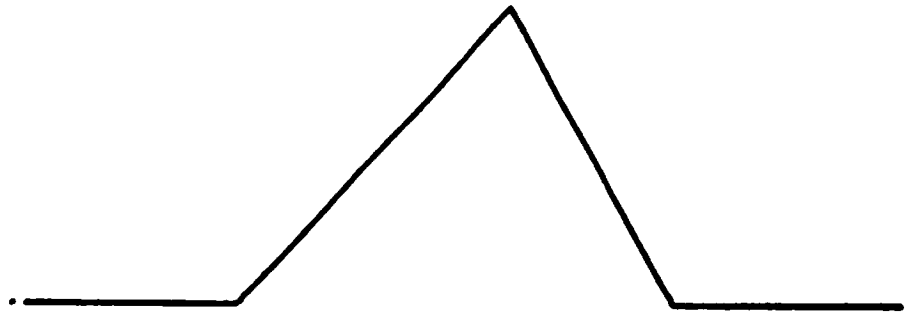

(a) ideal image (64 points)

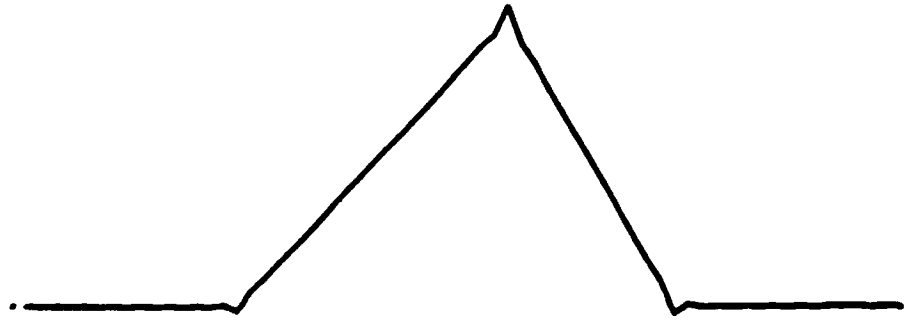

(b) spline coefficients (64 points)

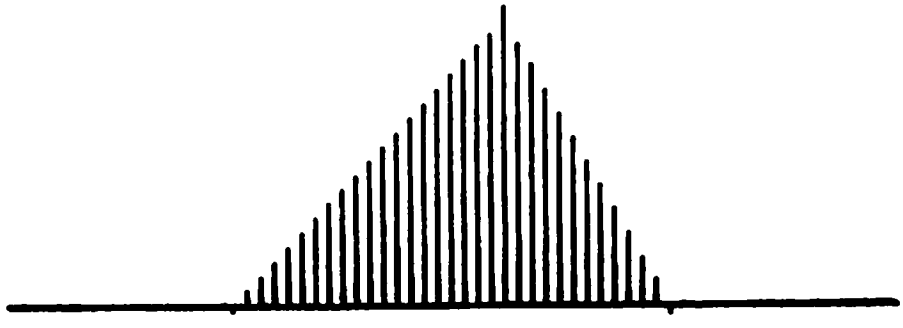

(c) spline coefficients (1024 points)

Fig. 2.6 Image to be used in the cubic B-spline interpolation

result significantly. In this simulation we simply leave them alone even though the result may not be an exact simulation unless the use of optical subtraction is considered.

Although the result of interpolation is a continuous function we can only consider a finite number of sampling points in the computer simulation. We plan to use the cubic B-spline interpolation to find an additional three points between each pair of original adjacent sampling points. Therefore the filtered output contains 256 (64x4) points. In order to achieve this result, the cubic B-spline function shown in Fig. 2.5 has to be sampled at 16 (4x4) points and then embedded in the same size array (256 points) as the impulse response. The convolution of these two functions is done in the transform domain and is actually a convolution of cyclic functions. However due to the use of a larger zero array surrounding the input, there is no contribution from adjacent periods. The convolution thus obtained would be the ideal result since the contributions are all from the sampling points of Fig. 2.5 and we know that the sampling points are not affected by the aliasing error. In order to see the effect of aliasing we perform a DFT interpolation on the cubic B-spline function (16 sampling points embedded in a 256 points zero array) and obtain an array of 1024 points. Therefore we

can see the effect of aliasing at the three points between any two adjacent original points. This interpolated cubic B-spline function is then convolved with the coefficients shown in Fig. 2.6(c). Note that the region outside the 16 sampling points is zero ideally, however, due to the use of phase coding it is nonzero in general. Therefore any coefficient in Fig. 2.6(c) may affect the value at points more than a 2Δ distance away. Here the large zero array in Fig. 2.6(c) is essential in preventing the contribution from other periods when the interpolation is done in the transform domain.

2.3.2 Simulations

Before examining the effect of different phase coding methods, we first generate an ideal impulse response (a cubic B-spline function) to compare with the DFT interpolated impulse responses obtained from different phase codings. The ideal cubic B-spline function has a width of 64 points embedded in a zero array of 1024 points. Figure 2.7(a) shows the center 128 points of this impulse response. The top half is the amplitude and the bottom half shows the phase which is zero. This function is convolved with the input sampled coefficients shown in Fig. 2.6(c) and we obtain the filtered result shown in Fig. 2.7(b) which again consists of an amplitude part and a

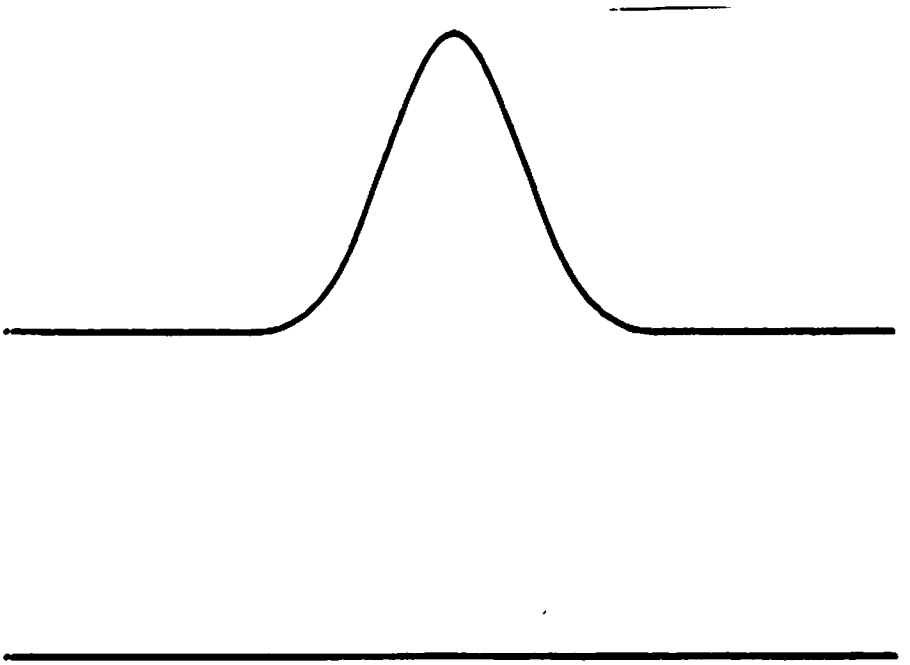

(a) impulse response (128 points)

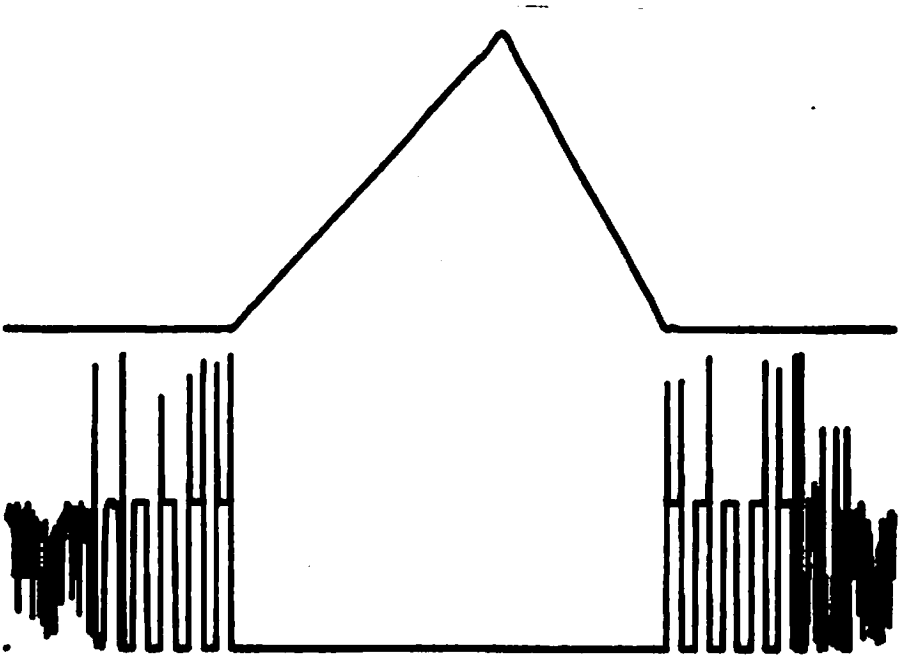

(b) filtered results (1024 points)

Fig. 2.7 Standard results

phase part. Note that this is no longer a perfect triangular function due to the fact that the cubic B-spline function is only a piecewise polynomial of third degree and is not capable of interpolating the abrupt changes at the boundaries. Since only the aliasing error due to phase coding is to be studied we will use Fig. 2.7 as the standard impulse response and filtered result in the following comparisons.

Due to the use of phase coding, the impulse response has correct values at the sampling points in intensity only and not in complex transmittance value. Therefore we only consider incoherent filtering. In order to get an incoherent impulse response of the cubic B-spline function we use the square root of the cubic B-spline function, $s_1(x)=s^{\frac{1}{2}}(x)$, to make the filter.

The main purpose of phase coding is to reduce the dynamic range and we will consider this effect first. The dynamic range will be defined as

$$\beta = \frac{|S_1|_{max}}{|S_1|_{min}} \qquad (2\text{-}15)$$

where $|S_1|_{max}$ and $|S_1|_{min}$ are the maximum and minimum absolute value of the Fourier transform of $s_1(x)$. However it is possible that there are only a few points reaching

very large or small values and the dynamic range defined above may not indicate the uniformity of the spectrum. Therefore we introduce a parameter called the efficiency η defined by

$$\eta = \frac{1}{N} \sum_{i=1}^{N} \frac{|S_{1i}|}{|S_1|_{max}} \tag{2-16}$$

where S_{1i} is the DFT of the sampled $s_1(x)$. This measures how efficiently the hologram material is used. By considering β and η we can evaluate how effective the phase coding is. Due to the use of phase coding, aliasing occurs which affects both the impulse response and the filtered result. Mean square errors are measured with Fig. 2.7 as the standard. The mean square errors of the impulse response and the filtered result are denoted as E_1 and E_2 respectively. Since the phase coding generally increases the mean square errors we further form two signal-to-noise ratios to evaluate the performance of the phase coding. These two S/N ratios are defined by

$$(S/N)_1 = \eta/E_1 \tag{2-17}$$

and

$$(S/N)_2 = \eta/E_2 \tag{2-18}$$

In addition to these parameters, figures of the impulse

response and filtered result are also shown.

We first try the impulse response with zero phase. The result is very close to the ideal one in Fig. 2.7 and is not repeated here. Only the parameters are shown in the first row of Table 2.1. Although the mean square errors are small the efficiency is poor as indicated by β and η in columns 2 and 3. The results of using random phase are shown in Fig. 2.8 with the parameters shown in the second row of Table 2.1. For easy comparison the ideal cubic B-spline function is also drawn in Fig. 2.8(a). The speckle-like noise is very severe in Fig. 2.8(a) but the effect has been cancelled out somewhat in Fig. 2.8(b). The phase part shown in Fig. 2.8(a) is associated with the square root cubic B-spline function $s_1(x)$. We then apply the space-transform iterative phase coding method with constant spectrum. One hundred iterations are used for this and the following iterative methods. The results are shown in Fig. 2.9. Although the speckle-like noise is severe the dynamic range and efficiency is considerably improved as shown in row 3 of Table 2.1. This shows that the iterative method is more effective in spectrum shaping. To reduce the aliasing error we apply a constrained bandwidth to the iterative method. The constrained spectrum is a rectangular function with half the total width and is denoted by 128/256 since the central 128

TABLE 2.1 THE EFFECTS OF PHASE CODING

phase coding	β	η	E_1	E_2	$(S/N)_1=\eta/E_1$	$(S/N)_2=\eta/E_2$
zero phase	.1123E6	.1264	.1003E-5	.6378E-7	.1259E6	.1982E7
random phase	.3553E2	.3606	.4820E0	.3034E0	.7481E0	.1189E1
256/256 rect	.1527E1	.8537	.8160E0	.2242E1	.1046E1	.3808E0
128/256 rect	.3571E2	.5014	.1253E-1	.3937E-2	.4002E2	.1274E3
224/512→256 rect	.1636E2	.7692	.1163E0	.6921E0	.6613E1	.1111E1
256/256 bell	.1466E2	.4770	.1860E0	.9094E0	.2565E1	.5245E0
128/256 bell	.2653E4	.2524	.7942E-6	.7778E-7	.3178E6	.3245E7
256/512→256 bell	.1192E3	.5004	.2405E-4	.8604E-4	.2081E5	.5816E4

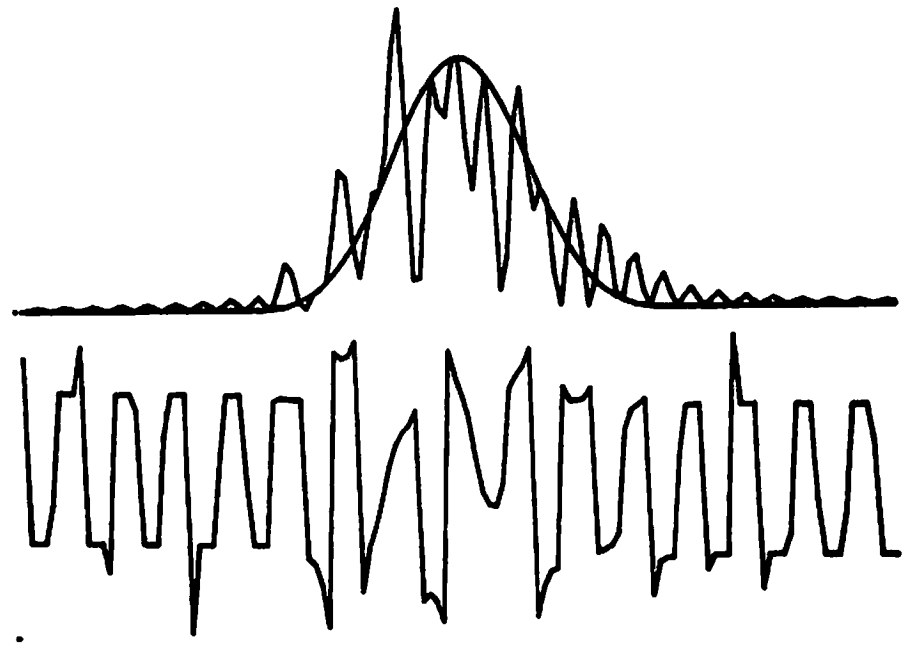

(a) impulse response

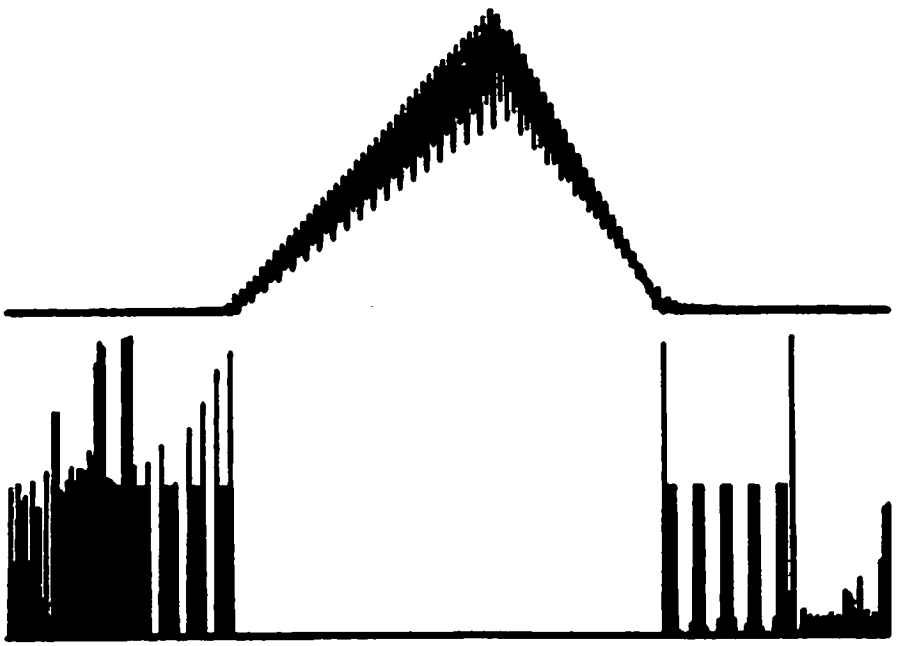

(b) filtered result

Fig. 2.8 Results of random phase coding

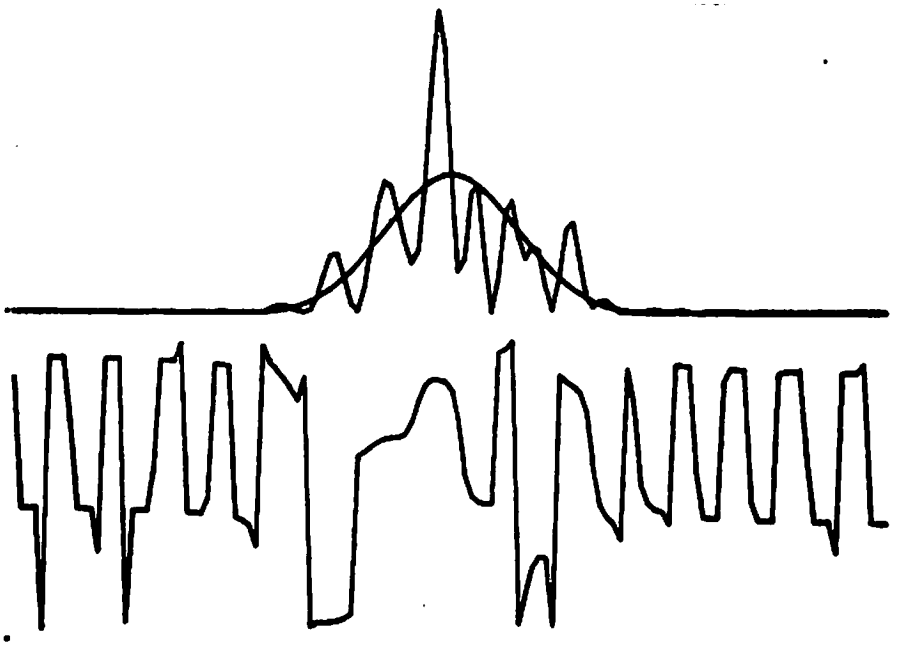

(a) impulse response

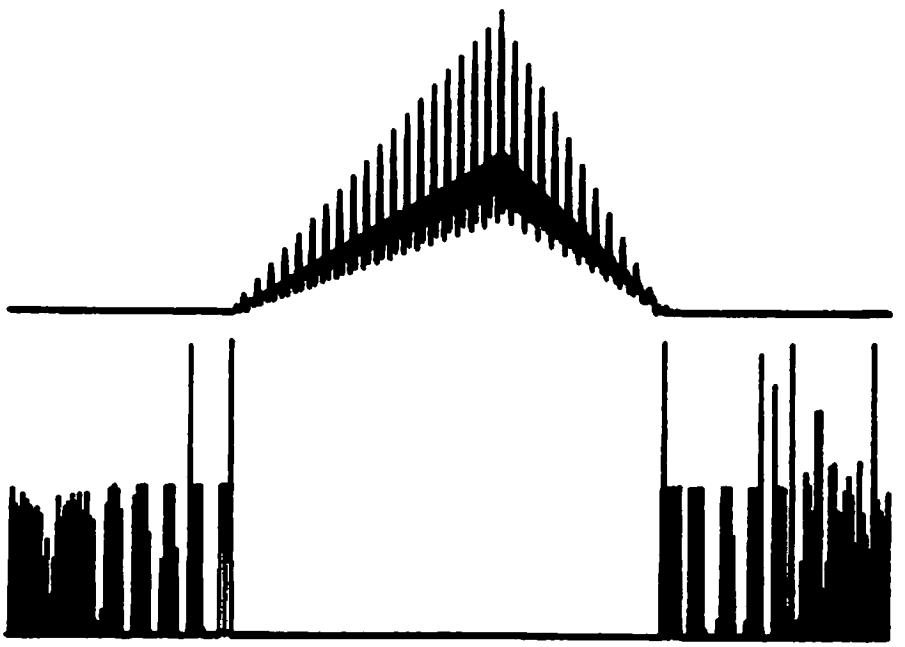

(b) filtered result

Fig. 2.9 Results of space-transform iterative phase coding (256/256 rectangular)

points out of 256 points are equal to one with the rest of the points being zero. These results are shown in Fig. 2.10. The speckle noise is much reduced as expected. Notice also that the phase shown in Fig. 2.10(a) is much smoother and this indicates that the less random phase does reduce the speckle-like noise. As shown in row 4 of Table 2.1 the mean square errors are reduced at the expense of low efficiency. However the signal-to-noise ratios do improve. To improve the efficiency we use the modified method. A spectrum of width 512 points with only the central 224 points being one is used in the iterative method and then only the central 256 points are used in making the filter. The results are shown in Fig. 2.11 and row 5 of Table 2.1. The efficiency is improved while the noise also increases. However the overall performance is better than the one using a constant spectrum.

In the above iterative methods the ideal spectra all have rectangular shapes and there are discontinuities at the boundaries. The spectra of natural objects usually are large in the low frequency region and fall off toward the high frequency region. Therefore it is reasonable to believe that a smoother spectrum should be able to fit better in the iterative method. The particular spectrum we choose for the following simulation has a bell shape. Figure 2.12 and row 6 of Table 2.1 show the result when the

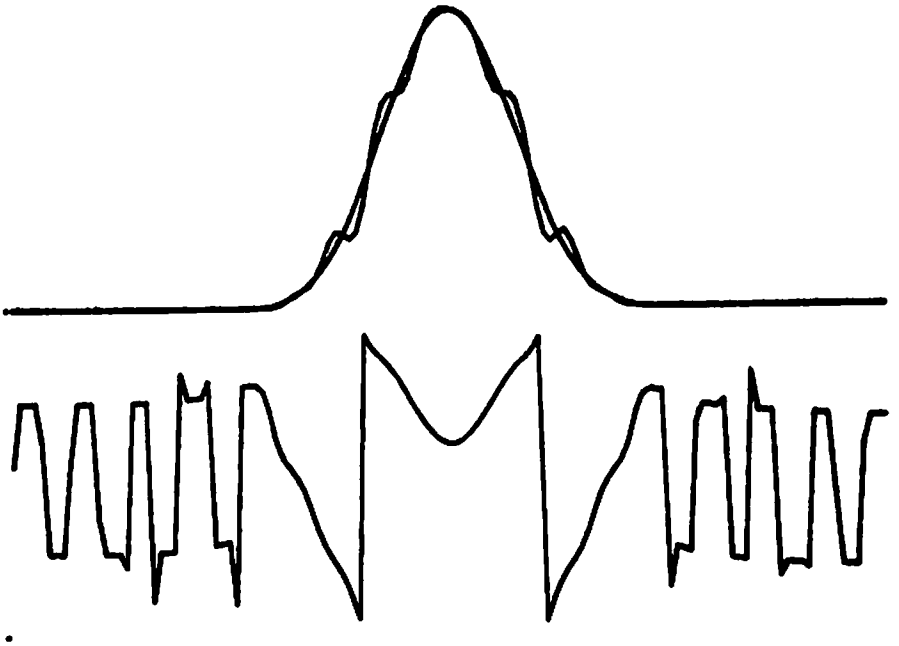

(a) impulse response

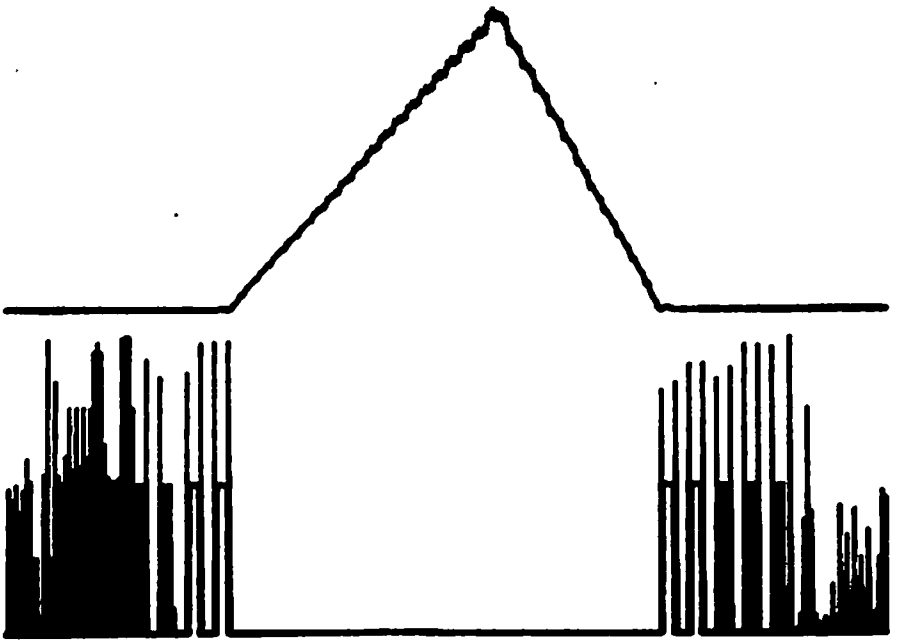

(b) filtered result

Fig. 2.10 Results of space-transform iterative phase coding (128/256 rectangular)

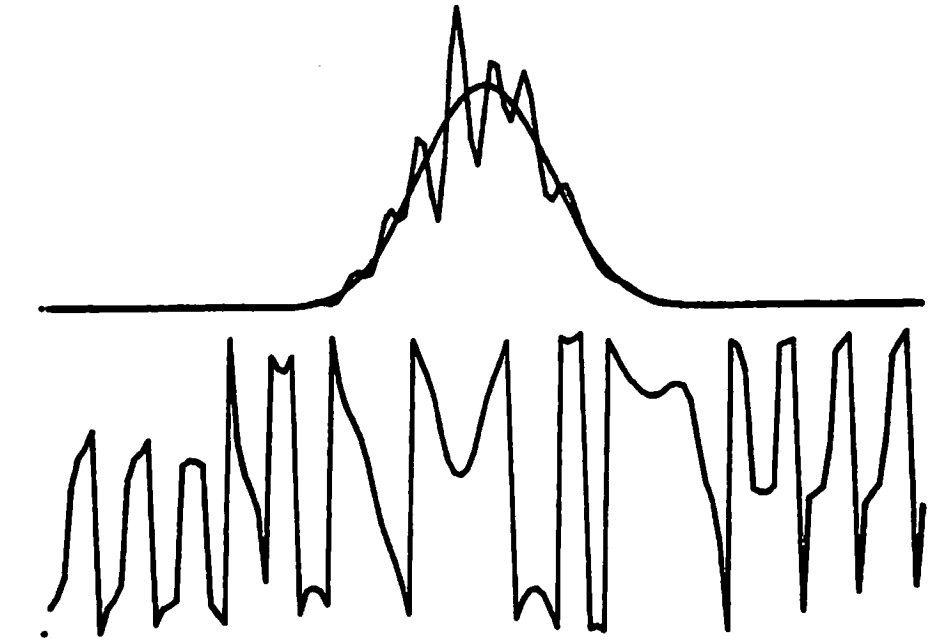

(a) impulse response

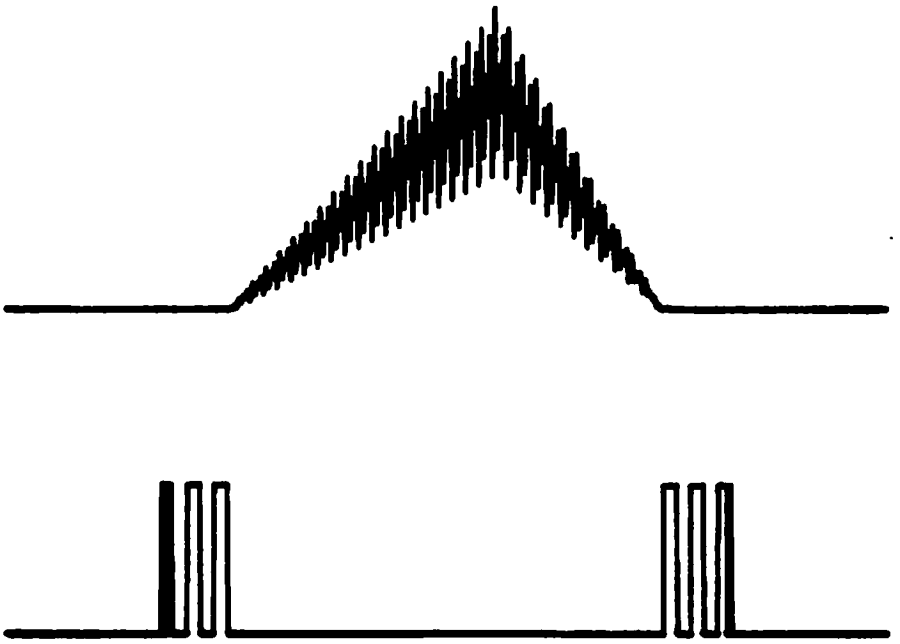

(b) filtered result

Fig. 2.11 Results of space-transform iterative phase coding (224/512 → 256 rectangular)

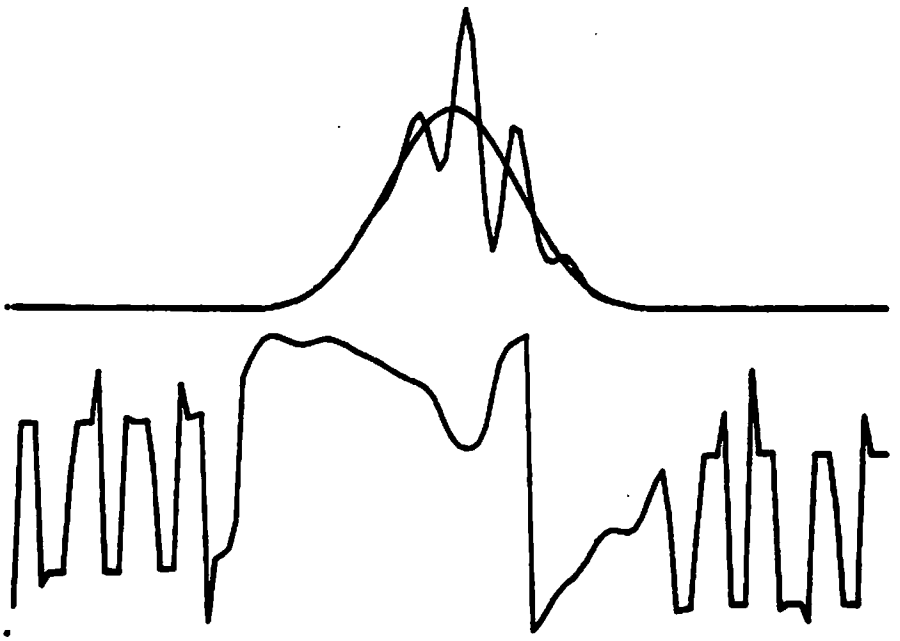

(a) impulse response

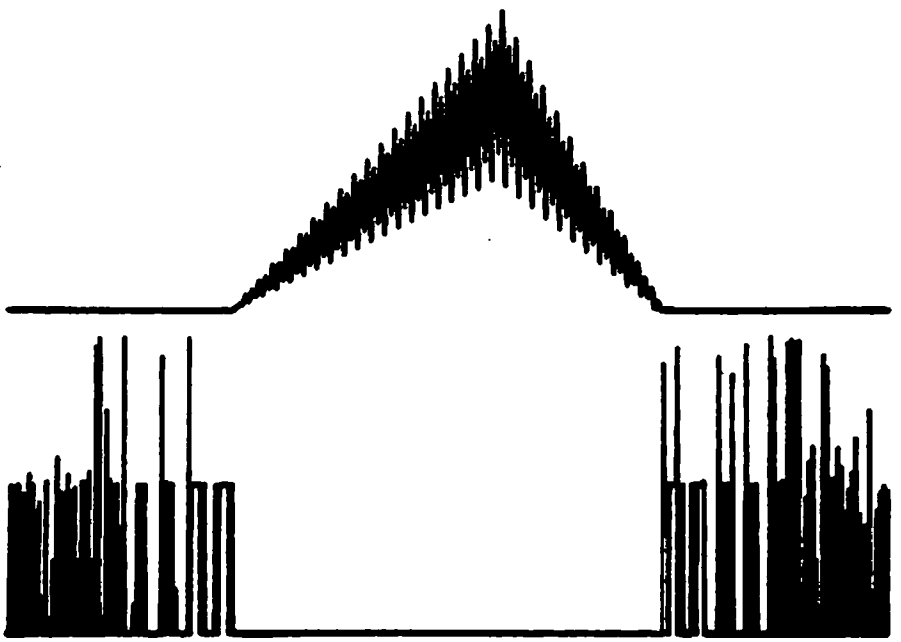

(b) filtered result

Fig. 2.12 Results of space-transform iterative phase coding (256/256 bell shape)

bell shape spectrum occupies the whole width. The results are not very impressive but are better than the constant spectrum results. To reduce the noise we then use a bell shape spectrum constrained to half the spectral width. The results are shown in Fig. 2.13 and row 7 of Table 2.1. The results are surprisingly good, almost coincident with the standards shown in Fig. 2.7. However the efficiency is low as the values of β and η indicate. To improve the efficiency we then use a bell shape spectrum of width 256 points embedded in a 512 points zero array as the ideal spectrum. Only the central 256 points are used for making the filter. This modified method not only improves the efficiency but also maintains an almost perfect impulse response and filtered result as shown in bottom row of Table 2.1 and Fig. 2.14.

2.3.3 Conclusions

In this section we have demonstrated the noise problem due to different phase coding techniques by using the cubic B-spline interpolation. Different phase coding methods are tried to see their effects in reducing the speckle noise while maintaining reasonable efficiency. These results are shown in Figs. 2.8 through 2.14 and some measurements are listed in Table 2.1. Note that these measurements may not reflect the performance very accurately and we require the

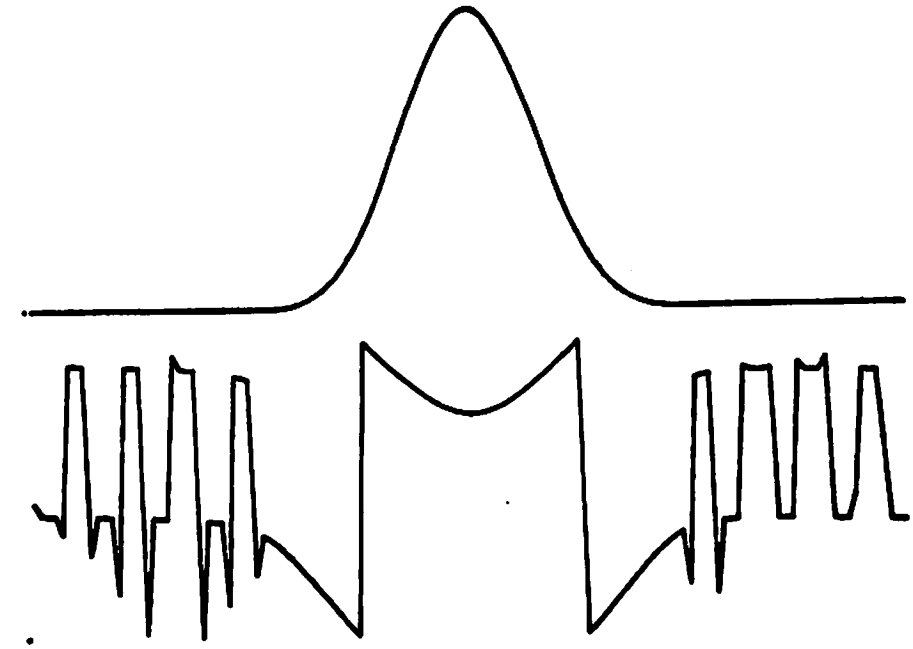

(a) impulse response

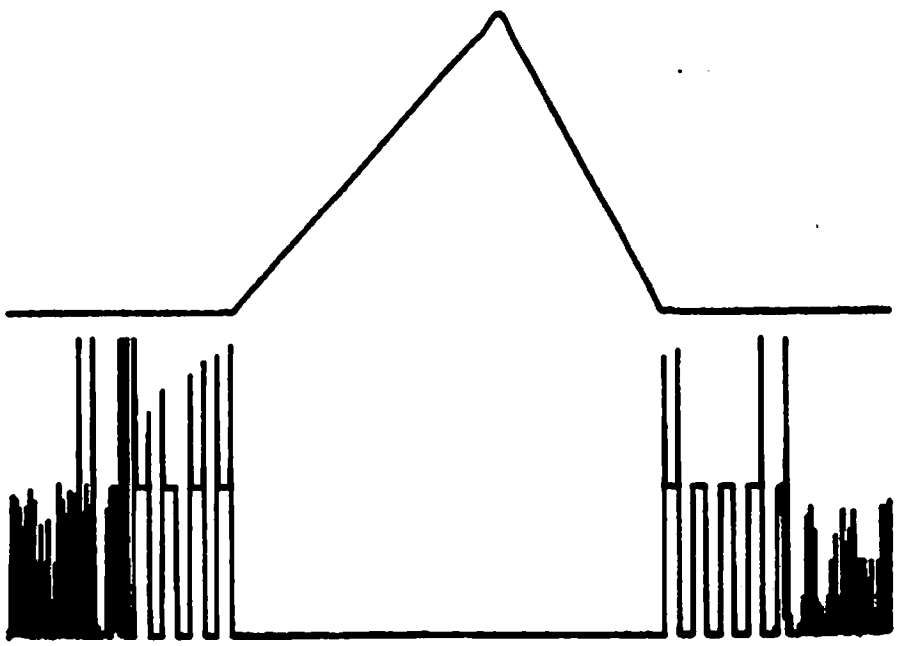

(b) filtered result

Fig. 2.13 Results of space-transform iterative phase coding (128/256 bell shape)

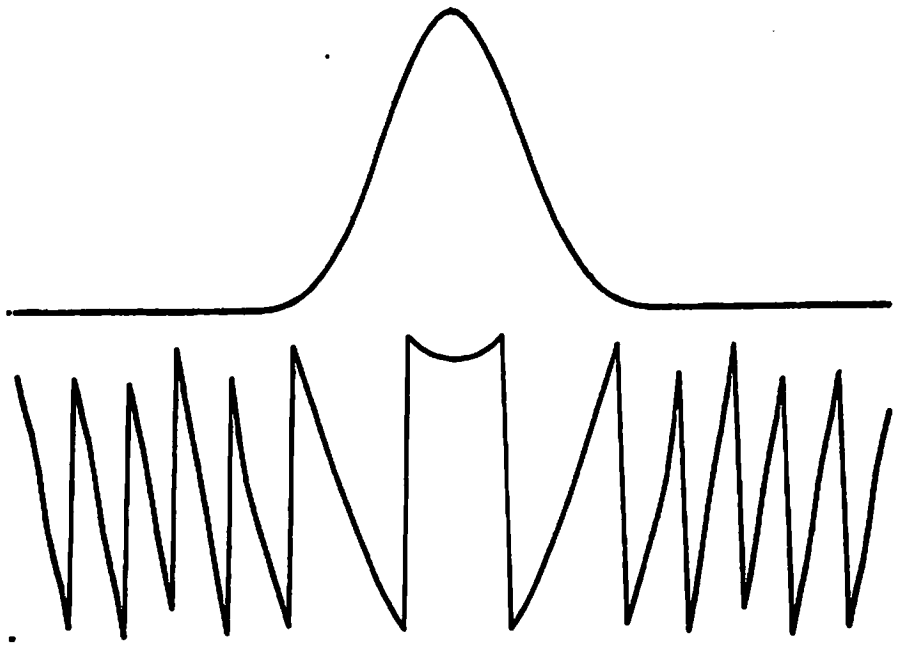

(a) impulse response

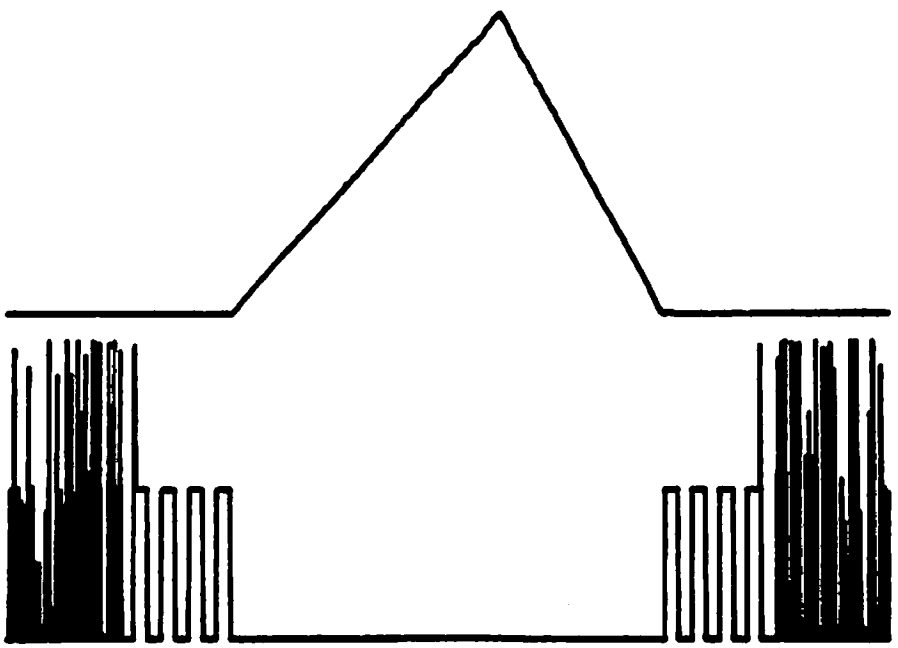

(b) filtered result

Fig. 2.14 Results of space-transform iterative phase coding (256/512 → 256 bell shape)

aid of the figures for more accurate comparison. For example when comparing Fig. 2.8(a) and Fig. 2.9(a), Fig. 2.8(a) appears no better than the other and is probably worse due to the noise outside the cubic B-spline function region. However this is not evident in the E_1 values shown in the second and third row of Table 2.1 Furthermore, both results in Figs. 2.13 and 2.14 are almost perfect while the S/N ratios shown in the last two rows of Table 2.1 are different by a factor of 10 and more than 100 respectively. However these measurements do facilitate the evaluation of different phase coding methods.

In general these results show that the aliasing error can be reduced by using constrained bandwidth at the expense of lower efficiency. A modified method which utilizes the constrained bandwidth but discards the high frequency components in making the filter is a good compromise between efficiency and noise reduction. It is also shown that a smooth spectrum can fit better in the iterative methods.

The iterative phase coding methods are more time consuming, but they are more capable of controlling the spectrum. The efficiency can be improved while the aliasing error is properly controlled. Although we have demonstrated the phase coding by using a one-dimensional

example, the same approach can be applied to two-dimensional functions. The computation time can be reduced if a two-dimensional function is separable. We can perform the phase coding on each of the one-dimensional functions and obtain the final result by multiplying them together.

CHAPTER 3

DOUBLE-PHASE HOLOGRAMS

Of all the classes of computer-generated holograms, binary holograms are the easiest to make. Having the Fourier transform of the object, only a plotter or a binary display device and photoreduction equipment are required to make this type of hologram. They also have the advantage of superior signal-to-noise ratio due to their binary transmission nature. The efficiency of a binary hologram can also be increased by bleaching. The bleaching is not critical in this process because inaccuracies only reduce the intensity rather than degrade the reconstruction image [3-1].

In this chapter we will discuss a new way of generating a binary hologram and consider the possibility of using it in an optical filtering system with a large input format.

3.1 Review of previous methods

Let $h(x,y)$ be the desired object and $H(u,v) = A(u,v)e^{j\theta(u,v)}$ its Fourier transform. The major

difficulty with digital holography is in finding a method to record the complex transmission values H(u,v) on a photographic or other optical recording medium which can only store non-negative real values. Area modulation and gray levels are used to represent amplitude, and various methods of encoding the phase by position modulation [3-2,3-3] within a Fourier transform resolution cell, or by the use of subcells [3-4,3-5], have been developed.

Lohmann et al. [3-2,3-3] have used a scheme shown in Fig. 3.1. A cell of size dxd is used to represent a Fourier component with a transparent slit in each cell representing its value H(u,v). The area of the slit is proportional to the amplitude A(u,v) and the position of the slit is shifted (in the v direction) by an amount Δ proportional to the phase angle $\theta(u,v)$.

In optical reconstruction, the hologram is illuminated by a uniform plane wave. If we look along an angle of $\phi = \sin^{-1}\lambda/d$ from the back of the hologram as shown in Fig. 3.1, we will observe the correct amplitude and phase [3-6] with the use of some approximations [3-3]. The desired object h(x,y) will be reconstructed at the first diffraction order when a lens is used [3-7].

Since any complex transmission value can be expressed by the summation of non-negative multiples of +1, -1, +j,

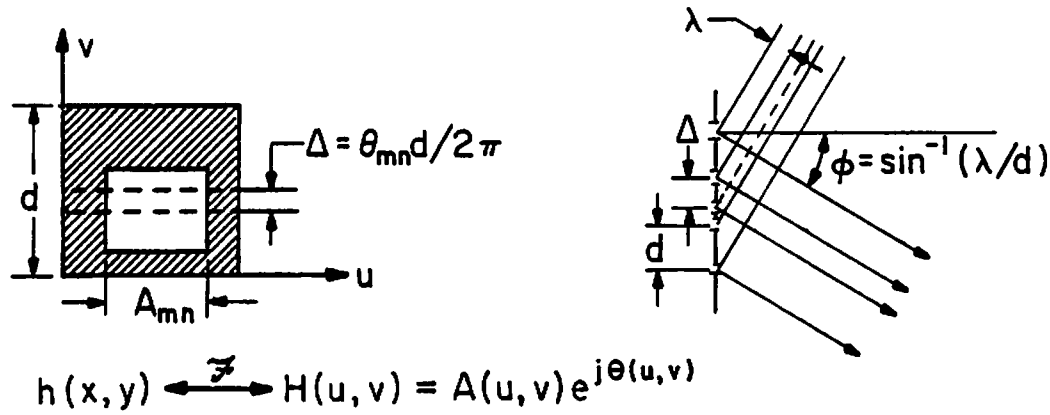

Fig. 3.1 Lohmann hologram

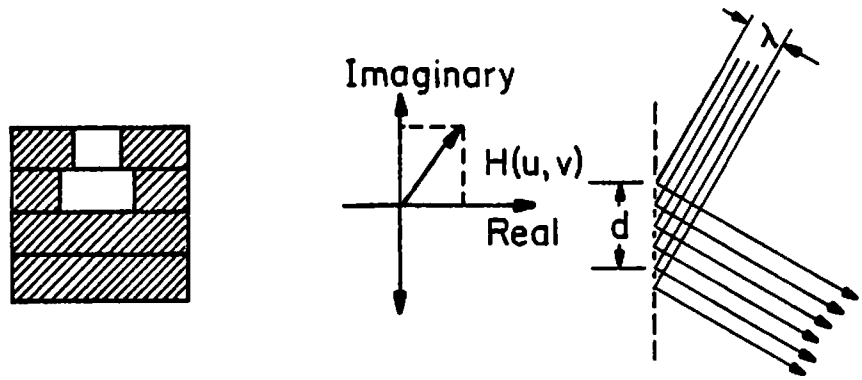

Fig. 3.2 Lee hologram

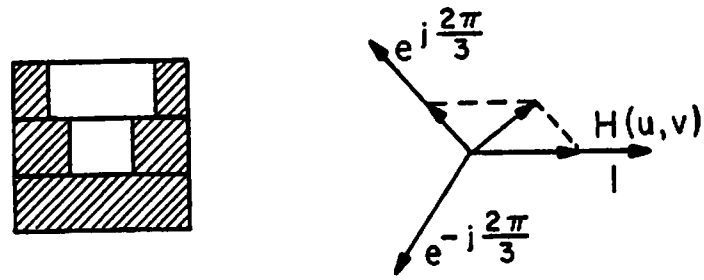

Fig. 3.3 Burckhardt hologram

and -j, where $j = \sqrt{-1}$, Lee [3-4] divided each cell into four subcells with a variable slit area or gray level in each subcell to represent the amplitude of each vector component. Figure 3.2 shows the configuration of each hologram cell, the decomposition of a vector, and the geometrical interpretation of the reconstruction. In Lee's original work, gray levels were used rather than a slit, and careful exposure control was required. Using the lens to perform transformation, the reconstruction appears at the first diffraction order. Note that although four components are used to represent a Fourier component, two of them at most are nonzero. Burckhardt [3-5] further found that instead of using four vectors to represent a complex value, three vectors pointing in the directions 0, $2\pi/3$, and $-2\pi/3$ can be used to represent any complex value as shown in Fig. 3.3. Like the Lee hologram, two of the three components at most are nonzero, and the reconstruction appears at the first diffraction order.

3.2 Theory

3.2.1 Basic principle

The new binary hologram is based on the principles that any complex function with finite maximum can be normalized to within a unit circle and that any complex transmission value $H = A\exp(j\theta)$ inside the unit circle

($0 \leq A \leq 1$) can be decomposed into the sum of two constant magnitude vectors. This decomposition can be expressed as

$$H = A\exp(j\theta) = \frac{1}{2}\exp[j(\theta+\psi)]+\frac{1}{2}\exp[j(\theta-\psi)], \qquad (3\text{-}1)$$

where

$$\psi = \cos^{-1}A \qquad 0 \leq \psi \leq \pi/2. \qquad (3\text{-}2)$$

Here we have dropped the (u,v) coordinates of the transform domain for simplicity. The two terms on the right side of Eq. (3-1) are designated H_1 and H_2, respectively, and are shown in Fig. 3.4. The vectors P, -P in Fig. 3.4 are called parity terms which will introduce error in the reconstruction due to the way of implementation as will be explained later. The decomposition can be applied to represent a complex value in a binary hologram by using the two phase quantities instead of the three non-negative quantities in a Burckhardt hologram. The new binary hologram is thus called double-phase hologram (DPH) [3-8].

As depicted in Fig. 3.5, each Fourier components on the hologram consists of two subcells. Each subcell has an open slit of fixed area in the opaque background with the position of the slit determined by the decomposed phases $\theta+\psi$ or $\theta-\psi$ from

$$d_1 = d(\theta+\psi)_{Mod2\pi}/2\pi \qquad (3\text{-}3)$$

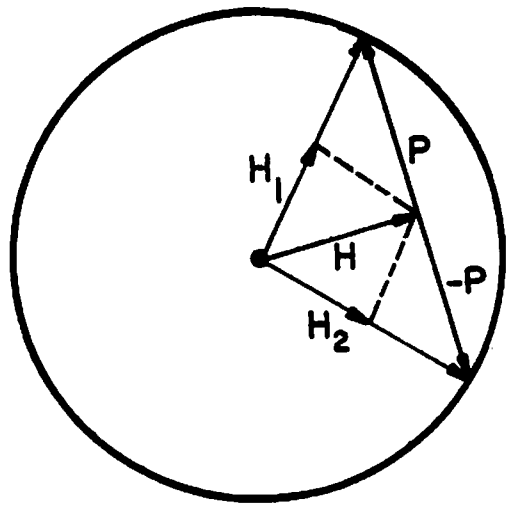

Fig. 3.4 Decomposition of a vector $H(u,v)$ in the unit circle into two constant magnitude vectors $H_1(u,v)$, $H_2(u,v)$ and the parity term $P(u,v)$

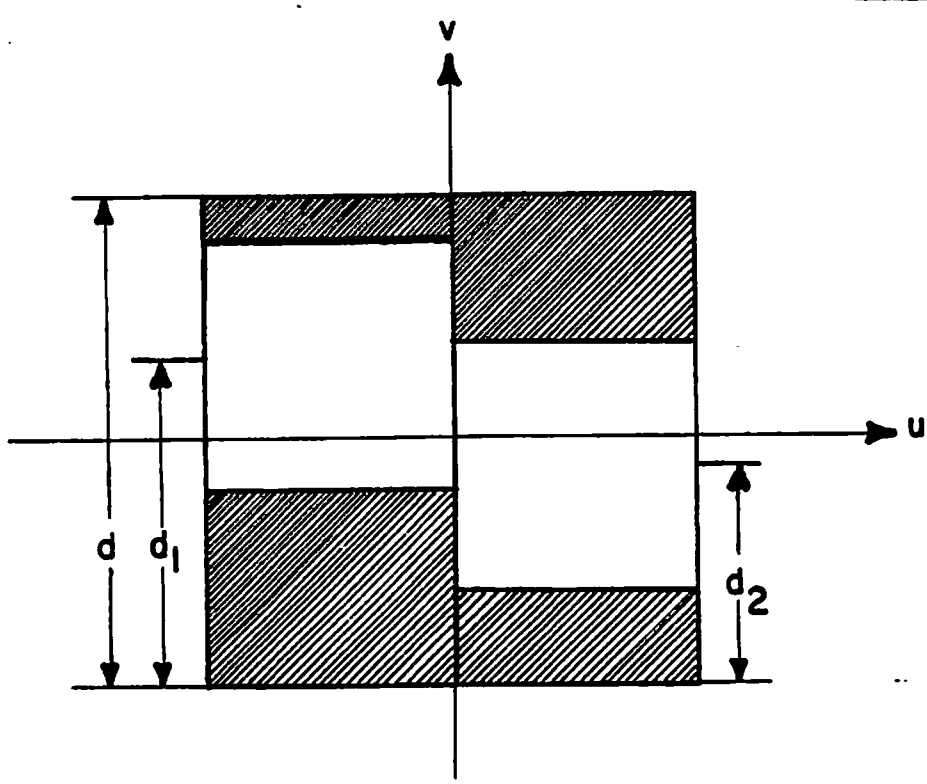

Fig. 3.5 Implementation of one cell in a DPH

$$d_2 = d(\theta-\psi)_{\text{Mod}2\pi}/2\pi \qquad (3\text{-}4)$$

where d is the width of one Fourier resolution cell. The width of the open slit is d/2 in order to maximize the diffraction efficiency. If we consider the subcells as a whole, each component has the correct complex value in the direction of the first diffraction order along the v direction. Therefore the reconstruction appears at the first diffraction order in the back focal plane of the lens.

Brown and Lohmann [3-2] and Haskell and Culver [3-9] used the same decomposition of Eqs. (3-1)-(3-2) in making binary holograms. Their implementation may result in the overlap of two slits. Although this problem can be avoided by limiting the size of the slits and the minimum distance between them, diffraction efficiency and dynamic range are reduced. Severcan [3-10] used this decomposition in phase-only spatial filtering systems. Chu and Goodman [3-11] used a similar configuration for encoding information in holographic memories. Chu and Fienup [3-12] also used this method in making a non-binary phase hologram called "synthetic coefficient hologram," which reconstructs an object close to the desired one on-axis.

In general, there are many ways to decompose a vector in the unit circle of the complex plane into two constant magnitude vectors. A vector $A\exp(j\theta)$ in the unit circle can be written as

$$H = A\exp(j\theta) = (n/2)\exp[j(\theta+\psi)]+(n/2)\exp[j(\theta-\psi)], \quad (3\text{-}5)$$

where

$$\psi = \cos^{-1}(A/n) \qquad 0 \leq \psi \leq \pi/2 \quad (3\text{-}6)$$

and n is an integer ≥ 1.

When a DPH is used to implement the two terms of the sum in Eqs. (3-5) and (3-6), Eq. (3-5) is rewritten as

$$\begin{aligned} 1/2\ \exp[j(\theta+\psi)]+1/2\ \exp[j(\theta-\psi)] &= (A/n)\exp(j\theta) \\ &= H/n \end{aligned} \quad (3\text{-}7)$$

because each vector in the sum carries half of the input energy. For n = 1 we obtain Eqs. (3-1) and (3-2), and for n = 2 we get

$$H/2 = (A/2)\exp(j\theta) = 1/2\ \exp[j(\theta+\psi)]+1/2\exp[j(\theta-\psi)], \quad (3\text{-}8)$$

where

$$\psi = \cos^{-1}(A/2), \qquad \pi/3 \leq \psi \leq \pi/2. \quad (3\text{-}9)$$

Notice that using any $n \geq 2$ restricts the available range of complex transmission values inside the unit circle.

This will generally reduce the diffraction efficiency because it is proportional to $1/n^2$. in addition, for larger n, ψ [Eq. (3-6)] varies over a smaller range. For example, when n = 2 as in Eq. (3-9), the range of ψ is now restricted to $\pi/3 \leq \psi \leq \pi/2$. Shmarev [3-13] used this decomposition in a kinoform filtering system.

3.2.2 Quantization errors

In Eq. (3-1), if n = 1 is chosen, the angle ψ is related to the amplitude A by

$$A = \cos \psi \qquad 0 \leq \psi \leq \pi/2 \tag{3-10}$$

and its derivative is given by

$$(dA)/(d\psi) = -\sin \psi \qquad 0 \leq \psi \leq \pi/2. \tag{3-11}$$

In the implementation of the DPH, the quantities $(\theta+\psi)$ and $(\theta-\psi)$ are quantized to $\theta+\psi+\Delta_1$ and $\theta-\psi+\Delta_2$, respectively, where Δ_1 and Δ_2 are the quantization errors and have uniform distributions between $-\pi/M$ and π/M if there are M quantization levels. Therefore, θ and ψ become

$$\hat{\theta} = \theta+(\Delta_1+\Delta_2)/2, \tag{3-12}$$

$$\hat{\psi} = \psi+(\Delta_1-\Delta_2)/2. \tag{3-13}$$

We may consider $\Delta\theta = (\Delta_1+\Delta_2)/2$ and $\Delta\psi = (\Delta_1-\Delta_2)/2$ as the

quantization errors of θ and ψ, respectively, although they are not quantized physically. The amplitude is therefore given by

$$\hat{A} = \cos \hat{\psi} \quad . \tag{3-14}$$

Since Δ_1 and Δ_2 have uniform distributions, $\Delta\theta$ and $\Delta\psi$ have triangular distributions with the width of $4\pi/M$ and are independent of the normalized Fourier spectrum A. However, as shown in Eq.(3-11) the absolute value of $dA/d\psi$ is an increasing function in the defined range. Therefore, the same amount of quantization error in $\hat{\psi}$ results in smaller error in $\hat{A}$ when A is close to 1 (ψ close to 0) and larger error in $\hat{A}$ when A is close to 0 (ψ close to $\pi/2$). This indicates that it is better to have a nearly constant Fourier spectrum so that most of the normalized spectrum A will be close to 1 and therefore reduce the quantization error. Therefore the phase coding techniques described in Chapter 2 not only reduce the dynamic range in the transform domain but also reduce the quantization errors in DPH.

When values of n other than 1 are chosen in Eq. (3-5), ψ has a smaller range with $\pi/2$ as the boundary as illustrated in Eqs. (3-8) and (3-9) for the case of n=2. Therefore, for $n \geq 2$ the hologram has worse amplitude quantization errors in addition to the disadvantage of low

light efficiency.

3.2.3 Analysis of the reconstruction

Due to the use of area modulation and position modulation in representing the amplitude and phase of a binary hologram, the hologram suffers from the so called aperture error and detour-phase error [3-14]. However it has been found [3-15] that the quantization noise and aliasing errors are much more noticeable than the aperture and detour-phase errors. The quantization error has been discussed in the Section 3.2.2 qualitatively. The aliasing error is also discussed in Chapter 2. In this section when we analyze the reconstruction from a DPH we will neglect these errors and study the error introduced by the parity term P(u,v) as shown in Fig. 3.4.

The reconstruction of the DPH appears only in the +1 diffraction order or -1 diffraction order (conjugate) along the y direction. Other y orders have incorrect phase and therefore we only consider the +1 diffraction order along the y direction in this chapter. To simplify the analysis, we will formulate equations as though the hologram were an on-axis hologram. This does not affect result since only the error caused by the parity term P(u,v) is of concern and other errors, for example detour-phase error, are neglected. Whenever the term diffraction order is used in

the following discussion of this chapter it is understood to be the x direction unless otherwise stated. To avoid any confusion, we will use the notation (n,l) occasionally to indicate the nth diffraction order in the x direction along the +l diffraction order in the y direction.

If the hologram has a cell size of dxd, then it can be expressed as

$$\begin{aligned} H_s(u,v) &= [H(u,v)\cdot\sum_{m,n=-\infty}^{\infty}\sum\delta(u-md)\,\delta(v-nd)]*\mathrm{rect}(u/d,v/d) \\ &= [H(u,v)\cdot\frac{1}{d^2}\mathrm{comb}(u/d,v/d)]*\mathrm{rect}(u/d,v/d)\ , \end{aligned} \tag{3-15}$$

where comb(·,·) is a two-dimensional function defined by

$$\mathrm{comb}(u,v) = \sum_{m,n=-\infty}^{\infty}\sum\delta(u-m)\,\delta(v-n)\,. \tag{3-16}$$

In this expression we have assumed that H(u,v) is bandlimited and that the hologram is large enough to cover all the nonzero components. Therefore the summation indices go from $-\infty$ to ∞. Upon reconstruction we get (omitting the scale factor $1/\lambda f$)

$$\begin{aligned} h_s(x,y) &= [h(x,y)*\mathrm{comb}(dx,dy)]\cdot d^2\mathrm{sinc}(dx,dy) \\ &= d^2 W_h(x,y)\,[h(x,y)*\mathrm{comb}(dx,dy)], \end{aligned} \tag{3-17}$$

where

$$W_h(x,y) = \text{sinc}(dx,dy) \tag{3-18}$$

is the weighting function, and

$$\text{sinc}(x,y) = \frac{\sin\pi x}{\pi x} \cdot \frac{\sin\pi y}{\pi y} \quad . \tag{3-19}$$

The one-dimensional version of the above expressions is shown in Fig. 3.6. The results of Eqs. (3-17)-(3-19) are an approximate representation of the reconstruction from a DPH since they are valid only when we observe the reconstruction at the +1 diffraction order along the y direction. Furthermore, a complex transmission function H(u,v) is assumed in these equations.

From Eq. (3-17) the reconstruction is repeated with a period of 1/d in the x direction at the +1 diffraction order along the y direction and is attenuated by the sinc function. Usually we are interested in the zero order (0,1), and the distortion due to the sinc function can be precompensated by multiplying the object h(x y) with 1/sinc function in the x direction. The effect of the finite size in the y direction is similar and is compensated in the same way.

The implementation of a DPH is based on the decomposition of a vector into two other constant magnitude vectors as given by Eqs. (3-1) and (3-2). By defining

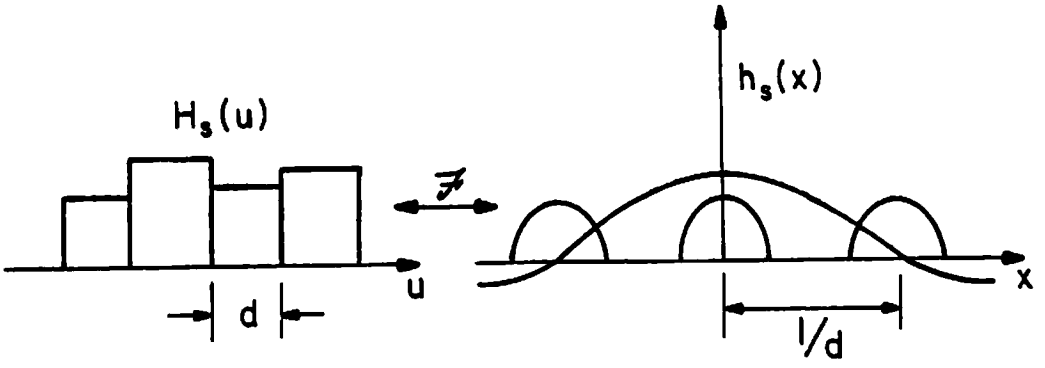

Fig. 3.6 Hologram and its reconstruction (ideal case)

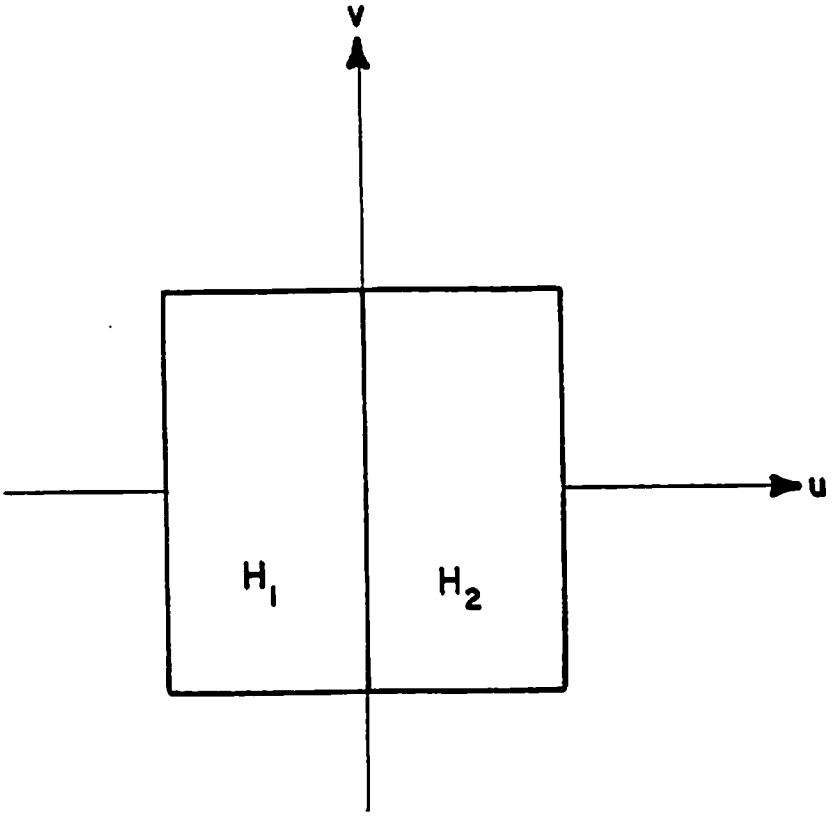

Fig. 3.7 Expression of one cell in terms of $H_1(u,v)$ and $H_2(u,v)$

$$H+P = 2H_1 \tag{3-20}$$

$$H-P = 2H_2 \tag{3-21}$$

where P is the vector called the parity term as shown in Fig. 3.4, the decomposition of Eqs. (3-1) and (3-2) can be rewritten as [3-10]

$$H = H_1+H_2 = 1/2(H+P)+1/2(H-P) \quad . \tag{3-22}$$

If H_1 and H_2 were overlapped at the same position, P and -P will cancel out, and the correct transform is obtained. However, due to the method of implementing the DPH, these two terms do not exactly cancel out, generally resulting in parity noise. Here we analyze this error and discuss some ways of reducing it.

Suppose that two subcells (Fig. 3.7) are used to represent the two components H_1 and H_2. When observed along the direction of the +1 diffraction order in y the hologram is given by

$$\begin{aligned} H_s'(u,v) &= \{[H(u,v)+P(u,v)]\frac{1}{d^2}\mathrm{comb}(u/d,v/d)\} * \mathrm{rect}(\frac{u+d/4}{d/2},\frac{v}{d}) \\ &\quad + \{[H(u,v)-P(u,v)]\frac{1}{d^2}\mathrm{comb}(u/d,v/d)\} * \mathrm{rect}(\frac{u-d/4}{d/2},\frac{v}{d}) \\ &= [H(u,v)\cdot\frac{1}{d^2}\mathrm{comb}(u/d,v/d)] * \mathrm{rect}(u/d,v/d) \\ &\quad + [P(u,v)\cdot\frac{1}{d^2}\mathrm{comb}(u/d,v/d)] * [\mathrm{rect}(\frac{u+d/4}{d/2},\frac{v}{d}) - \mathrm{rect}(\frac{u-d/4}{d/2},\frac{v}{d})], \end{aligned} \tag{3-23}$$

where the 1/2 in Eq. (3-22) is taken into account by the

size of the rect function. The first term is exactly the same as Eq. (3-15), and the second term introduces the noise. Denoting the second term by $P_s(u,v)$ and its inverse transform by $p_s(x,y)$, we have

$$\begin{aligned} p_s(x,y) &= [p(x,y)*\mathrm{comb}(dx,dy)]\frac{d^2}{2}\mathrm{sinc}(dx/2,dy) \\ &\quad \cdot[\exp(-j2\pi dx/4)-\exp(j2\pi dx/4)] \qquad (3\text{-}24) \\ &= jd^2 W_p(x,y)\,[p(x,y)*\mathrm{comb}(dx,dy)], \end{aligned}$$

where $p(x,y)$ is the inverse transform of the parity term $P(u,v)$ and will be called the parity noise, and

$$W_p(x,y) = -\mathrm{sinc}(dx/2,dy)\sin(\pi dx/2) \qquad (3\text{-}25)$$

is the weighting function. $W_p(x,y)$ is computed and drawn in Fig. 3.8. At the zero order (0,1) the noise term $p(x,y)$ is strongly attenuated by $\sin(\pi dx/2)$. Since $h(x,y)$ is space-limited we may assume that $p(x,y)$ is also space-limited to a small region. Therefore in the region of interest (zero order) noise is less noticeable. On the other hand at $x = 1/d$ (+1 order), $\sin(\pi dx/2)$ reaches its maximum, and $\mathrm{sinc}(dx/2)$ does not fall off too much [$\mathrm{sinc}(1/2) \simeq 0.64$] while the object $h(x,y)$ is strongly attenuated by $\mathrm{sinc}(dx)$ at $x = 1/d$. Therefore, the error term dominates at the first diffraction order.

Each cell can be further divided into more subcells as long as they sum up with the correct transform value.

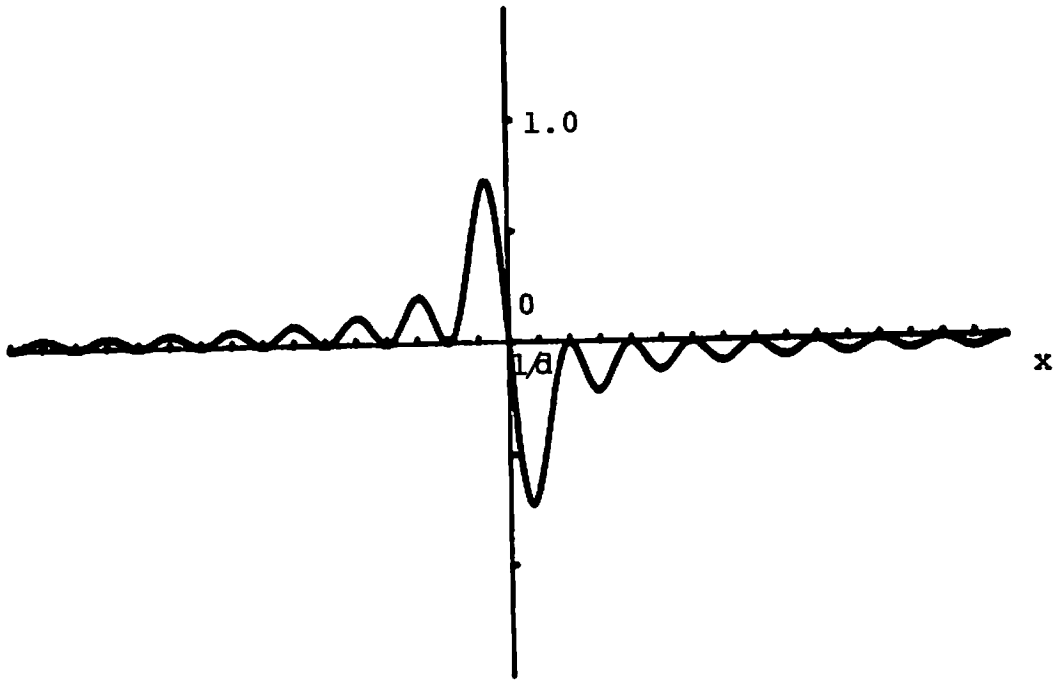

Fig. 3.8 Noise weighting function $W_p(x)$ for 2 subcells

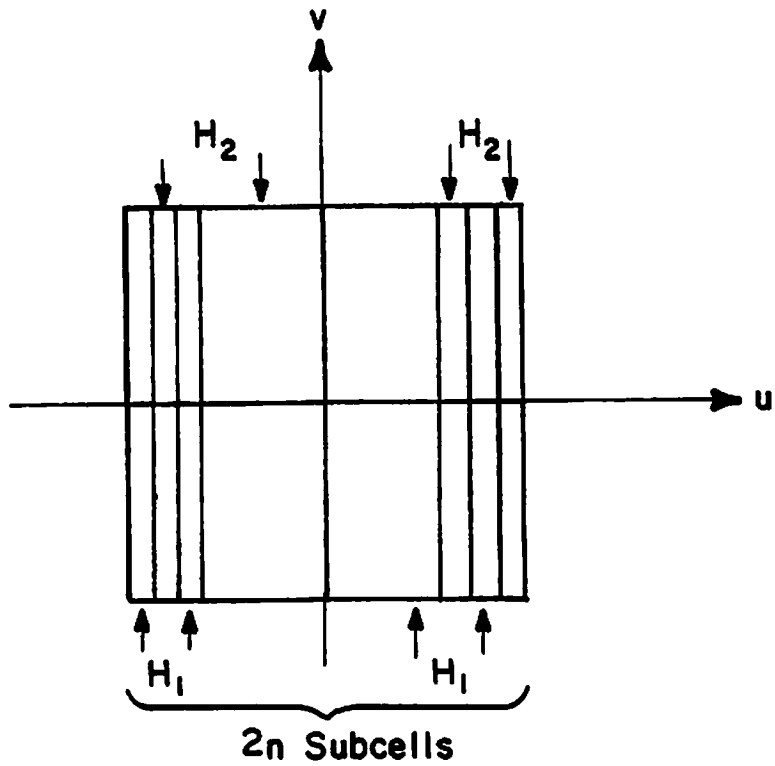

Fig. 3.9 Configuration of one cell with 2n subcells

Suppose there are 2n subcells in each cell with the interlaced configuration shown in Fig. 3.9. We can proceed as in Eqs. (3-23) to (3-25) and get

$$H_s'(u,v) = H_s(u,v)+P_s(u,v) \tag{3-26}$$

where the $H_s(u,v)$ is the same as Eq. (3-15) and $P_s(u,v)$ is given by

$$\begin{aligned} P_s(u,v) = {} & [P(u,v)\cdot\frac{1}{d^2}\mathrm{comb}(u/d,v/d)]*\{\mathrm{rect}(v/d)\cdot \\ & [\mathrm{rect}(\frac{u+(2n-1)d/4n}{d/2n})-\mathrm{rect}(\frac{u+(2n-3)d/4n}{d/2n}) \\ & +\ldots+\mathrm{rect}(\frac{u-(2n-3)d/4n}{d/2n})-\mathrm{rect}(\frac{u-(2n-1)d/4n}{d/2n})]\}. \end{aligned} \tag{3-27}$$

Upon reconstruction, this term gives

$$p_s(x,y) = jd^2W_p(x,y)[p(x,y)*\mathrm{comb}(dx,dy)] \tag{3-28}$$

where

$$\begin{aligned} W_p(x,y) = {} & \frac{(-1)^n}{n}\mathrm{sinc}(dx/2n,dy)\{\sin\phi-\sin3\phi+\ldots \\ & +(-1)^{n-1}\sin(2n-1)\phi\}\ , \end{aligned} \tag{3-29}$$

with $\phi=\pi dx/2n$. For n = 2,3,4 the closed form of $W_p(x,y)$ is given by

$$W_p(x,y;n=2) = -\mathrm{sinc}(dx/4,dy)\sin(\pi dx/4)\cos(\pi dx/2), \tag{3-30}$$

$$\begin{aligned} W_p(x,y;n=3) = {} & -\mathrm{sinc}(dx/6,dy)\sin(\pi dx/6)\cdot \\ & [1-\tfrac{4}{3}\sin^2(\pi dx/3)], \end{aligned} \tag{3-31}$$

$$W_p(x,y;n=4) = \mathrm{sinc}(dx/8,dy)\sin(\pi dx/8)\cos(\pi dx/4)\cdot [2\sin^2(\pi dx/4)-1] \quad . \tag{3-32}$$

The sinusoidal function $\sin(\pi dx/4)$, $\sin(\pi dx/6)$ and $\sin(\pi dx/8)$ in $W_p(x,y;n)$ make the noise term less noticeable for larger n. A closed form of Eq. (3-29) for $n > 4$ can also be found but is expected to be tedious and messy. Instead curves of $W_p(x,y;n)$ for different n are plotted and shown in Figs. 3.10-3.12.

Some conclusions can be made based on the above observations:

(1). As n increases the noise term around $x = 0$ is expected to reduce and we can get better reconstruction by using more subcells.

(2). The dominating noise term appears at the $\pm n$ orders $(\pm n,1)$.

(3). Other noise term orders are strongly attenuated and most of them are on the zeroes of the weighting function.

The experimental results shown in Section 3.5 are consistent with the predictions here. Orderings of subcells other than the interlaced cells in Fig. 3.9 are possible, but they will have more noise at the zeroth order.

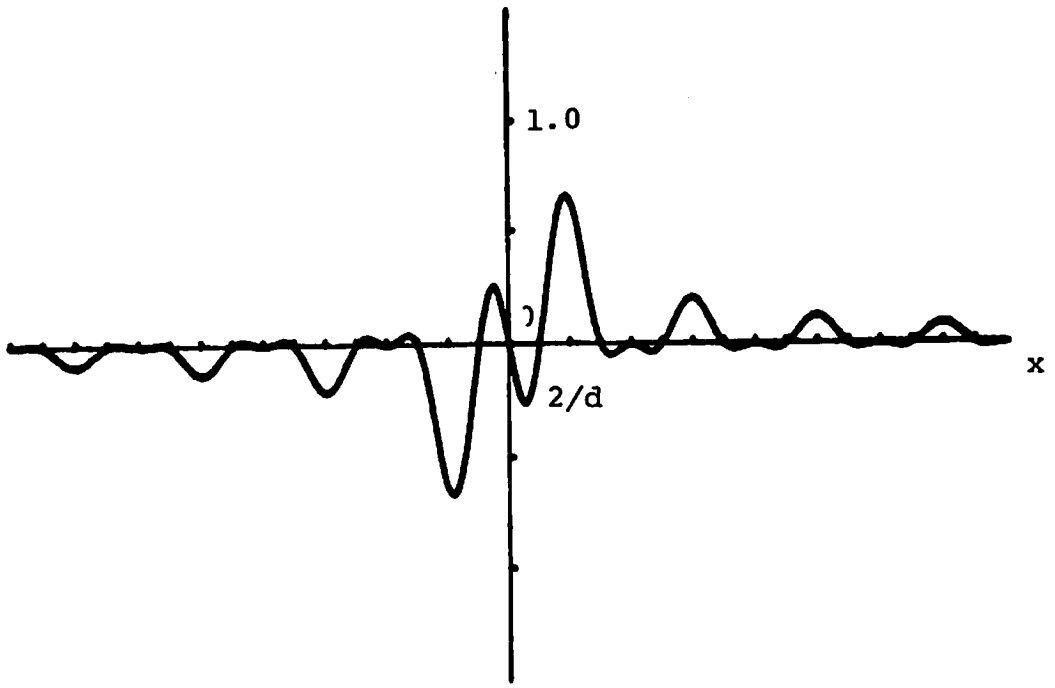

Fig. 3.10 Noise weighting function $W_p(x)$ for 4 subcells

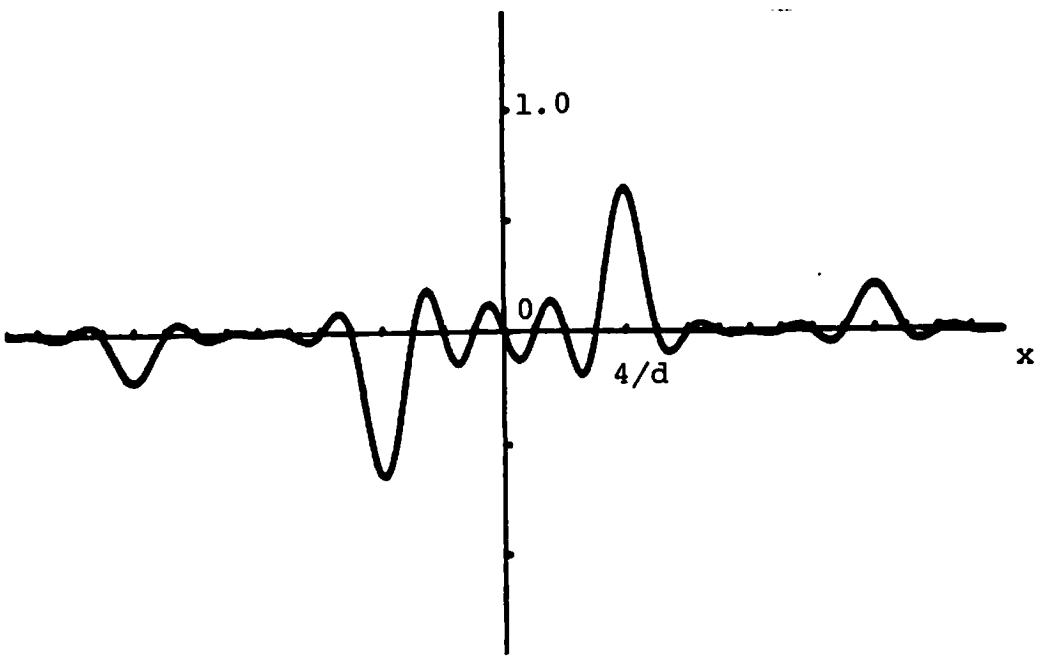

Fig. 3.11 Noise weighting function $W_p(x)$ for 8 subcells

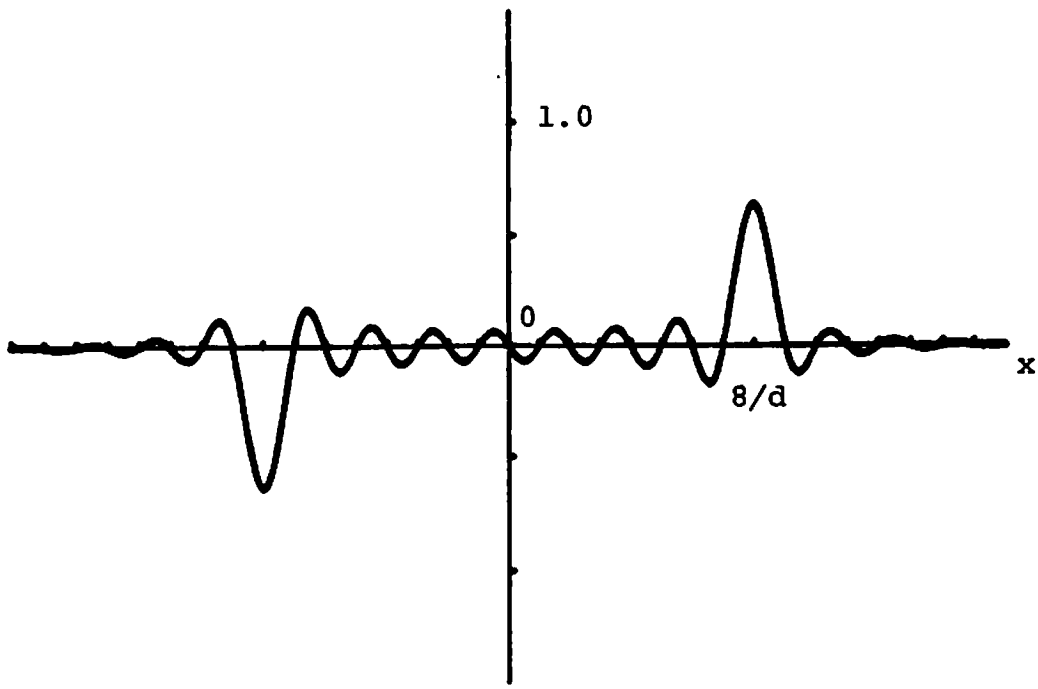

Fig. 3.12 Noise weighting function $W_p(x)$ for 16 subcells

One difference between the DPH and other types of holograms is that the reconstruction is not symmetric because the +1 order (1,1) is unlike the -1 order (-1,1) for number of subcells greater than two. Notice that what we actually observe is

$$\begin{aligned} \mathcal{O}(x,y) &= |h_s(x,y)+p_s(x,y)|^2 \\ &= d^4 |W_h(x,y)\,[h(x,y)*\mathrm{comb}(dx,dy)] \\ &\quad +jW_p(x,y)\,[p(x,y)*\mathrm{comb}(dx,dy)]|^2 \quad . \end{aligned} \tag{3-33}$$

From Fig. 3.4 we know that P(u,v) is $\pi/2$ ahead of H(u,v) for all (u,v). It is well known that phase information is generally more important than amplitude for holograms made from diffused objects [3-16,3-17] and two reconstructions will resemble each other if their phases are identical. Therefore the noise term p(x,y) is similar to h(x,y) except it is $\pi/2$ ahead of h(x,y). An artificial object consisting of a bright letter P on a dark background was constructed. The inverse transform of the parity term P(u,v) is shown in Fig. 3.13 and it is similar to the object. Therefore we have

$$jp(x,y) \simeq -h(x,y). \tag{3-34}$$

Comparing sinc(dx,dy) with $W_p(x,y)$ in Figs. 3.10-3.12, we know that these two functions are in phase for $x < 0$ and out of phase for $x > 0$, therefore Eq. (3-33) is

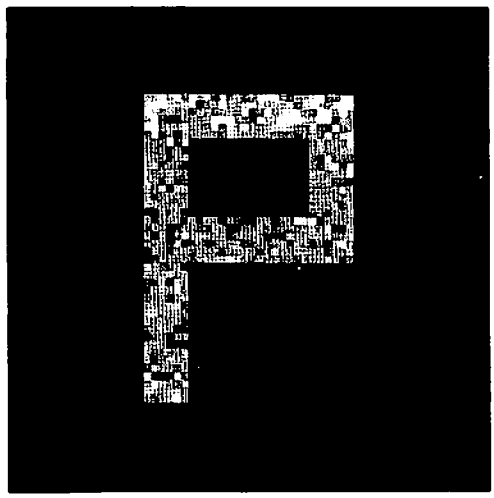

Fig. 3.13 Inverse Fourier transform of parity term P(u,v) associated with the phase coded object h(x,y), letter P

approximately zero at the -1,-2,...,-(n-1) orders and nonzero at the +1,+2,...,+(n-1) orders along the x direction.

3.2.4 Dual method

Further study of the relationship between H(u,v) and P(u,v) has found that we can exchange the roles of H and P. That is, if we consider p(x,y) as the desired object and use it to make the DPH then we will obtain the reconstruction h(x,y) at the high order of the x direction instead of at the zero order (0,1). Referring to Fig. 3.4, we can express P as

$$P = (1-A^2)^{\frac{1}{2}}\exp[j(\theta+\pi/2)]. \tag{3-35}$$

|P| varies from 1 to 0 as A varies from 0 to 1. Now we consider P as the desired function and find its parity term, Q. Using Eq. (3-35) again, we have

$$\begin{aligned} Q &= \sqrt{1-(\sqrt{1-A^2})^2}\; e^{j[(\theta+\pi/2)+\pi/2]} \\ &= -Ae^{j\theta} = -H. \end{aligned} \tag{3-36}$$

The inverse transform of Q is

$$q = \mathfrak{F}^{-1}\{Q\} = -\mathfrak{F}^{-1}\{H\} = -h \tag{3-37}$$

and

$$|q|^2 = |h|^2. \tag{3-38}$$

The reconstruction of the parity term is exactly the desired object as before. Thus we may say that H and P are the parity terms of each other. If we use P(u,v) to make a DPH then the desired object h(x,y) appears at the +n order (n,1) when 2n subcells are used and the original parity noise p(x,y) appears at the zero order (0,1). This can serve as an experimental proof of the above analysis since when P(u,v) is used in a DPH its noise term h(x,y) is known and can be distinguished easily.

The original decomposition of H(u,v) into the sum of two constant vectors is expressed in Eqs. (3-1) and (3-2). Repeating the same procedure for P(u,v), we get

$$P = \frac{1}{2} e^{j(\theta+\pi/2+\psi')} + \frac{1}{2} e^{j(\theta+\pi/2-\psi')} \tag{3-39}$$

where

$$\psi' = \cos^{-1}|P| = \cos^{-1}\sqrt{1-A^2} = \pi/2-\psi. \tag{3-40}$$

Therefore the two constant vectors have directions

$$\theta_1' = \theta+\pi/2+\psi' = \theta-\psi+\pi = \theta_2+\pi \tag{3-41}$$

$$\theta_2' = \theta+\pi/2-\psi' = \theta+\psi = \theta_1 \tag{3-42}$$

where $\theta_1 = \theta + \psi$ and $\theta_2 = \theta - \psi$ are the directions of H_1 and H_2 (Fig. 3.4). θ_1' and θ_2' are immediately available from θ_1

and θ_2 without going through the decomposition formula. The vectors in the θ_1', θ_2' directions are shown in Fig. 3.14 along with those in the θ_1, θ_2 directions. We shall refer this method as method II and the original method as method I.

3.3 Comparisons of methods I and II

As we just discussed the DPH can be made in two ways. In method I, we use H(u,v) to make the DPH and the reconstruction appears at the zero order (0,1) while in method II we use P(u,v) to make the DPH and the reconstruction is at the nth order (n,1) when 2n subcells are used. One advantage of method II is that the desired object is far removed from the central bright spot which may appear like an Airy pattern or a cross pattern when the black part of the hologram is not totally opaque. However we still have to compare the light efficiency and the signal-to-noise (S/N) ratio of these two methods.

In method I the reconstruction and the noise terms are given by Eqs. (3-17) and (3-28)

$$h_s(x,y) = d^2 W_h(x,y)\,[h(x,y) * \mathrm{comb}(dx,dy)] \qquad (3\text{-}17)$$

and

$$p_s(x,y) = jd^2 W_p(x,y)\,[p(x,y) * \mathrm{comb}(dx,dy)] \qquad (3\text{-}28)$$

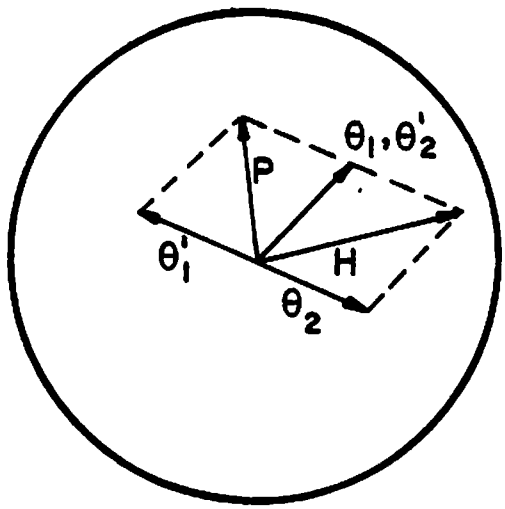

Fig. 3.14 Decomposed vectors for H(u,v) and P(u,v)

respectively, where $W_h(x,y)$ and $W_p(x,y)$ are the weighting functions defined by Eqs. (3-18) and (3-29). For method II we have the same result with the exchange of $h(x,y)$, $p(x,y)$ and $h_s(x,y)$, $p_s(x,y)$ in Eqs. (3-17) and (3-28). Since we are considering the first order in the y direction only and the effect of finite cell size in the y direction has been precompensated in the same way for both cases, we may redefine Eqs. (3-17) and (3-28) as one-dimensional functions

$$h_s(x) = dW_h(x)\,[h(x) * \mathrm{comb}(dx)] \tag{3-43}$$

and

$$p_s(x) = jdW_p(x)\,[p(x) * \mathrm{comb}(dx)] \tag{3-44}$$

with

$$W_h(x) = \mathrm{sinc}(dx), \tag{3-45}$$

and

$$W_p(x) = \frac{(-1)^n}{n}\,\mathrm{sinc}(dx/2n)\,[\sin\phi - \sin 3\phi + \ldots + (-1)^{n-1}\sin(2n-1)\phi] \tag{3-46}$$

where $\phi = \pi dx/2n$.

Before making the hologram, we have to normalize the Fourier transform in order to fit the maximum value of the

hologram. In methods I and II, the object is attenuated by different weighting functions and is therefore precompensated differently. Thus the Fourier transforms for these two methods and therefore the normalizations are no longer the same. This would essentially affect the reconstruction efficiency. However to simplify the analysis we will neglect this difference especially when the object is phase coded. Therefore the efficiency is affected by the weighting functions only. Since the object is precompensated, the efficiency can be determined by the value at the center of the reconstruction order. For method I, the efficiency η_1 is given by

$$\eta_1 \propto |W_h(0)| = 1 \quad . \tag{3-47}$$

For method II, the object appears in the +n order (n,1) and the efficiency is given by

$$\eta_2 \propto |W_p(n/d)| = \text{sinc}(1/2) = 2/\pi \approx 0.64 \quad . \tag{3-48}$$

Besides the efficiency, we also have to consider the signal-to-noise (S/N) ratio. We define the signal as the efficiency η and the noise as the noise term at the order of reconstruction. Specifically we define the noise as the maximum absolute value of the noise term at the order of reconstruction. That is,

$$S/N = \eta/|N|_{max} \tag{3-49}$$

where N is the noise term (the reconstruction of the parity term). To simplify the analysis, we further make an assumption that the energy of h(x,y) and p(x,y) is approximately the same and therefore the S/N is affected by the weighting functions only.

Both a sinc function and the functions $W_p(x)$ shown in Figs. 3.10-3.12 reach a local maximum near the boundaries of the reconstructed image in the order of interest. For simplicity, we will use the value of $|N|$ at the boundary as an approximation to $|N|_{max}$ and denote the value by $|N|$.

In method I we have

$$|N_1| \propto |W_p(\frac{1}{2d})| = |\frac{1}{n}\mathrm{sinc}(\frac{1}{4n})\{\sin(\pi/4n)-\sin(3\pi/4n)+\ldots +(-1)^{n-1}\sin((2n-1)\pi/4n)\}| \quad (3\text{-}50)$$

and

$$(S/N)_1 = \eta_1/|N_1| \quad . \quad (3\text{-}51)$$

In method II, noise is weighted by $W_h(x)$,

$$|N_2| = \max(|W_h(\frac{n}{d}-\frac{1}{2d})|, |W_h(\frac{n}{d}+\frac{1}{2d})|) \quad (3\text{-}52)$$

$$|W_h(\frac{n}{d}-\frac{1}{2d})| = |\mathrm{sinc}(n-1/2)| = \frac{1}{\pi(n-1/2)} \quad . \quad (3\text{-}53)$$

Similarly,

$$|W_h(\frac{n}{d} - \frac{1}{2d})| = \frac{1}{\pi(n+1/2)} \quad . \tag{3-54}$$

Therefore

$$|N_2| \propto \frac{1}{\pi(n-1/2)} \tag{3-55}$$

and

$$(S/N)_2 = \eta_2/|N_2| \propto 2n-1 \quad . \tag{3-56}$$

Table 3.1 is a list of η_1, $|N_1|$, $(S/N)_1$, η_2, $|N_2|$, $(S/N)_2$, and $(S/N)_1/(S/N)_2$ for different values of n. Method I has a better efficiency than method II by a factor of 1.5 approximately. Method I also has a better S/N for small n but the two methods have comparable S/N when n increases as indicated in the last column. Therefore method I is better than method II in terms of light efficiency and S/N. The table also indicates that S/N gets larger in both methods when n increases. Therefore, given a fixed number of resolution points in each cell, it is preferable to use as many subcells as possible so long as the subcells can be faithfully generated by plotting and photoreduction.

3.4 Corrected phase double-phase hologram

In Section 3.2, the phase quantities H_1 and H_2 in the subcells are determined by the decomposition of the Fourier

TABLE 3.1 COMPARISONS OF DIFFRACTION EFFICIENCY AND S/N FOR METHODS I AND II

n	η_1	$\|N_1\|$	$(S/N)_1$	η_2	$\|N_2\|$	$(S/N)_2$	$(S/N)_1/(S/N)_2$
1	1.000	0.637	1.571	0.637	0.637	1.000	1.571
2	1.000	0.264	3.792	0.637	0.212	3.000	1.264
4	1.000	0.127	7.897	0.637	0.091	7.000	1.128
8	1.000	0.063	15.949	0.637	0.042	15.000	1.063
16	1.000	0.031	31.974	0.637	0.021	31.000	1.031
32	1.000	0.016	63.987	0.637	0.010	63.000	1.016

transform at the center of each cell. This implementation results in a superposition of the desired reconstruction and the parity noise each weighted by different functions. The effect of the parity noise can be reduced by using more subcells and this requires more resolution points on the display device.

Instead of using values of H_1 and H_2 at the center of each cell we can use the corresponding value at the center of each subcell. We will show that this method produces the exact reconstruction without the interference of the parity noise. Since the reconstruction is exact we only need two subcells in the implementation and can relax the need for a high resolution display device in making the hologram.

Using the corresponding values of H_1 and H_2 in each subcell, Eq. (3-23) becomes

$$\begin{aligned} H_s''(u,v) = {} & \{[H(u,v)+P(u,v)]\cdot[\frac{1}{d^2}\mathrm{comb}(u/d,v/d)*\delta(u+d/4)]\} \\ & *\mathrm{rect}(\frac{u}{d/2},\frac{v}{d}) \\ & +\{[H(u,v)-P(u,v)]\cdot[\frac{1}{d^2}\mathrm{comb}(u/d,v/d)*\delta(u-d/4)]\} \\ & *\mathrm{rect}(\frac{u}{d/2},\frac{v}{d}) \end{aligned} \qquad (3\text{-}57)$$

and its inverse Fourier transform $h_s''(x,y)$ is given by

$$
\begin{aligned}
h_s''(x,y) &= \{[h(x,y)+p(x,y)]*[\mathrm{comb}(dx,dy)\cdot e^{-j2\pi xd/4}]\} \\
&\quad \cdot\frac{d^2}{2}\,\mathrm{sinc}(dx/2,dy)+\{[h(x,y)-p(x,y)] \\
&\quad *[\mathrm{comb}(dx,dy)\cdot e^{j2\pi xd/4}]\}\cdot\frac{d^2}{2}\,\mathrm{sinc}(dx/2,dy) \\
&= \frac{1}{2}\{\sum_{m,n=-\infty}^{\infty}\sum [h(x-m/d,y-n/d)+p(x-m/d,y-n/d)] \\
&\quad \cdot e^{-j\pi m/2}+[h(x-m/d,y-n/d)-p(x-m/d,y-n/d)] \\
&\quad \cdot e^{j\pi m/2}\}\cdot\mathrm{sinc}(dx/2,dy) \quad .
\end{aligned}
\tag{3-58}
$$

Recall that these derivations are based on the assumption that we are looking along the direction of the first diffraction order in y. Therefore we can assume n = 0 in Eq. (3-58). Then for the zero order along the x direction, m = 0, we have

$$
h_0(x,y) = h(x,y)\,\mathrm{sinc}(dx/2,dy) \tag{3-59}
$$

In fact we can show that if $h_m(x,y)$ is the mth diffraction order along the x direction then

$$
h_m(x,y) = \begin{cases}
h(x-m/d,y)\,\mathrm{sinc}(dx/2,dy) & \mathrm{Mod}(m,4) = 0 \\
-jp(x-m/d,y)\,\mathrm{sinc}(dx/2,dy) & \mathrm{Mod}(m,4) = 1 \\
-h(x-m/d,y)\,\mathrm{sinc}(dx/2,dy) & \mathrm{Mod}(m,4) = 2 \\
jp(x-m/d,y)\,\mathrm{sinc}(dx/2,dy) & \mathrm{Mod}(m,4) = 3
\end{cases}
\tag{3-60}
$$

At the zero order (0,1) we obtain the reconstruction exactly except for the attenuation factor, sinc(dx/2,dy), which can be easily precompensated. In this method we use

only two subcells in each cell rather than using more subcells to get a better reconstruction as in the previous method. If we wish to divide the cell into 2n subcells as before, then it can be shown that Eq. (3-60) becomes

$$h_m(x,y) = \begin{cases} h(x-nm/d,y)\,\mathrm{sinc}(dx/2n,dy) & \mathrm{Mod}(m,4) = 0 \\ -jp(x-nm/d,y)\,\mathrm{sinc}(dx/2n,dy) & \mathrm{Mod}(m,4) = 1 \\ -h(x-nm/d,y)\,\mathrm{sinc}(dx/2n,dy) & \mathrm{Mod}(m,4) = 2 \\ jp(x-nm/d,y)\,\mathrm{sinc}(dx/2n,dy) & \mathrm{Mod}(m,4) = 3 \end{cases} . \quad (3\text{-}61)$$

The noise term is removed to the nth order (n,1) while no spurious images appear in between. The method II described in Section 3.2.4 can also be applied here. That is, we can exchange the roles of H(u,v) and P(u,v) to obtain the reconstruction at the nth order. Proper precompensation has to be applied here too.

The hologram described in this section will be called the corrected phase DPH since it uses the corresponding values of H_1 and H_2 at the center of each subcell. However due to the use of the detour-phase technique the slit is no longer at the center of each subcell and this method is still an approximation in the v direction. Improvement is possible if an interpolation method is used to determine the phase at the actual slit position [3-18]. The result in Section 3.5 shows that the corrected phase DPH does produce good reconstructions.

It is worth noting that if the same method is applied to Chu and Fienup's "synthetic coefficient hologram" [3-12], then we do get the correct phase representation and the image quality is improved.

The additional Fourier components required in this method can be obtained by using the translation property of the Fourier transform as discussed by Chavel and Hugonin [3-19] and also in Section 4.3.

3.5 Experimental results

We have performed experiments to verify the above analysis. Each hologram consists of an array of 64 x 64 cells with 32 quantization levels in each cell. Holograms were recorded on a 4" x 5" sheet of Kodak SO-115 by using a Dicomed D-47 Image Recorder and then photoreduced to 2 cm x 2 cm on Kodak High Resolution Plate (HRP) type 2A. All the holograms have been precompensated for the distortion due to the finite size of the cell and the different order at which reconstruction appears as discussed in Section 3.2.3. Figure 3.15 shows two typical DPH's with two subcells and four subcells.

The reconstruction results for DPH's with zero phase and with random phase are shown in Fig. 3.16 and Fig. 3.17. The one with zero phase suffers from severe quantization

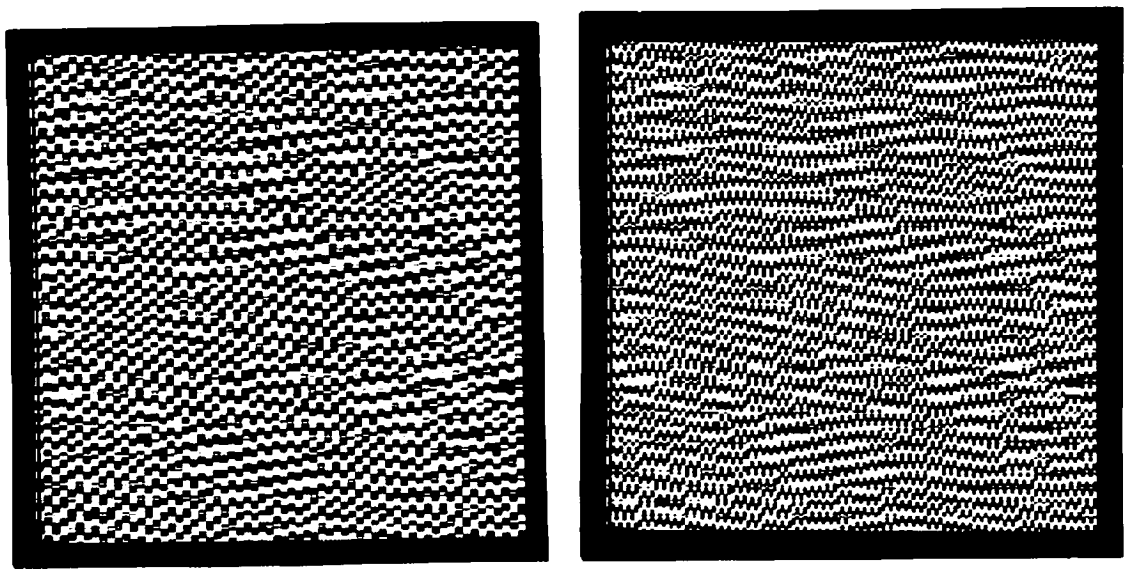

(a) 2 subcells (b) 4 subcells

Fig. 3.15 Double-phase holograms

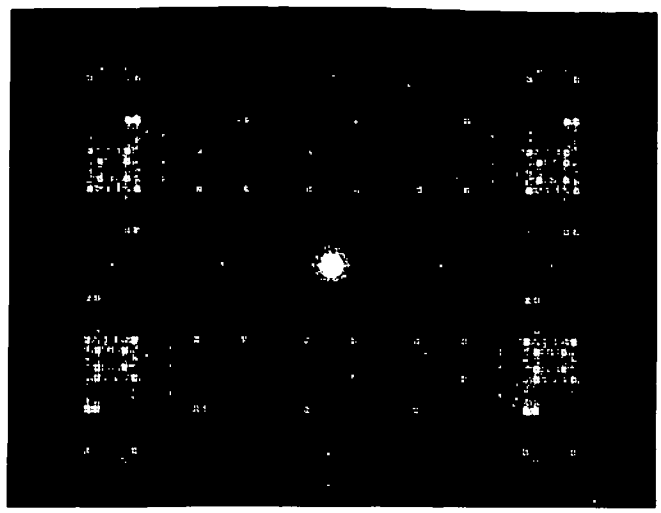

Fig. 3.16 Reconstruction of a DPH with zero phase

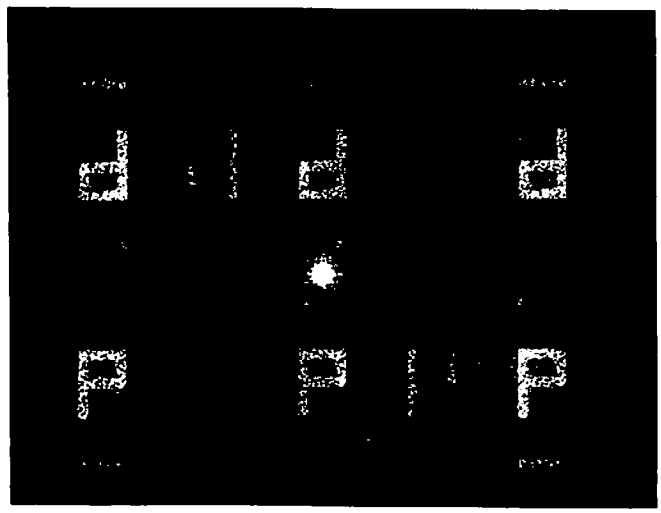

Fig. 3.17 Reconstruction of a DPH with random phase

error. When using random phase, the image quality becomes comparable with the Lohmann hologram (Fig. 3.18) while the intensity is stronger. In recording these results we have used different exposure times in order to get a similar intensity appearance on the prints. In order to demonstrate the phase coding results discussed in Chapter 2, we have implemented some DPH's with the results of phase coding. Figure 3.19 is the reconstruction from a DPH when the space-transform iterative phase coding method with constant spectrum is used. This result appears similar to Fig. 3.17 due to the aliasing error present in both. Figure 3.20 uses a spectrum with a bandwidth of 32 x 32 points out of a 64 x 64 array. The image is considerably improved at the expense of a lower light efficiency. Figure 3.21 has a bandwidth of 64 x 64 out of a 128 x 128 array and only the central portion is used in plotting. The image quality remains the same as in Fig. 3.20 while the light efficiency is improved.

To demonstrate the effect of using a different number of subcells in the hologram, we used the constrained spectrum of 32 x 32 points out of 64 x 64 array in order to reduce the effect of aliasing error. Figures 3.22-3.24 are the results of DPH's with two, eight, and sixteen subcells respectively and Fig. 3.20 is the result of four subcells. For the DPH with sixteen subcells, the noise term appears

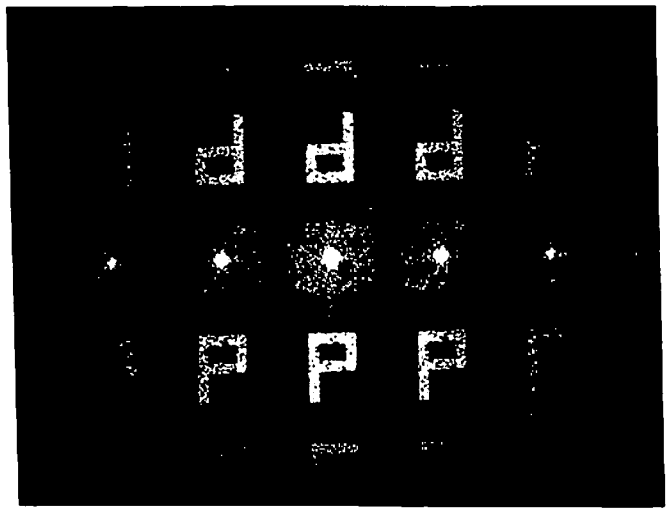

Fig. 3.18 Reconstruction of a Lohmann hologram with random phase

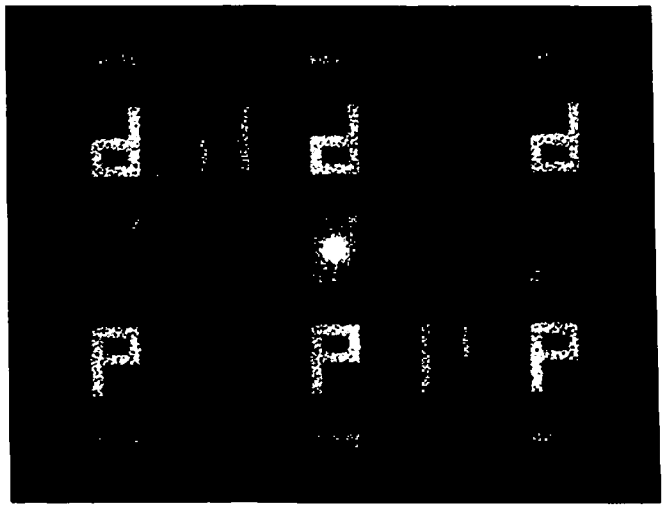

Fig. 3.19 Reconstruction of a DPH with the space-transform iterative phase coding method (constant spectrum)

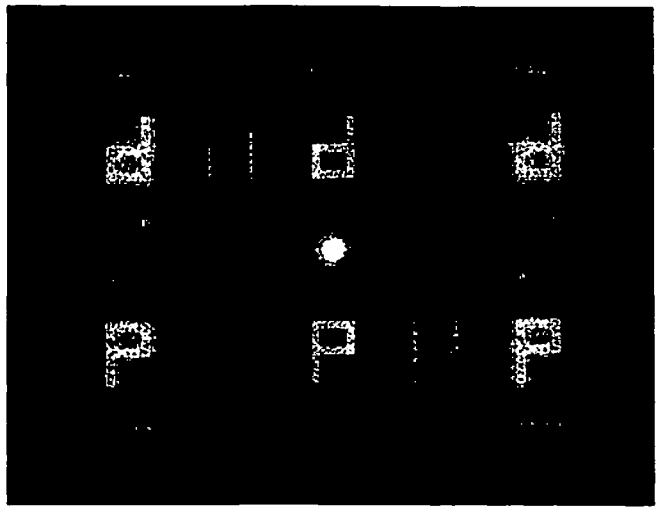

Fig. 3.20 Reconstruction of a DPH with the sapce-transform iterative phase coding method (constrained bandwidth, 32×32 out of 64×64)

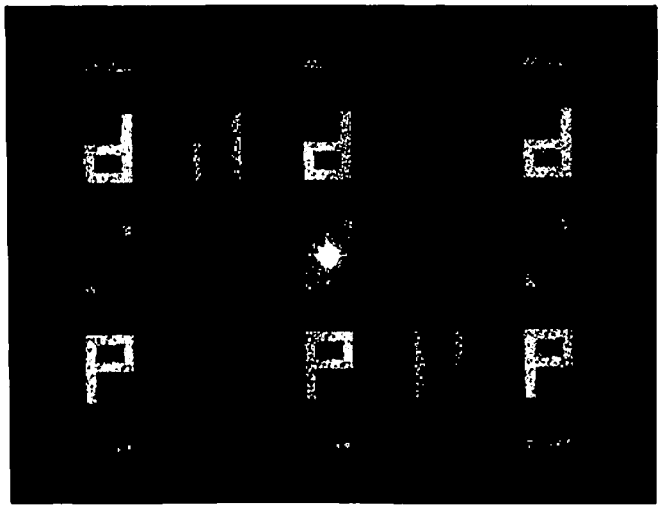

Fig. 3.21 Reconstruction of a DPH with the space-transform iterative phase coding method (constrained bandwidth, 64×64 out of 128×128 and plotting 64×64)

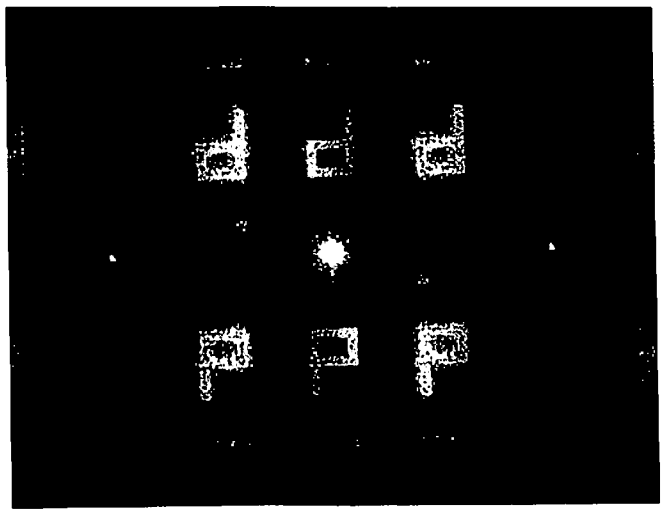

Fig. 3.22 Reconstruction of a DPH with 2 subcells

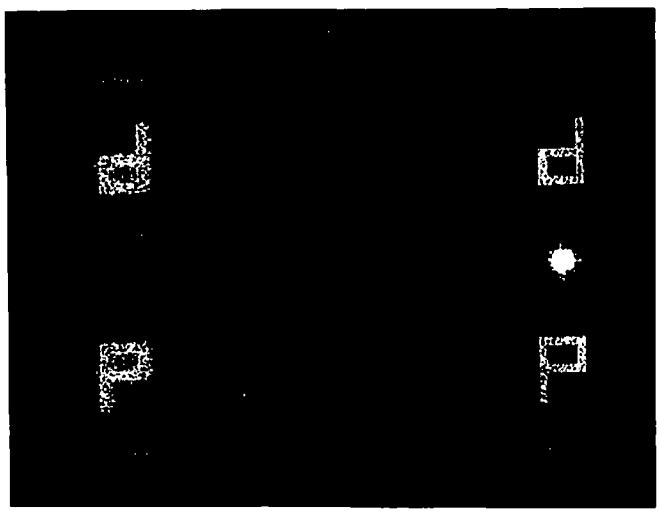

Fig. 3.23 Reconstruction of a DPH with 8 subcells

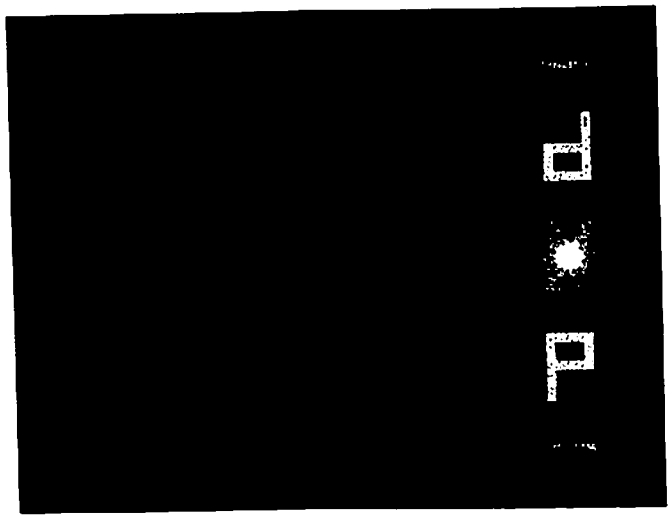

Fig. 3.24 Reconstruction of a DPH with 16 subcells

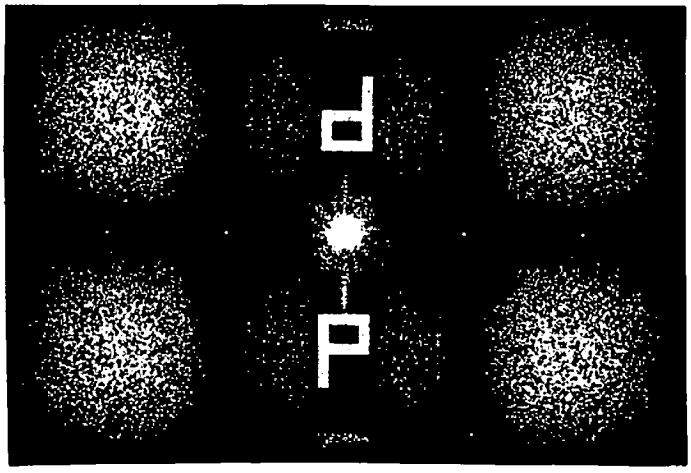

Fig. 3.25 Reconstruction of a DPH with randomly chosen parity term

at the eighth order and is not shown in Fig. 3.24.

As shown in Fig. 3.13, the reconstruction of the parity term resembles the object if the object is phase coded. However, in Fig. 3.4, we may pick -P(u,v) rather than P(u,v) as the parity term. In terms of the implementation, we may exchange the roles of H_1 and H_2 in Fig. 3.7. If we are allowed to choose the parity term for each cell independently then there are 2^{N^2} possible reconstructions of the parity term for an object of size N x N. The one shown in Fig. 3.13 is just one of them. If we randomly choose the parity term as P(u,v) or -P(u,v), then we should not expect the reconstruction of the parity term to have any structure. Figure 3.25 shows the reconstruction of the DPH with randomly chosen parity term. The reconstruction of the parity term appears like speckle noise. In this example since the desired object and the noise term are totally different, we can easily observe how these terms are weighted in different orders.

Figure 3.26 is the reconstruction of a DPH using method II which uses the parity term to make the DPH and therefore the reconstruction appears at the place where the noise term occurs in method I as described in Section 3.2.4. The desired image appears at the fourth order since eight subcells are used. Figure 3.27 shows the

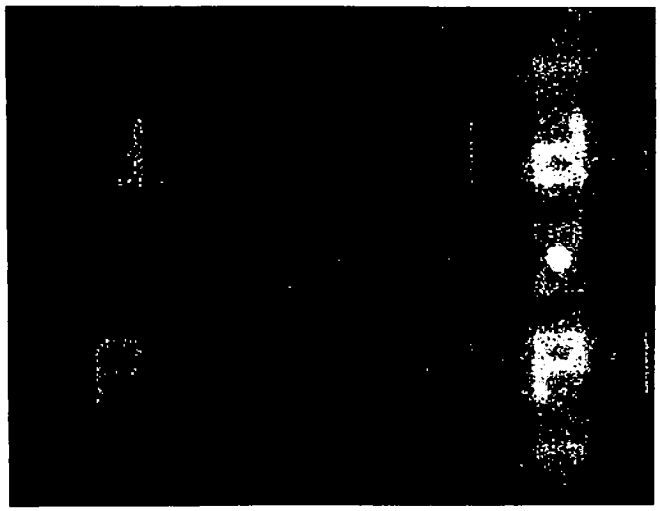

Fig. 3.26 Reconstruction of a DPH with method II (image appears at the fourth order)

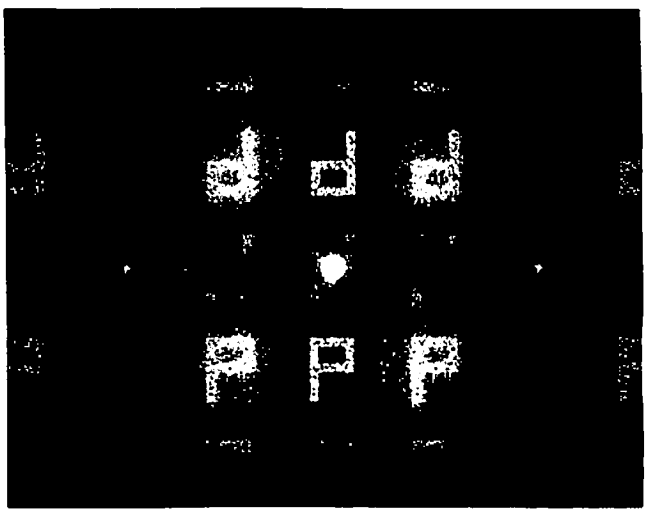

Fig. 3.27 Reconstruction of a corrected phase DPH with 2 subcells

reconstruction of the corrected phase DPH by using only two subcells. The improvement is evident as compared with the result in Fig. 3.22. The experimental results all agree with the analysis discussed in the previous sections.

3.6 Conclusions and discussions

In this chapter we have introduced a new way of making binary holograms in which two slits with constant area are used to represent each Fourier component. Each slit has exactly half the width of a Fourier resolution cell to increase the diffraction efficiency. When bleached, the light efficiency is increased by a factor of four, while the intensity of the central bright spot is reduced.

The two types of DPH's discussed which differ in that the reconstructions appear either at the zero order (0,1) or higher orders (n,1). The one at the zero order (0,1) is found to be superior in terms of light efficiency and S/N ratio. A consequence of the DPH method is a parity term which produces noise in the reconstruction. The effect of the parity term can be reduced by using more subcells or can even be eliminated by plotting the value of the hologram calculated for the center of each subcell rather than the overall cell center.

In order to get the same distance of separation between different orders along the x direction, the DPH requires twice the resolution of the Lohmann hologram. For example if we divide each cell of the DPH into 2n subcells, then the Lohmann hologram requires only n subcells. However, the original DPH needs only N^2 Fourier components (assuming an N x N object) while the Lohmann hologram as well as the corrected phase DPH require nN^2 Fourier components. Furthermore dividing the cell into n subcells reduces the ability to represent amplitude in the Lohmann hologram but does not affect the DPH at all since it contains only the phase information and amplitude is represented implicitly. Basically it is also possible to divide each cell into n subcells in the v direction (Fig. 3.9) and therefore move the reconstruction away from the central bright spot along the y direction. Unfortunately this would reduce the number of quantization level in phase. The phase information is known to be more critical to the reconstruction and therefore this method is not suitable for either a DPH or a Lohmann hologram. In terms of the separation of the reconstruction from the bright central spot, the method II of DPH is superior to the Lohmann hologram since it has a reconstruction at high order and is more suitable for a filtering system with a large input format.

The binary hologram is easy to make and has the advantage of high signal-to-noise ratio. However it works off-axis and has low diffraction efficiency. Furthermore the strong bright spot at the center is considered as an obstacle to the filtering operation. The binary hologram also requires more points to represent the amplitude and phase information for each Fourier component and therefore requires a large space-bandwidth product for the plotter and the recording material. In the following chapters we will study the on-axis holograms in order to overcome these problems.

CHAPTER 4

THE ON-AXIS OPTICAL FILTERING SYSTEM AND THE SUPPRESSION OF HIGH ORDERS

An off-axis hologram produces its desired output at the first diffraction order. This order has only a maximum diffraction efficiency of 10.13% when a square wave grating is used. Furthermore the strong spot at the center is usually not negligible. Thus if we use this hologram as a filter in a filtering system, we have to increase the carrier frequency or restrict the extent of the impulse response and the input in order to avoid overlapping between two adjacent diffraction orders.

The on-axis hologram, on the other hand, has more desirable properties. The output appears at the zero order which has high diffraction efficiency. Other high orders are strongly attenuated by the sinc function as the result of the finite cell size of the hologram. If these high orders can be further reduced or even eliminated properly, the whole output plane is available and the size of the input need not be restricted. The sampling rate of the filter then depends on the extent of the impulse response

rather than on the input extent which is generally much larger. In this chapter we will discuss an on-axis optical filtering system in general and investigate two methods of suppressing the high diffraction orders.

4.1 General discussion of an on-axis optical filtering system

Here we will discuss the on-axis optical filtering system, illustrate some different methods and then preview the ways of suppressing the high orders.

4.1.1 Analysis

To simplify the notation, we use one-dimensional variables in the following formulation. The complex filter $H_s(u)$ is designed to have the coherent impulse response $h(x)$ and the incoherent response $|h(x)|^2$ in the image plane. Denoting the Fourier transform of $h(x)$ by $H(u)$, the computer-generated hologram $H_s(u)$ approximates $H(u)$ by a series of weighted pulses

$$H_s(u) = \{[\sum_n H(nD)\,\delta(u-nD)] * p(u)\} \cdot M(u) \qquad (4\text{-}1)$$

shown in Fig. 4.1. The pulse spacing is D, each pulse has a shape $p(u)$ with weights given by the sampled values $H(nD)$. In general the pulse has a rectangular shape with width D, i.e.,

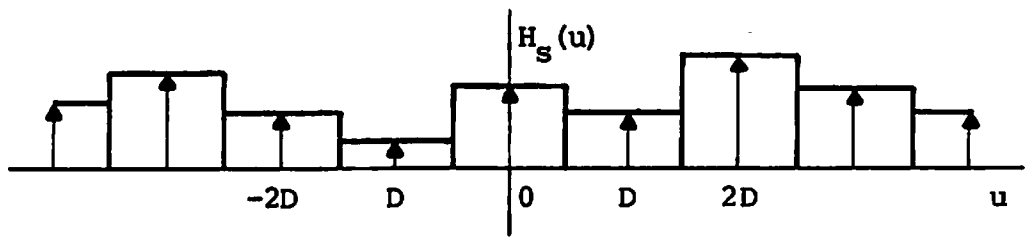

Fig. 4.1 Hologram profile if $p(u)=\text{rect}(\frac{u}{D})$

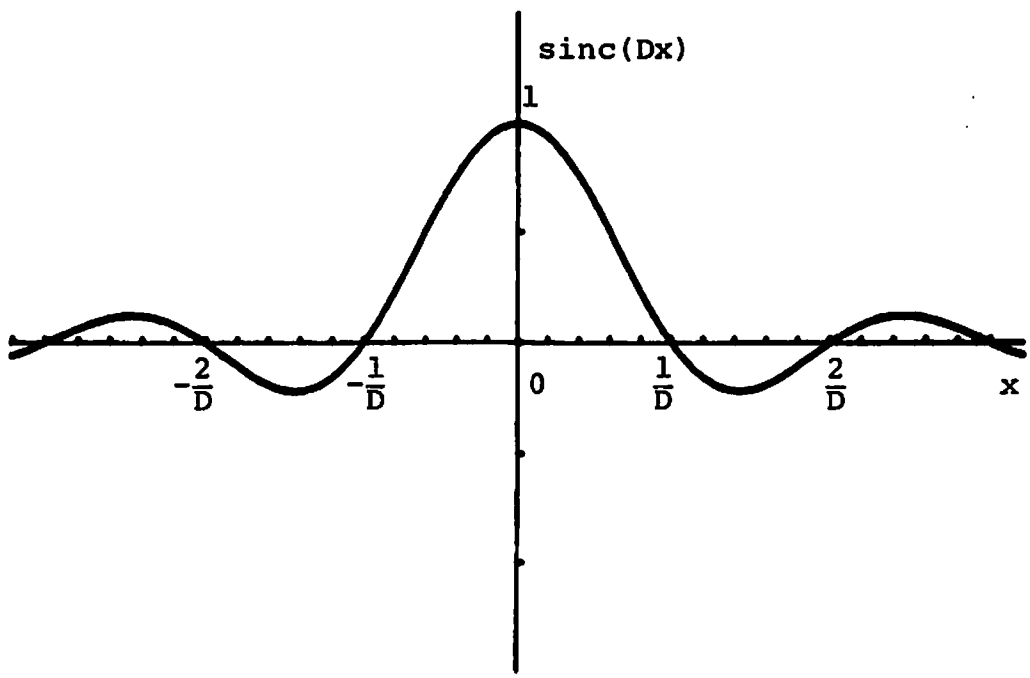

Fig. 4.2 Output weighting function if $p(u)=\text{rect}(\frac{u}{D})$

$$p(u) = \text{rect}(\frac{u}{D}) \quad . \tag{4-2}$$

The function M(u) is a mask representing the physical size limit of the hologram. If we assume that H(u) is bandlimited and the size of the hologram is large enough to cover the whole spectrum, then we may drop the mask function. Thus Eq. (4-1) becomes

$$H_s(u) = [H(u) \cdot \frac{1}{D}\text{comb}(\frac{u}{D})] * \text{rect}(\frac{u}{D}) \quad . \tag{4-3}$$

When this hologram is put in the filtering system we obtain the impulse response $h_s(x)$ which is the inverse Fourier transform of $H_s(u)$. Omitting the scale factor $1/\lambda f$ we have

$$\begin{aligned} h_s(x) &= \mathcal{F}^{-1}\{H_s(u)\} \\ &= [h(x) * \text{comb}(Dx)] \cdot D\text{sinc}(Dx) \quad . \end{aligned} \tag{4-4}$$

The total output is a displaced series of impulse responses of the form h(x), weighted by a sinc(Dx) factor as shown in Fig. 4.2. Notice that the higher diffraction orders fall on the zeroes of sinc(Dx) function and therefore are strongly attenuated. If these higher order responses can be neglected then the whole image plane is available. Therefore the size of the input object is no longer restricted and the sampling interval of the filter is determined by the extent of the impulse response X_n rather than by the extent of the input object X_0. We need

$$D < \frac{1}{X_n} \quad . \tag{4-5}$$

However, to properly eliminate the higher order response, we require the higher order responses to be concentrated around the zeroes of the sinc(Dx) function and D is generally smaller than the requirement imposed by Eq. (4-5).

If the higher order responses can not be neglected, the sampling rate must be much higher. To avoid overlapping between adjacent orders we require

$$D < \frac{1}{X_n + X_0} \quad . \tag{4-6}$$

Generally X_n is much smaller than X_0, so this condition becomes

$$D < \frac{1}{X_0} \quad . \tag{4-7}$$

The sampling interval is determined by the extent of the input object rather than the impulse response.

Besides the reduction of the high orders the sinc function also modifies the impulse response slightly due to the modulation near the peak of sinc(Dx), but this effect is small. If desired, the function h(x) could be precompensated by a window function correction term. The transform of

$$h'(x) = \frac{h(x)}{\mathrm{sinc}(Dx)} \qquad |x| < X_n/2 \qquad (4\text{-}8)$$

could be plotted so that h(x) would appear correctly.

4.1.2 Different on-axis holographic methods

To achieve on-axis complex operations, several methods have been proposed. The most straightforward method is to plot the amplitude and phase of the transfer function separately. The phase plot is bleached and then superimposed on the amplitude plot. The registration problem can be simplified by plotting grating patterns outside the aperture. The Moiré fringes produced by these patterns can be used for alignment. The sandwich of the two holograms is then permanently fixed together.

Other on-axis holograms including the kinoform [4-1] and the ROACH [4-2] have been used. Kinoforms are made by discarding the amplitude of the transform of a diffused object. Due to the lack of amplitude information, degradation occurs in the reconstruction. Besides using a random phase diffuser or deterministic diffuser [4-3] to even the spectrum, several iterative methods [4-2,4-4] can be used to achieve a flat spectrum as discussed in Chapter 2. These methods are convergent in general, however, we do not expect to get perfect reconstruction in a finite number of steps. Therefore instead of discarding

the slow amplitude variation of the spectrum, we may implement it as a sandwich hologram. Since the slowly varying amplitude has a low dynamic range, the limited dynamic range of the film is no longer a problem. The ROACH stores amplitude and phase information on different layers of color film. Basically it is a sandwich hologram without any registration problem.

4.1.3 Suppression of high orders

The on-axis holograms have the advantages of high diffraction efficiency and the high orders are strongly attenuated by the sinc function. However if the extent of the impulse response is not small, the orders adjacent to the zero order still have non-negligible energy. If the hologram is to be used in a filtering system the presence of these high orders limits the size of the input object to be filtered.

Lowenthal and Chavel [4-5,4-6] have proposed a two-step method to avoid these high orders. First they made a computer-generated binary hologram. Then they put it in a band-pass filtering system and selected the desired order. In the output plane the desired wave is interfered with a reference wave and recorded on holographic material. Basically this method still has a limitation on the input object size which depends on the offset of the reference

wave. Furthermore due to the interference involved in the procedure, the holographic material has to have a high space-bandwidth product and a very stable and low noise photographic recording is also essential.

One straightforward way of alleviating the problem of high orders is to surround the impulse response by a large zero array and therefore leave a large space between different orders for the input object. If this large array needs some intermediate processing, for example the phase coding discussed in Chapter 2, then the use of a big array with most of the elements being zero simply wastes computation time and memory. In the next two sections, we will propose two methods to solve this problem. One is to effectively increase the cell size by precombining the components in the transform domain and therefore reducing the intensity in the high orders. The second method is to interpolate the hologram so that the carrier frequency is effectively increased. There are several possible interpolation techniques which can be used in this method. It will be shown that the one using the shift property of the Fourier transform produces the best results and it is the same result as obtained by surrounding the impulse response by a large zero array without handling that large array directly.

It is worth noting that these two methods can also be applied to the off-axis holograms. In next chapter, a method of making continuous holograms will be discussed. The continuous hologram will produce a zero order output only and essentially eliminate the problem mentioned above.

4.2 Cell size expansion method

4.2.1 Analysis

Here we study how to suppress the high orders by modifying the cell size or its profile. Again, for simplicity, we use one-dimensional variables in the following analysis as in Section 4.1.1.

The hologram can be expressed mathematically as in Eq. (4-3)

$$H_s(u) = [H(u) \cdot \frac{1}{D}\mathrm{comb}(\frac{u}{D})] * \mathrm{rect}(\frac{u}{D}) \quad . \qquad (4\text{-}3)$$

The impulse response $h_s(x)$ is given by Eq. (4-4) and can be rewritten as

$$h_s(x) = DW_h(x)\,[h(x) * \mathrm{comb}(Dx)] \qquad (4\text{-}9)$$

where

$$W_h(x) = \mathrm{sinc}(Dx) \qquad (4\text{-}10)$$

is the weighting function. Figures 4.1 and 4.2 show the

hologram cell profile and the weighting function $W_h(x)$. Even though high orders are strongly attenuated by the weighting function, the residues at the ± 1 orders are not negligible. This limits the size of the input to be filtered. Further suppression of high orders can be achieved by using a triangular function of width 2D in Eq. (4-3). This results in a linear interpolation of the sampled data and the weighting function becomes $\text{sinc}^2(Dx)$. Fig. 4.3 shows the profile of the hologram and the weighting function. Now the higher orders are better suppressed by the $\text{sinc}^2(Dx)$ function. However the hologram shown in Fig. 4.3(a) requires an infinite number of resolution points to get a continuous curve. Therefore it has to be approximated by many rectangular pulses. If finer resolution is available we can simply sample the hologram finer and use rectangular pulses. We then increase the carrier frequency and move the high orders further away. Therefore the configuration shown in Fig. 4.3(a) does not look practical.

We can also replace the rect function in Eq. (4-3) by another rect function of width 2D. The weighting function then becomes sinc(2Dx) and is shown in Fig. 4.4 along with the hologram profile. The weighting function is a narrower sinc function. The first order impulse response now falls on the second zero of the sinc function and is suppressed

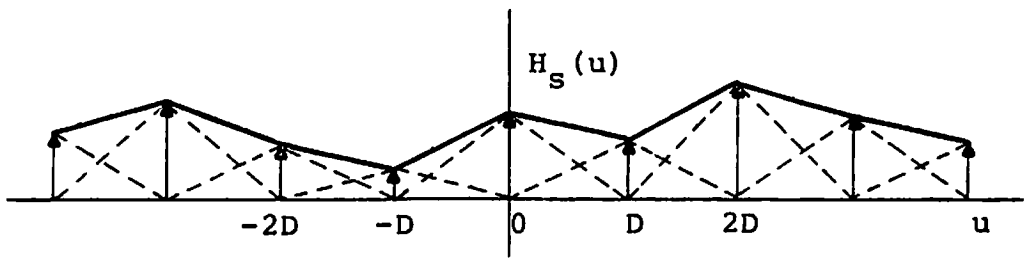

(a) hologram profile

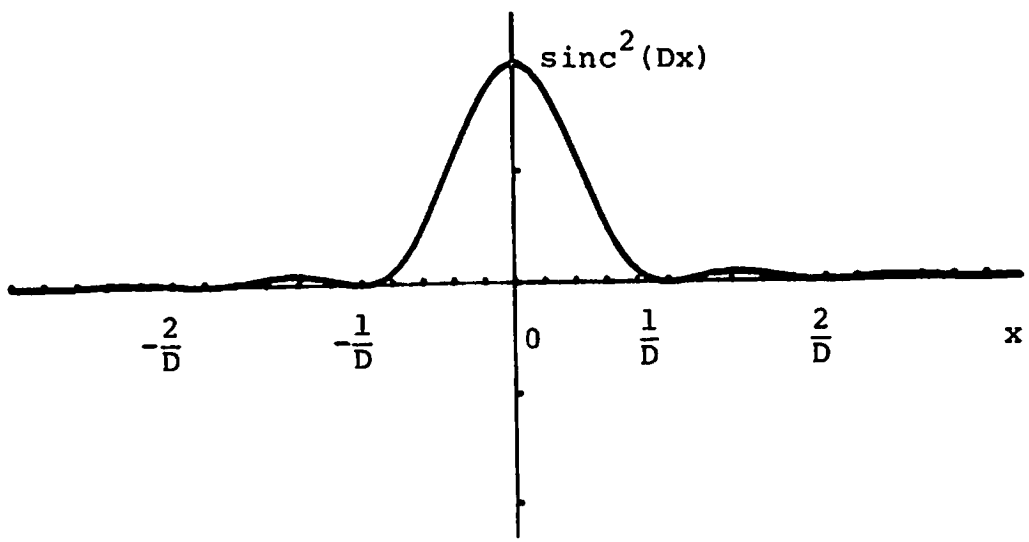

(b) output weighting function

Fig. 4.3 Hologram and output for $p(u)=\Lambda(\frac{u}{D})$

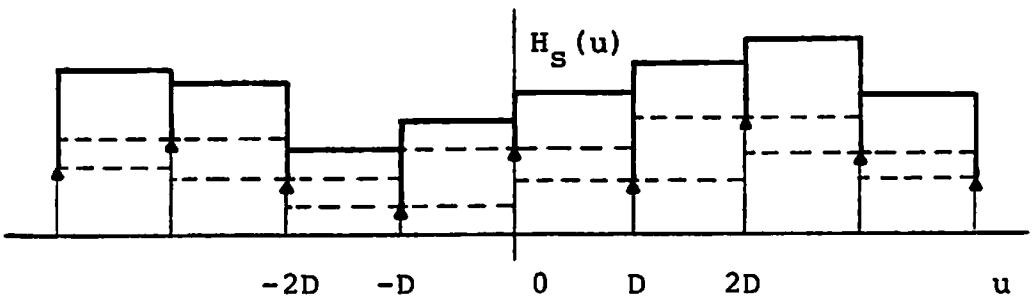

(a) hologram profile

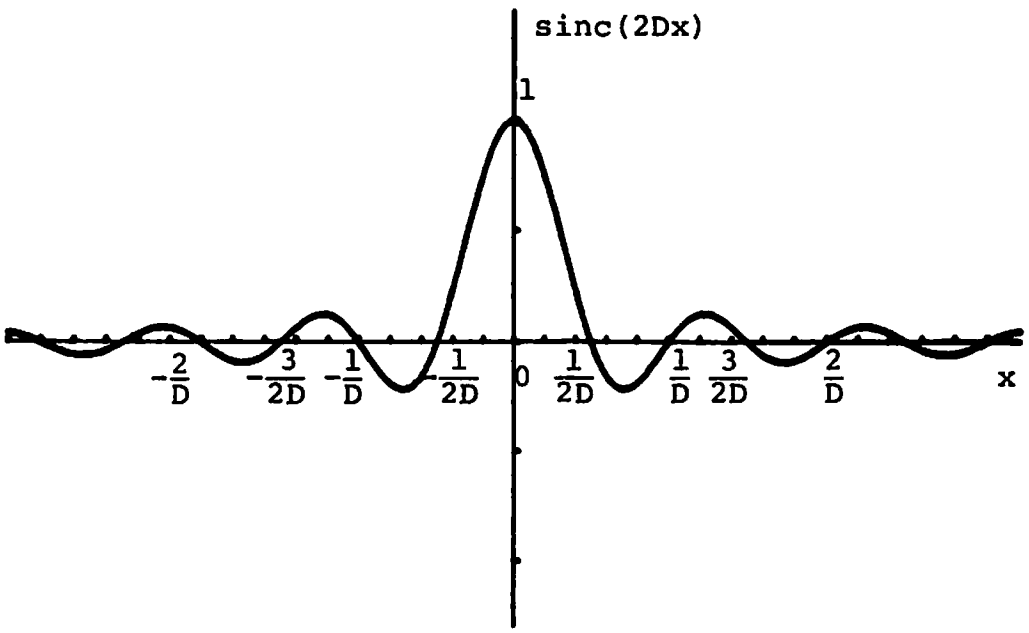

(b) output weighting function

Fig. 4.4 Hologram and output for $p(u)=\text{rect}(\frac{u}{2D})$

more. One nice property of this method is that the resolution requirement on the hologram remains the same. As shown in Fig. 4.4(a) the constant amplitude area is now between two impulses instead of centered at the impulse although the width remains the same. The value between two impulses is the summation of the two combined mathematically in advance and then plotted accordingly. In principle, if the desired quantity on the hologram, for example transmittance, is a linear function of the exposure, then we can obtain the desired quantity by double exposure. However these functions, transmittance or phase shift, are usually nonlinear functions of exposure. Even if they are linear functions of exposure we still do not get the correct result since the desired operation is complex addition rather than scalar addition. For example in the kinoform case we need $e^{j\theta_1}+e^{j\theta_2}$ instead of $e^{j(\theta_1+\theta_2)}$ and in the ROACH case we require $A_1e^{j\theta_1}+A_2e^{j\theta_2}$ rather than $(A_1+A_2)e^{j(\theta_1+\theta_2)}$. Therefore these quantities must be precombined mathematically.

Note that in Fig. 4.4(b) the sinc function not only attenuates higher orders but also distorts the desired impulse response. Similar distortion occurs in Fig. 4.2 but is less severe. This distortion can be precompensated by

$$h'(x) = \frac{h(x)}{\mathrm{sinc}(2Dx)} \qquad |x| < X_n/2 \quad . \quad (4\text{-}11)$$

However we have to limit the extent of the impulse response X_n since the weighting function reaches zero at the boundary ($x = \pm\frac{1}{2D}$) and $h'(x)$ is not defined.

We can use even wider rectangular functions and get better suppression. For example $\mathrm{rect}(\frac{x}{3D})$, $\mathrm{rect}(\frac{x}{4D}),\ldots,\mathrm{rect}(\frac{x}{nD})$ with the widths being multiples of D are all possible. The first order is at the third, fourth,..,nth zero respectively. However the extent of h(x) is then limited to 2/3, 1/2,...,2/n of the original maximum size due to the fact that the zeroes of the sinc function can not be precompensated. After precombination of the samples, the constant value area is now centered at the original impulses when the multiple is odd and is between impulses when the multiple is even. In any event the resolution requirement remains the same.

4.2.2 Signal-to-noise ratio

Although the expansion of the cell size suppresses the high orders better, it also distorts the zero order. This order can be precompensated in advance, however, this increases the high orders again. It is interesting to compare these methods.

Here we evaluate the cell size expansion method mathematically and compare the signal-to-noise ratio for different cell sizes. The quantities to be compared are the energy at the zero order and at the first order since they are the desired signal and the "noise" to be suppressed. Let us denote these two quantities by S_n and N_n where the subscript n indicates that these results are from the use of cell size nD. For each n we compare S_n/S_1 and $S_n/N_n/S_1/N_1$, the efficiency and the improvement of the signal-to-noise ratio.

For simplicity we assume that the impulse response is a rectangular function and this eliminates the energy dependence of particular impulse responses. The width of the rectangular function is limited to $\frac{2}{nD}$ which is twice the distance to the first zero of the sinc(nDX) function since the precompensation is impossible at the zeroes. Let $h_1(x)$, $h_2(x)$ be the compensated functions

$$h_1(x) = \frac{h(x)}{\text{sinc}(Dx)} \qquad (4\text{-}12)$$

$$h_n(x) = \frac{h(x)}{\text{sinc}(nDx)} \qquad n \neq 1 \quad . \qquad (4\text{-}13)$$

The domain of these two functions is limited to $(-\frac{1}{nD}, +\frac{1}{nD})$ so that no singularities occur.

Let $H_1(u)$, $H_n(u)$ be the Fourier transforms of $h_1(x)$ and $h_n(x)$ respectively. To make a hologram we have to normalize $H_1(u)$ and $H_n(u)$ to fit the maximum capability of the recording materials. Therefore we have $C_1H_1(u)$ and $C_nH_n(u)$ on the holograms where C_1, C_n are normalization constants. Now we make an assumption that the energy going through both holograms is the same if the impulse response is phase coded. This is a reasonable assumption since both holograms have similar average transmittances. By Parseval's theorem the reconstructions also have the same energy. That is,

$$\int |C_1H_1(x)\mathrm{sinc}(Dx)|^2dx = \int |C_nh_n(x)\mathrm{sinc}(nDx)|^2dx. \quad (4\text{-}14)$$

The appearance of the sinc function is due to the use of the rectangular cell. In this expression we also drop the high orders by assuming that most of the energy is at the zero order. Substituting Eqs. (4-12) and (4-13) in Eq. (4-14) we have

$$\int |C_1h(x)|^2dx = \int |C_nh(x)|^2dx. \quad (4\text{-}15)$$

Therefore

$$C_1 = C_n \quad (4\text{-}16)$$

and

$$S_1 = S_n = \int |C_1h(x)|^2dx \quad . \quad (4\text{-}17)$$

Hence the efficiency remains the same no matter how big the cell size is. For impulse response with zero phase, the above result is no longer true. Let A be the maximum amplitude on the hologram, then since the maximum of Fourier transform occurs at the zero frequency for zero phase impulse response, we have

$$C_1 = \frac{1}{H_1(0)} = \frac{A}{\int h_1(x)\,dx} = \frac{A}{\int \frac{h(x)}{\mathrm{sinc}(Dx)}\,dx} \tag{4-18}$$

$$C_n = \frac{A}{\int \frac{h(x)}{\mathrm{sinc}(nDx)}\,dx} \quad . \tag{4-19}$$

It follows that $C_1 > C_n$ instead of $C_1 = C_n$. However to simplify the analysis, we can either assume $C_1 = C_n$ or include this factor in the final result.

The energy of the first diffraction order for cell size nD is given by

$$N_n = \int_{(\frac{1}{D}-\frac{1}{nD})_+}^{(\frac{1}{D}+\frac{1}{nD})_-} |C_1 h_n(x-\tfrac{1}{D})\,\mathrm{sinc}(nDx)|^2 dx$$

$$= C_1^2 \int_{(-\frac{1}{nD})_+}^{(\frac{1}{nD})_-} |h_n(x)\,\mathrm{sinc}(nD[x+\tfrac{1}{D}])|^2 dx \tag{4-20}$$

$$= C_1^2 \int_{(-\frac{1}{nD})_+}^{(\frac{1}{nD})_-} \left|\frac{1}{\mathrm{sinc}(nDx)}\,\mathrm{sinc}(nD[x+\tfrac{1}{D}])\right|^2 dx$$

where $(\cdot)_-$ and $(\cdot)_+$ indicate the quantities slightly smaller and larger than $(\cdot)$ respectively in order to avoid the singularities. The last equality is the result of the assumption that h(x) is rect function. Equation (4-20) can be further simplified to

$$N_n = C_1^2 \int_{(-\frac{1}{nD})_+}^{(\frac{1}{nD})_-} \frac{(\pi nDx)^2}{\sin^2(\pi nDx)} \frac{\sin^2(\pi nDx+\pi n)}{[\pi nD(x+\frac{1}{D})]^2} dx$$

$$= C_1^2 \int_{(-\frac{1}{nD})_+}^{(\frac{1}{nD})_-} (\frac{Dx}{Dx+1})^2 dx \quad . \tag{4-21}$$

In order to compare the performance, we should have the same h(x) in Eq. (4-12). Therefore

$$N_1 = \int_{(\frac{1}{D}-\frac{1}{nD})_+}^{(\frac{1}{D}+\frac{1}{nD})_-} |C_1 h_1(x-\frac{1}{D})\,\mathrm{sinc}(Dx)|^2 dx$$

$$= C_1^2 \int_{(-\frac{1}{nD})_+}^{(\frac{1}{nD})_-} |h_1(x)\,\mathrm{sinc}(D[x+\frac{1}{D}])|^2 dx$$

$$= C_1^2 \int_{(-\frac{1}{nD})_+}^{(\frac{1}{nD})_-} |\frac{1}{\mathrm{sinc}(Dx)} \cdot \mathrm{sinc}(Dx+1)|^2 dx \tag{4-22}$$

$$= C_1^2 \int_{(-\frac{1}{nD})_+}^{(\frac{1}{nD})_-} \frac{(\pi Dx)^2}{\sin^2(\pi Dx)} \cdot \frac{\sin^2(\pi Dx+\pi)}{[\pi(Dx+1)]^2} dx$$

$$= C_1^2 \int_{(-\frac{1}{nD})_-}^{(\frac{1}{nD})_-} (\frac{Dx}{Dx+1})^2 dx = N_n \quad .$$

Hence we have

$$S_n/N_n = S_1/N_1 \quad . \tag{4-23}$$

This analysis shows that although the cell size expansion does suppress the high orders, the precompensation raises the energy again and both effects happen to cancel each other. Therefore no gain is obtained by using this method when the energy is of concern. In the case of zero phase impulse response the S/N is even worse.

4.2.3 Experimental results and conclusions

Although the analysis is based on the assumption of a complex hologram such as the ROACH, we demonstrate the result by the kinoform. A 64 x 64 array depicting the letter 'P' with random phase is chosen as an example. In order to see the effect of attenuation better we choose an expanded cell size to be four times the original size. Cells are precombined in complex value, then the amplitude is discarded in order to make a kinoform. Due to the use of random phase we do not expect too much degradation caused by the lack of amplitude information. These kinoforms are made on kodachrome 64 by the ROACH method, i.e., exposing the blue sensitive layer and green sensitive layer with the desired phase pattern and then flooding the red sensitive layer so that the developed film has only

phase delay effects for red light.

Figures 4.5 and 4.6 show the reconstruction of uncompensated and precompensated cases. In Fig. 4.5 the high orders are suppressed more while the zero order is also distorted severely. In Fig. 4.6 the zero order is restored while the higher orders come up again. Note that in the precompensated case, the letter has been truncated at the top and bottom in advance to avoid the singularity in the 1/sinc(4DX,4DY) function.

As these results and the previous analysis have shown, the cell expansion method does not work well in suppressing the high orders. However if the impulse response is very small compared with the whole array, then we do expect to have good high order suppression since they are around the zeroes of the sinc function.

4.3 Hologram interpolation with the DFT

As we discussed in Section 4.1.3, we can embed the impulse response in a large zero array in order to avoid the overlapping between adjacent orders in the output plane. This process is actually an oversampling in the transform domain and does not provide any further information at all. If certain intermediate processes are to be used (for example an iterative phase coding method

Fig. 4.5 Reconstruction of kinoform when $p(u,v)=\text{rect}(\frac{u}{4D},\frac{v}{4D})$ (uncompensated)

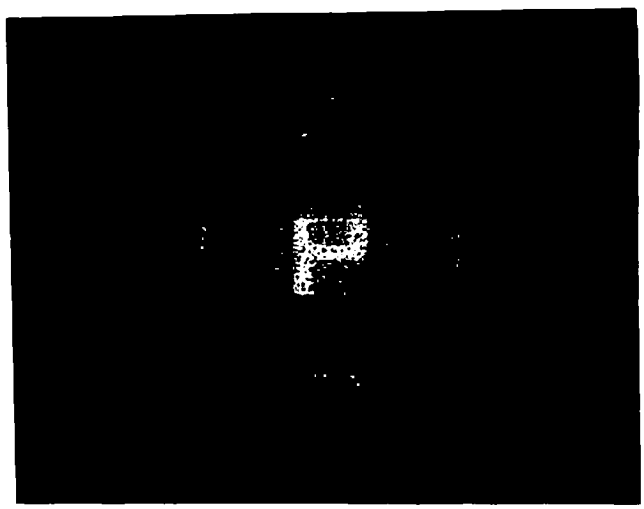

Fig. 4.6 Reconstruction of kinoform when $p(u,v)=\text{rect}(\frac{u}{4D},\frac{v}{4D})$ (precompensated)

discussed in Chapter 2), then the use of a large zero array not only wastes computation time but also requires more core as working space. Thus it is desirable to work on the original impulse response array of size N^2 and obtain a reconstruction of size $(MN)^2$ with the impulse response embedded in a zero array. Note that embedding the impulse response in a zero array does not change the original sampling values in the transform domain except for a constant factor. It simply fills in more points between the original sampling points. Since the zero array does not provide any new information, the new points in the transform domain should be determined by the original sampling points. This suggests that our goal can be achieved by interpolation in the transform domain.

In the study of computer-generated spatial filters for large object formats, Bartelt et al. [4-7] have used a step-and-repeat camera to interlace the binary hologram with itself so that the carrier frequency is increased. In the region between orders, however, false images appear which are suppressed by a weighting function

$$G(x,y) = \frac{\sin(\pi Dx)}{\sin(\pi Dx/M)} \cdot \frac{\sin(\pi Dy)}{\sin(\pi Dy/M)} \qquad (4\text{-}24)$$

where D is the cell size and M is the interlace number. Although the false images have been suppressed fairly well, noise still exists. In addition, if the hologram to be

interlaced is an on-axis type, for example ROACH, then after interlacing we still get back to the original hologram.

One other intuitive way is to use the shift property of the DFT [4-8,4-9]. The impulse response can be multiplied by a linear phase in order to get a translated Fourier transform. However, the reconstruction from this method has an impulse response slightly off-axis (see Appendix A). We found that instead of using the shift property of the discrete Fourier transform, we should use the same property associated with the continuous Fourier transform in order to get the desired result. We also realize that this method is actually a sinc function interpolation which has been claimed to be time consuming and not rigorous if we do not take into account an infinite number of terms. This method is explained thoroughly in the next section.

4.3.1 Theory

To simplify the mathematics we use a one-dimensional impulse response in this section. Extension to the two-dimensional case is straightforward.

Suppose the original impulse response has length N as shown in Fig. 4.7(a). The input sequences to the DFT, h_n

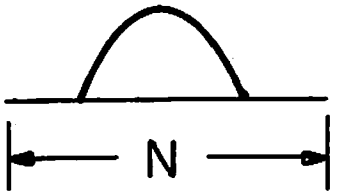

(a) impulse response

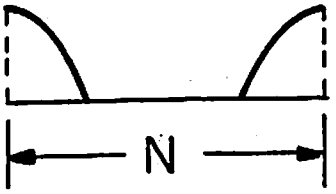

(b) input sequences to DFT, h_n, n=1,...,N-1

Fig. 4.7 Impulse response to be used in DFT interpolation

$n = 0,1,\ldots,N-1$, are shown in Fig. 4.7(b). Both figures are shown in continuous form although they are actually sampled. Now we want to make a hologram such that the reconstruction has the same impulse response surrounded by an MN zero array.

First of all we form M new inputs by multiplying the impulse response shown in Fig. 4.7(a) with different linear phases. For each m, $m = 0,\ldots,M-1$, the impulse response in (a) is multiplied by

$$e^{-j2\pi mn/MN} \qquad n = -\frac{N}{2},\ldots,0,\ldots,\frac{N}{2}-1 \quad (4\text{-}25)$$

Note that n is indexed from $-\frac{N}{2}$ to $\frac{N}{2}-1$. After shifted by half period as from Fig. 4.7(a) to (b), these new inputs can be expressed mathematically (see Appendix A) as

$$\begin{aligned} h_n^{(m)} &= h_n e^{-j2\pi m[(n+N/2)_{Mod N}-N/2]/MN} \\ &= h_n e^{-j2\pi m(n+N/2)_{Mod N}/MN} \cdot e^{j\pi m/M} \quad . \end{aligned} \qquad (4\text{-}26)$$

Then we compute the corresponding DFT $H_k^{(m)}$ for each $h_n^{(m)}$

$$H_k^{(m)} = \frac{1}{\sqrt{N}} \sum_{n=0}^{N-1} h_n^{(m)} e^{-j2\pi kn/N} \qquad \begin{matrix} k = 0,\ldots,N-1 \\ m = 0,\ldots,M-1 \end{matrix} \quad . \qquad (4\text{-}27)$$

A new sequence p_ℓ, $\ell = 0,\ldots,MN-1$ is formed by

$$P_\ell = H^{(m)}_{(\ell-m)/M} \qquad \text{where } m = Mod(\ell,M) \quad . \qquad (4\text{-}28)$$

We prove in the following that P_ℓ has the desired

properties mentioned above.

Proof:

Let Q_n be the inverse DFT of P_ℓ.

$$Q_n = (DFT)^{-1} P_\ell$$

$$= \frac{1}{\sqrt{MN}} \sum_{\ell=0}^{MN-1} P_\ell e^{j2\pi \ell n/MN} \quad . \tag{4-29}$$

Substituting Eq. (4-28) we have

$$Q_n = \sum_{m=0}^{M-1} \frac{1}{\sqrt{MN}} \sum_{k=0}^{N-1} H_k^{(m)} e^{j2\pi (Mk+m) n/MN}$$

$$= \sum_{m=0}^{M-1} \frac{1}{\sqrt{M}} \left[\frac{1}{\sqrt{N}} \sum_{k=0}^{N-1} H_k^{(m)} e^{j2\pi kn/N}\right] e^{j2\pi mn/MN} \quad . \tag{4-30}$$

Let

$$n = pN+n' \qquad \begin{matrix} n' = 0,\ldots,N-1 \\ p = 0,\ldots,M-1 \end{matrix} \tag{4-31}$$

$$Q_n = Q_{pN+n'}$$

$$= \sum_{m=0}^{M-1} \frac{1}{\sqrt{M}} \left[\frac{1}{\sqrt{N}} \sum_{k=0}^{N-1} H_k^{(m)} e^{j2\pi k(pN+n')/N}\right] \cdot e^{j2\pi m(pN+n')/MN} \tag{4-32}$$

$$= \sum_{m=0}^{M-1} \frac{1}{\sqrt{M}} \left[\frac{1}{\sqrt{N}} \sum_{k=0}^{N-1} H_k^{(m)} e^{j2\pi kn'/N}\right] \cdot e^{j2\pi mn'/MN} e^{j2\pi mp/M} \quad .$$

Using the inverse transform relationship of Eq. (4-27) and Eq. (4-26) we get

$$Q_{pN+n'} = \sum_{m=0}^{M-1} \frac{1}{\sqrt{M}} h_{n'}^{(m)} e^{j2\pi mn'/MN} e^{j2\pi mp/M}$$

$$= \sum_{m=0}^{M-1} \frac{e^{j\pi m/M}}{\sqrt{M}} [h_{n'} e^{-j2\pi m(n'+N/2)\,\mathrm{Mod}N/MN}] \cdot e^{j2\pi mn'/MN} e^{j2\pi mp/M} \quad . \tag{4-33}$$

Let us consider two cases of n'

(I) $n' = 0, \ldots, -1$

$$Q_{pN+n'} = \sum_{m=0}^{M-1} \frac{e^{j\pi m/M}}{\sqrt{M}} [h_{n'} e^{-j2\pi mn'/MN} e^{-j\pi m/M}] e^{j2\pi mn'/MN} e^{j2\pi mp/M}$$

$$= \frac{1}{\sqrt{M}} h_{n'} \sum_{m=0}^{M-1} e^{j2\pi mp/M} \quad . \tag{4-34}$$

Since

$$\sum_{m=0}^{M-1} X^m = \frac{1-X^M}{1-X} \tag{4-35}$$

we have

$$S = \sum_{m=0}^{M-1} e^{j2\pi mp/M} = \frac{1-e^{j2\pi mp}}{1-e^{j2\pi mp/M}} \quad . \tag{4-36}$$

If $p = 1, 2, \ldots, M-1$

$$S = \frac{1-1}{1-e^{j2\pi mp/M}} = 0 \quad . \tag{4-37}$$

If $p = 0$, we substitute $p = 0$ in the original expression

$$S = \sum_{m=0}^{M-1} 1 = M \quad . \tag{4-38}$$

Therefore Eq. (4-31) becomes

$$Q_{pN+n'} = \begin{cases} \sqrt{M}\, h_{n'}, & p = 0 \\ 0 & p = 1,2,\ldots,M-1 \end{cases} \quad . \tag{4-39}$$

(II) $n' = \frac{N}{2},\ldots,N-1$

$$\begin{aligned} Q_{pN+n'} &= \sum_{m=0}^{M-1} \frac{e^{j\pi m/M}}{\sqrt{M}} [h_{n'} e^{-j2\pi m(n'-N/2)/MN}] \\ &\quad \cdot e^{j2\pi mn'/MN} e^{j2\pi mp/M} \\ &= \frac{1}{\sqrt{M}} h_{n'} \sum_{m=0}^{M-1} e^{j\pi m/M} e^{-j2\pi mn'/MN} e^{j\pi m/M} \\ &\quad \cdot e^{j2\pi mn'/MN} e^{j2\pi mp/M} \\ &= \frac{1}{\sqrt{M}} h_{n'} \sum_{m=0}^{M-1} e^{j2\pi m(1+p)/M} \end{aligned} \tag{4-40}$$

$$= \begin{cases} \sqrt{M}\, h_{n'}, & p = M-1 \\ 0 & p = 0,1,\ldots,M-2 \end{cases} \quad .$$

Figure 4.8 shows the sequences Q_n and the reconstruction from the hologram. Figure 4.9 further shows the computer simulation of a two-dimensional case. Figure 4.9(a) is the original impulse response (letter 'P') and (b) is the reconstruction when the array is expanded by four times in each direction. Note that if the holograms are of the same size (before and after interpolation), then the impulse

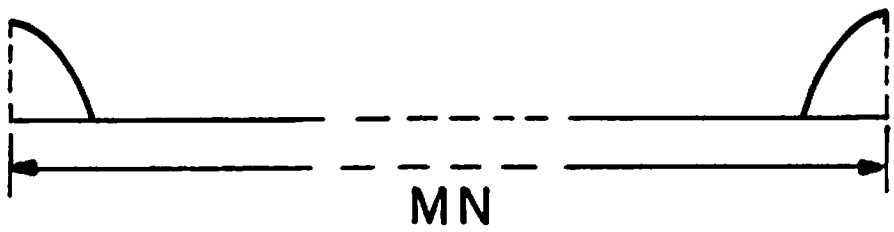

(a) output sequences Q_n, n=0,...,MN-1

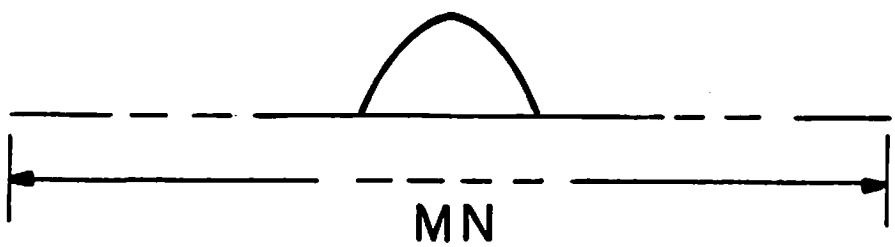

(b) reconstruction

Fig. 4.8 Results of DFT interpolation

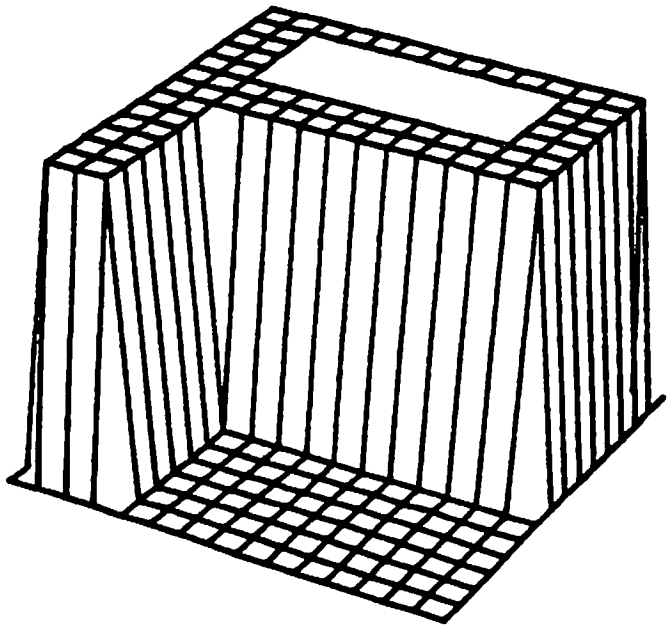

(a) impulse response (letter 'P')

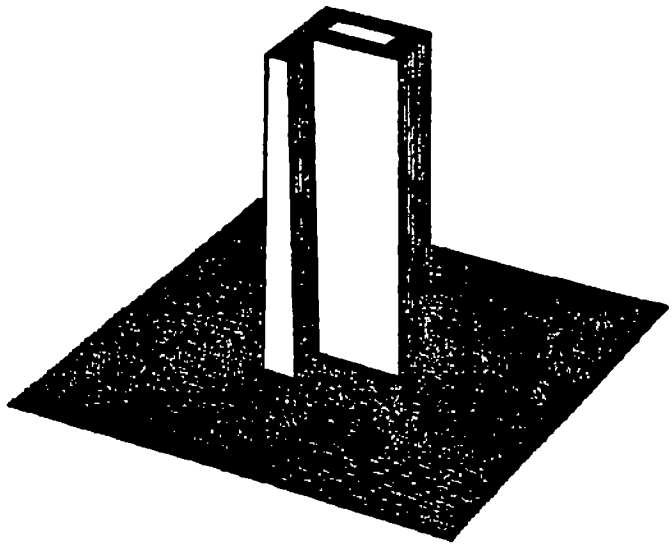

(b) reconstruction (M=4)

Fig. 4.9 Results of DFT interpolation (two-dimensional example)

response in (b) is of the same size as the impulse response in (a) except that in (b) it is surrounded by a zero array.

4.3.2 Relationship with sinc interpolation

Let us consider the following Fourier transform pair $h(x) \Leftrightarrow H(u)$ (Fig. 4.10) where $h(x)$ is space-limited (width X) and $H(u)$ is not band-limited although $|H(u)|$ may be very small when $|u|$ goes beyond a certain frequency. Suppose $h(x)$ is sampled at interval ΔX, then the aliasing error occurs due to the fact that no finite Nyquist rate exists. Figure 4.11 shows the sampled function $h(x)$ and its Fourier transform $H'(u)$. The period of $H'(u)$ is given by

$$F = \frac{1}{\Delta X} \tag{4-41}$$

and there are N samples in $h'(x)$.

When using the DFT, we have to sample $H'(u)$ for the same number of points. The interval is then given by

$$\Delta F = \frac{F}{N} = \frac{1}{N\Delta X} = \frac{1}{X} \quad . \tag{4-42}$$

Figure 4.12 shows the new transform pair $h''(x) \Leftrightarrow H''(u)$ and one period from each of them are what we actually get from the DFT.

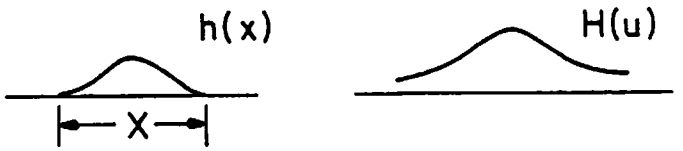

Fig. 4.10 Fourier transform pair h(x) <=> H(u)

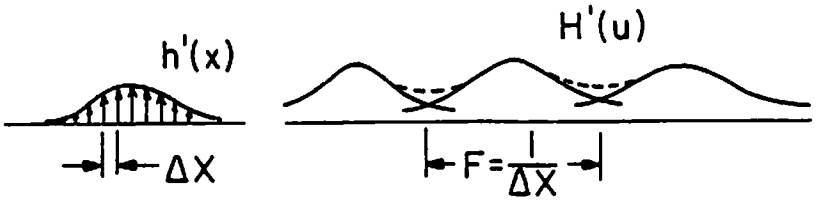

Fig. 4.11 Fourier transform pair h'(x) <=> H'(u) where h'(x) is the sampled version of h(x)

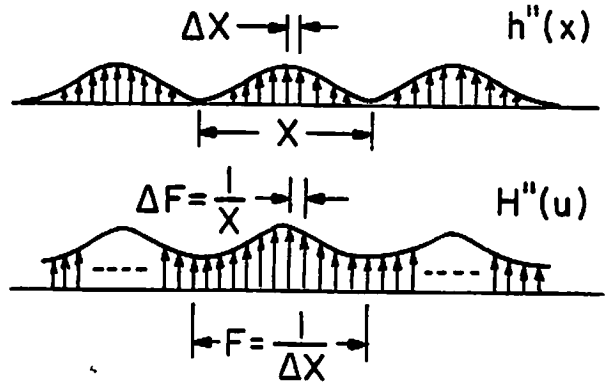

Fig. 4.12 Fourier transform pair h"(x) <=> H"(u) where both h(x) and H'(u) are sampled

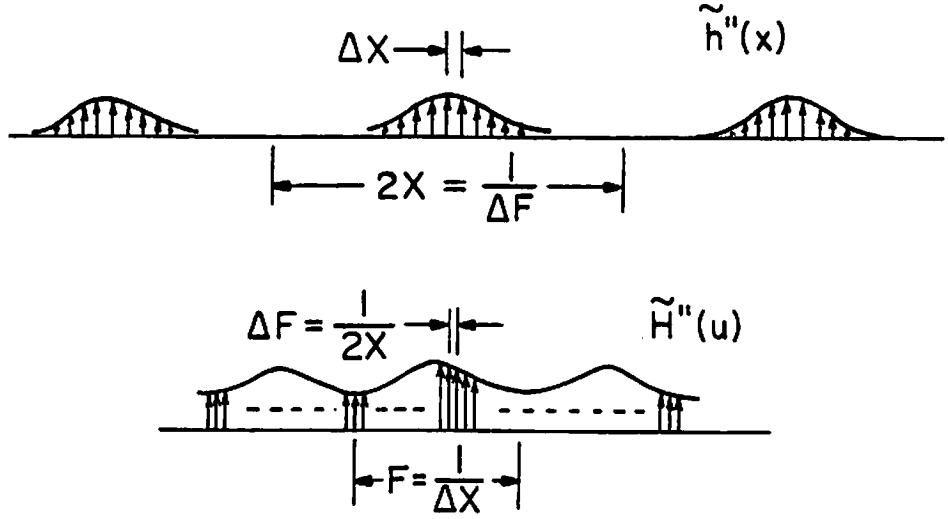

Fig. 4.13 Fourier transform pair h"(x) <=> H"(u) where H'(u) is sampled finer (M=2)

if we use a continuous sinc function interpolation for H"(u) then we are equivalently filtering h"(x) by a rect function giving the relationship in Fig. 4.11. Now if we sample H'(u) at the interval of $\frac{1}{Mx}$ instead of $\frac{1}{x}$, then we get a new transform pair $\tilde{h}$"(x) <=> $\tilde{H}$"(u) as shown in Fig. 4.13. All of the MN points are the result of the sinc interpolation since they are the sampled values of the continuous sinc interpolation. Notice that $\tilde{h}$"(x) is the sampled h(x) embedded in a zero array of size MN. This is exactly the same result obtained from the method we proposed in Section 4.3.1. Since the Fourier transform uniquely determines the relationship between the impulse response and the Fourier transform we can conclude that this method actually does the sinc function interpolation on a finite array of points. It is also noted that by embedding the object in a zero array and performing Fourier transform we also perform the sinc interpolation. However, it requires more core as working space as discussed in the next section.

4.3.3 Comparisons

To illustrate the advantage of this interpolation method let us consider the case when an array is passed n times through the space-transform iterative phase coding method discussed in Chapter 2. The original array size is

N x N and is to be put into a MN x MN zero array. Here we assume that M and N are power of 2.

When we use $(MN)^2$ points directly we need CPU time to do the Fourier transform (t_1) and the conversion between polar coordinate and Cartesian coordinates (t_1'). t_1 is given by [4-10]

$$t_1 = (2n-1)[(MN)^2 \log_2 (MN)^2] t_C$$
$$= 2(2n-1)M^2N^2[\log_2 (MN)]t_C \qquad (4\text{-}43)$$

where the factor of two in 2n accounts for the two Fourier transforms required in each iteration and -1 accounts for the fact that we need only one Fourier transform in the first iteration. Here t_C is the CPU time to perform one multiplication.

To compute t_1', let us assume that t_{PC} and t_{CP} are the times required for one component to do conversion from polar coordinate to Cartesian coordinates and vice versa. Also assume that the original object is in polar form.

Then

$$t_1' = (2n-1)(MN)^2(t_{PC}+t_{CP})$$
$$= (2n-1)M^2N^2t_0 \qquad (4\text{-}44)$$

where

$$t_0 = t_{PC}+t_{CP} \quad . \tag{4-45}$$

When using the interpolation method we need CPU time for the iterative method (t_{21}), interpolation (t_{22}) and conversion (t_2'). t_{21} is given by

$$\begin{aligned} t_{21} &= (2n-1)N^2(\log_2 N^2)t_C \\ &= 2(2n-1)N^2(\log_2 N)t_C \quad . \end{aligned} \tag{4-46}$$

To interpolate the points between the original points we have to go through Eqs. (4-26)-(4-28). The multiplication of an exponential term is simply an addition in phase and can be neglected in obtaining

$$\begin{aligned} t_{22} &= (M^2-1)N^2(\log_2 N^2)t_C \\ &= (M^2-1)2N^2(\log_2 N)t_C \quad . \end{aligned} \tag{4-47}$$

Letting t_2 be the sum of t_{21} and t_{22}, we have

$$\begin{aligned} t_2 &= t_{21}+t_{22} \\ &= 2N^2(2n+M^2-2)\log_2 N \quad . \end{aligned} \tag{4-48}$$

The conversion time t_2' is given by

$$\begin{aligned} t_2' &= (2n-1)N^2t_0+(M^2-1)N^2t_0 \\ &= (2n+M^2-2)N^2t_0 \end{aligned} \tag{4-49}$$

where the first term accounts for the conversion performed in the iterative method and the second term for the

interpolation. The -1 in (M^2-1) is due to the fact that we need not compute the transform resulted from multiplying zero phase. Let us consider some typical values of M, N, and n to compare these two methods. Suppose n = 20, N = 32, M = 4, then

$$t_1 = 2N^2 \cdot 39 \cdot 16 \cdot 7t_c = 2N^2 \cdot 4368t_c \tag{4-50}$$

$$t_2 = 2N^2(40+16-2) \cdot 5t_c = 2N^2 \cdot 270t_c \tag{4-51}$$

$$\frac{t_1}{t_2} = \frac{4368}{270} \approx 16.2 \tag{4-52}$$

and the saving of the CPU time for the non-conversion part is approximately a factor of 16.2. For the conversion part we have

$$t_1' = 39 \cdot 16N^2t_0 = 624N^2t_0 \tag{4-53}$$

$$t_2' = (40+16-2)N^2t_0 = 54N^2t_0 \tag{4-54}$$

then we have

$$\frac{t_1'}{t_2'} = \frac{624}{54} \approx 11.6 \tag{4-55}$$

and the saving in data conversion is approximately a factor of 11.6.

For other larger values of n, M and N we can use the approximations

$$t_1 \simeq 4nM^2N^2(\log_2 N)t_C \tag{4-56}$$

$$t_2 \simeq 2N^2(2n+M^2)(\log_2 N)t_C \tag{4-57}$$

$$t_1' \simeq 2nM^2N^2t_0 \tag{4-58}$$

$$t_2' \simeq (2n+M^2)N^2t_0 \tag{4-59}$$

$$\frac{t_1}{t_2} \simeq \frac{t_1'}{t_2'} \simeq \frac{2nM^2}{2n+M^2} \tag{4-60}$$

It is obvious from Eq. (4-60) that the interpolation method always takes less CPU time for larger n and M.

Another way to save CPU time in making the hologram mentioned above is to perform the iterative phase coding method on N^2 points, embed this result in a $(MN)^2$ zero array and perform the Fourier transform. Letting t_3 and t_3' be the CPU time required for Fourier transforming and data conversion respectively, we have

$$\begin{aligned} t_3 &= (2n-1)N^2[\log_2 N^2]t_C+(MN)^2[\log_2(MN)^2]t_C \\ &= 2(2n-1)N^2[\log_2 N]t_C+2M^2N^2[\log_2(MN)]t_C \quad . \end{aligned} \tag{4-61}$$

Compared with t_2 in Eq. (4-46), t_3 is larger but approximately equal to t_2. The conversion time t_3 is given

by

$$t_3' = (2n-1)N^2 t_0 + (MN)^2 t_{CP} \quad . \qquad (4-62)$$

Although t' is smaller than t', this method requires a large amount of core or a great deal of disk swapping to do the computation when M is large.

4.3.4 Experimental results

As in Section 4.2.3 we again demonstrate the hologram interpolation method by using a kinoform. The interpolation is done according to Eqs. (4-26)-(4-28) in terms of complex values. Then we discard the amplitude information and make a kinoform on Kodachrome 64 by the ROACH method. Figure 4.14 is the reconstruction of the letter 'P' from the original hologram. Figure 4.15 shows the reconstruction from the interpolated hologram with M = 2. The spacing between different orders is doubled and no false images appear in between.

4.3.5 Conclusions

We have introduced a method to perform interpolation which utilizes the translation property of the Fourier transform. This method has reduced the amount of CPU time and core size in making a computer-generated hologram which reconstructs an impulse response embedded in a large zero

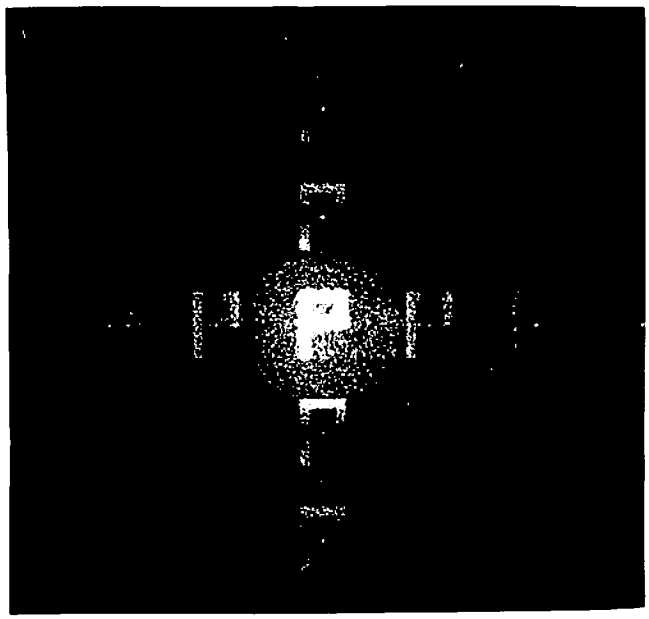

Fig. 4.14 Reconstruction from kinoform

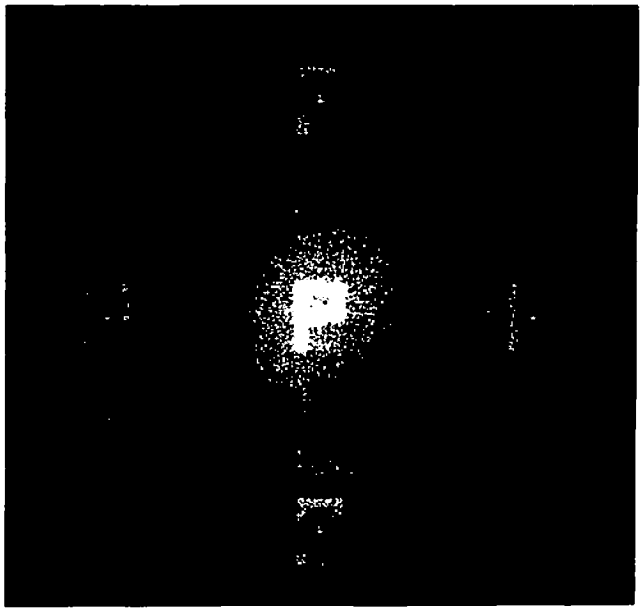

Fig. 4.15 Reconstruction from interpolated kinoform (M=2)

array. We also showed that this method is a practical implementation of sinc function interpolation without any error caused by the truncation of the impulse response assuming function is periodic. This method of performing sinc interpolation may find other applications in other areas.

When the hologram is used in a filtering system with a large input object format, M is usually very large (for example M = 10) and the space-bandwidth product requirements on the plotter and recording material are increased. In the next chapter we will introduce a method of making a continuous hologram which reconstructs a single impulse response only and does not require a large space-bandwidth product for the plotter.

CHAPTER 5

COMPUTER-GENERATED CONTINUOUS HOLOGRAMS

On-axis holograms such as the ROACH [5-1] and kinoform [5-2] have the advantage of high diffraction efficiency. However, the impulse response appears not only at the zero order but also at higher orders. These higher orders are strongly attenuated by a sinc function as the result of the finite cell size of the hologram. However the orders adjacent to the zero order still have non-negligible energy. If the hologram is to be used in a filtering system, the presence of these high orders limits the size of the input object to be filtered.

In Chapter 4 we have discussed two methods, the cell size expansion method and hologram interpolation with the DFT, which either suppress the high orders or separate them further. Although these methods relax the constraint on the input object size, the problem of higher orders still exists. In this chapter we further describe a way of making a continuous hologram from sampled patterns. This continuous hologram will produce the zero order only and eliminate the problems associated with the high orders.

5.1 Basic concept of continuous holograms

Figure 5.1 shows the set-up for making continuous holograms. Let us consider one path first. If we put a sampled ROACH at the plane of the amplitude pattern then due to the use of the low-pass filter we will get a wavefront corresponding to a continuous ROACH at the plane of color film. Unfortunately, the film is sensitive to intensity rather than to amplitude and phase respectively. Therefore this wavefront cannot be recorded directly. Instead of recording the information by interference methods [5-3,5-4,5-5] we can manipulate the amplitude and phase parts separately and record them on the color film (specifically Kodachrome 64) using the ROACH method.

For example in the upper path of Fig. 5.1,we have an amplitude pattern to control the amplitude transmittance on the film. Upon illumination by red light (through the red filter) this pattern produces a Fourier transform in the low-pass filter plane. The Fourier transform has multiple orders due to the fact that the pattern is sampled. Only the zero order is transmitted through the low-pass filter and a continuous image is formed in the film plane.

The amplitude of the samples on the pattern and the exposure of the film are predetermined by other test

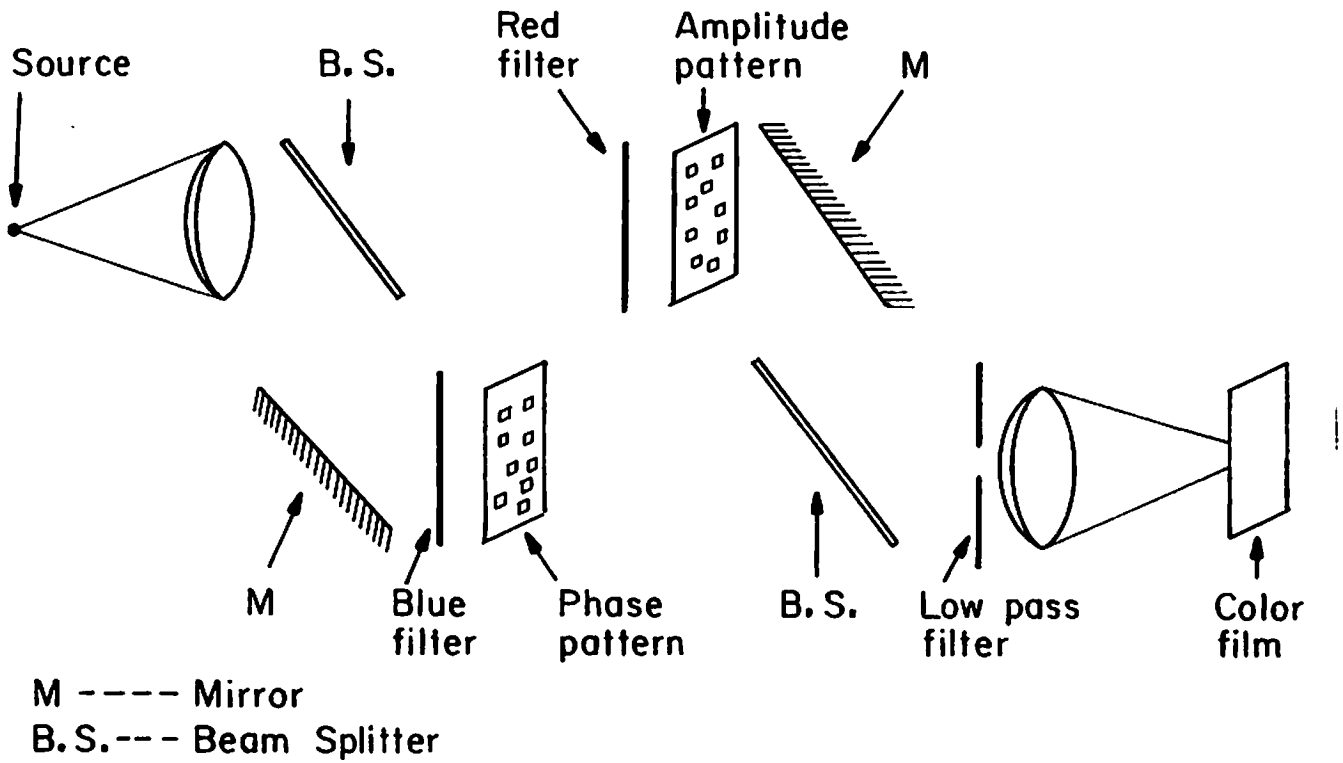

Fig. 5.1 Set-up for making continuous holograms

patterns (as will be discussed in Section 5.2) so that the desired transmittance is obtained on the film. Similarly in the lower path we have a sampled phase control pattern illuminated by blue-green light (through the color filter) that forms a continuous image on the color film. Again the amplitude of the samples and the exposure time are predetermined so that the desired phase shift is obtained on the developed color film. The continuous hologram thus made will produce a single impulse response when illuminated by red light.

The samples on the amplitude and phase patterns can be either grey tone or half tone (binary). The binary patterns are much easier to control and were chosen in our experiments. Since amplitude and phase are controlled by two different paths, it is essential to have these two patterns aligned. It has been found in the experiment that two pairs of cross hairs plotted on opposite corners of the patterns are sufficient for accurate alignment.

The same set-up can be used for making amplitude only holograms and phase only holograms (kinoforms). For an amplitude only hologram we use the upper path only while for a kinoform we use the lower path for phase information control and then reexpose the film with uniform red light. In the following experimental work we use color reversal

films (specifically Kodachrome 64) for all continuous holograms although the amplitude only and phase only holograms can be made on other materials. For example we can make a kinoforms by exposing a phase pattern on 649F then bleaching it.

5.2 Calibration procedure

Suppose the sampled pattern for amplitude control or phase control is an array of δ functions of different amplitudes. After the low-pass filtering we have the convolution of these δ functions with the sinc function at the film plane. Therefore the exposures at the sampling points are the same as though there were no low-pass filtering. By using the proper exposure, we can obtain the desired amplitude transmittance and phase shift at the sampling points. Between the sampling points are the interpolated values. In order to determine the proper exposure time, we have to measure the amplitude transmittance or phase shift at the sampling points. However there is no way to measure these quantities at one point. Therefore during the calibration step we construct a pattern with constant amplitude δ functions over a certain area. The corresponding area in the image plane will have an approximately constant exposure and therefore can be measured in terms of the transmittance or phase

shift. In practice, we do not have δ functions in the sampled patterns. Instead, finite width pulses are used. These can be precompensated by the generalized sampling theorem [5-6] so that the effective results are δ functions.

5.2.1 Amplitude calibration

Figure 5.2 shows a typical amplitude test pattern. It contains 16 constant amplitude blocks. Each block has $(32)^2$ cells with $(16)^2$ quantization levels each. The arrangement of the value in each block is made so that adjacent blocks are easy to distinguish. Since there are only 16 blocks available, we assign 16 linearly spaced values between 0 and 256 to each block. In each cell the aperture is at the center and is plotted as close to a square as possible. These patterns are made on SO-115 (Fig. 5.3) using a Dicomed Image Recorder and then photoreduced onto Kodak HRP in exactly the same way as the DPH's that were made and discussed in Chapter 3. These test patterns are put into the set-up shown in Fig. 5.1 and films are exposed to these patterns through a red filter (Kodak Wratten filter 25). On the film, the area corresponding to each block has a nearly constant density at least at the central portion since the contributions from the points outside that area are from the tail of the

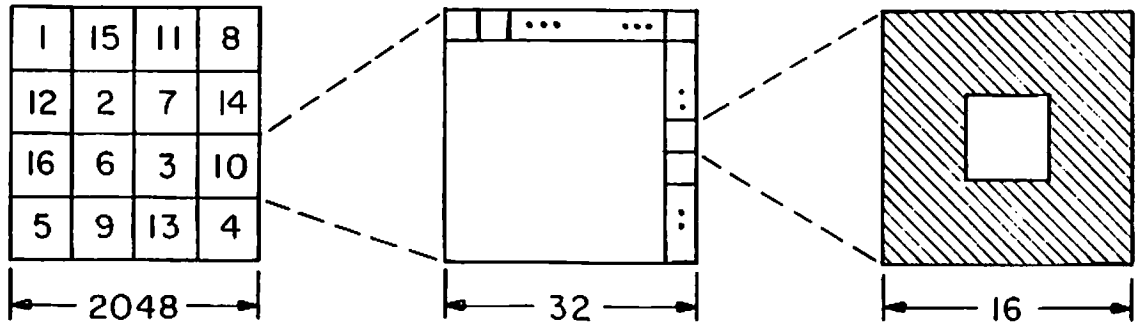

Fig. 5.2 Values of an amplitude test pattern

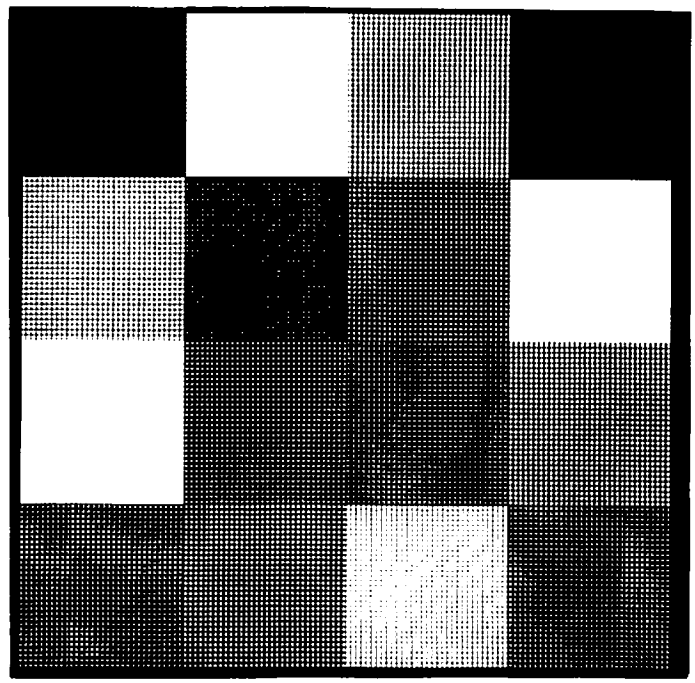

Fig. 5.3 Amplitude test pattern

sinc function and can be neglected. The density is then measured using a Macbeth densitometer at the center of each block. The result not only depends on the aperture size but also on the exposure time. After using several different exposures we can choose the proper one which gives a reasonable linear region in the t-E or D-log E curve, where E represents the aperture size.

In general the linear region available in these curves (for example the t-E curve) has a very limited dynamic range. The effects of this finite dynamic range and finite quantization levels have been evaluated by computer simulation. The results indicate that the number of quantization levels we used (around 100) is sufficient. However while the limited dynamic range of the transmittance works fine for phase coded impulse responses, it introduces severe distortion for the zero phase impulse response since the Fourier transform contains many small components which are not correctly represented under the limited dynamic range. Therefore we have to use nonlinear characteristic curves. To simplify the computation, the nonlinear curve we use is a piecewise linear curve. Figure 5.4 shows an idealized piecewise linear t-E curve. t_3, t_2, t_1 in Fig. 5.4 represent those end points of the piecewise linear curve and E_3, E_2 and E_1 are the corresponding exposures (the size of the apertures on the

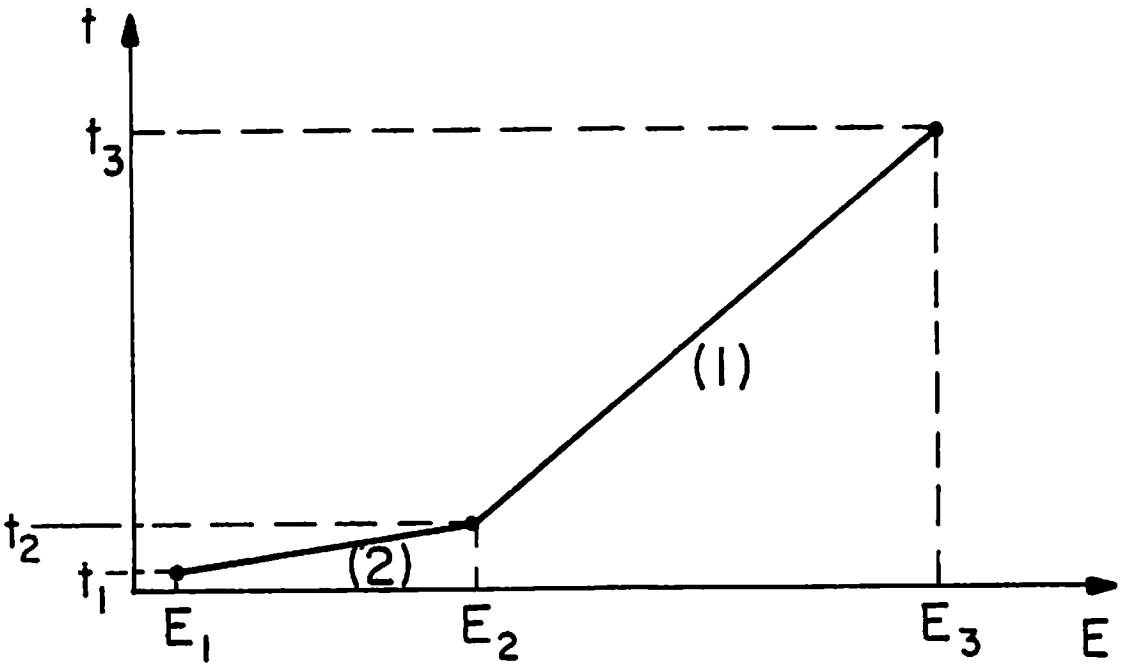

Fig. 5.4 Piecewise linear t-E curve

binary pattern). Due to the use of these subscripts, the formula derived in the following can be used for negative film too.

In practice $t_3 < 1$ and therefore we normalize the amplitude transmittance by t_3 and let

$$t_a = \frac{t}{t_3} \quad . \tag{5-1}$$

The curve can be formulated as

$$\begin{aligned} E &= \frac{E_3-E_2}{t_3-t_2}(t-t_2)+E_2 \qquad \text{if } t_2 \leq t \leq t_3 \\ E &= \frac{E_2-E_1}{t_2-t_1}(t-t_1)+E_1 \qquad \text{if } t_1 \leq t \leq t_2 \quad . \end{aligned} \tag{5-2}$$

If $Ae^{j\theta}$ is the transform to be recorded then A must be normalized according to

$$A_N = \frac{A}{A_{max}} \tag{5-3}$$

where A_{max} is the maximum value of A. Equalizing t_a and A_N and using Eq. (5-1) we can rewrite Eq. (5-2) as

$$E = \begin{cases} \dfrac{E_3-E_2}{t_3-t_2}(t_3A_N-t_2)+E_2 & \text{if } A_N \geq \dfrac{t_2}{t_3} \\ \dfrac{E_2-E_1}{t_2-t_1}(t_3A_N-t_1)+E_1 & \text{if } \dfrac{t_2}{t_3} > A_N \geq \dfrac{t_1}{t_3} \\ E_1 & \text{if } A_N < \dfrac{t_1}{t_3} \quad . \end{cases} \tag{5-4}$$

For $A_N < \frac{t_1}{t_3}$ we assign E to be E_1 since $\frac{t_1}{t_3}$ is the minimum

transmittance value achievable by the piecewise linear curve. After these exposures (aperture sizes) are determined, a binary pattern corresponding to these values is made and put into the system shown in Fig. 5.1 to make the amplitude part of the hologram. A similar procedure can be applied to the piecewise linear D-logE curve and is not repeated here. We can further reduce the distortion due to the small components by truncating those few large components in the low frequency region. In general the truncation of these low frequency components does not affect the appearance of the reconstruction much. Furthermore since the Fourier transform of zero phase impulse response has a lot of small components, the truncation of the large components allows those small components to be represented by higher transmittance functions and therefore increases the efficiency of the hologram.

5.2.2 Phase calibration

To test the phase shift, we divide each block in Fig. 5.2 into 4 sub-blocks and interlace the original values by some reference value (say 0). The phase test pattern as shown in Fig. 5.5 is put into the set-up in Fig. 5.1 and illuminated by blue-green light (through Kodak Wratten filter 38A). The color film thus exposed is then flooded

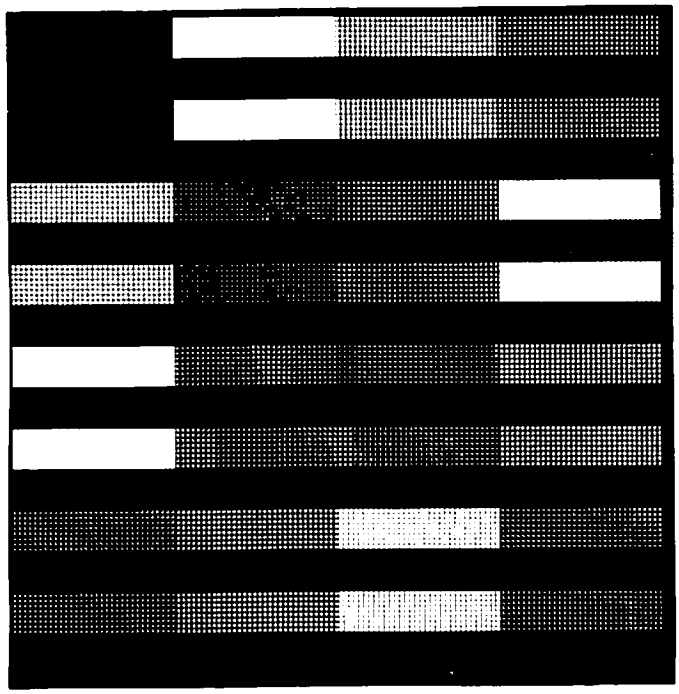

Fig. 5.5 Phase test pattern

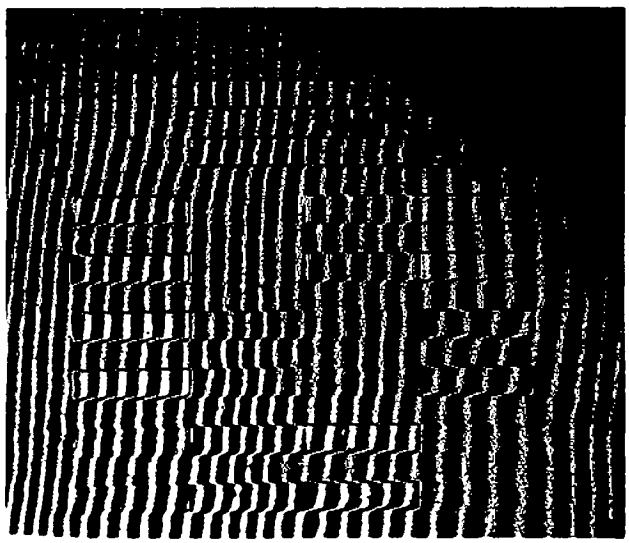

Fig. 5.6 Interference pattern

with red light. Ideally the developed film is transparent to red light but phase variation occurs due to the emulsion thickness and refractive index change in the blue absorbing (yellow) and green absorbing (magenta) layers. The amount of phase shift can be measured by using a Mach-Zehnder interferometer. Figure 5.6 shows the interference pattern obtained from the interferometer. The spacing between two fringes corresponds to a phase shift of 2π and the phase shift can be determined by measuring the amount of fringe shift with respect to the spacing between the fringes. We can choose a linear portion of θ-E or θ-logE curves to compute the proper exposure. Fig. 5.7 shows an idealized θ-E curve with

$$\theta_2 - \theta_1 = 2\pi \quad . \tag{5-5}$$

The proper exposure (or aperture size) for a given phase θ is given by

$$E = \frac{E_2 - E_1}{2\pi}\,\theta + E_1 \quad . \tag{5-6}$$

A binary pattern corresponding to these values is made and used as a phase control pattern in the set-up of Fig. 5.1. In the case of using a θ-logE curve , a similar procedure is applied and is not repeated here. A typical pattern is shown in Fig. 5.8. The aperture size and exposure time determine the amount of light going through each aperture.

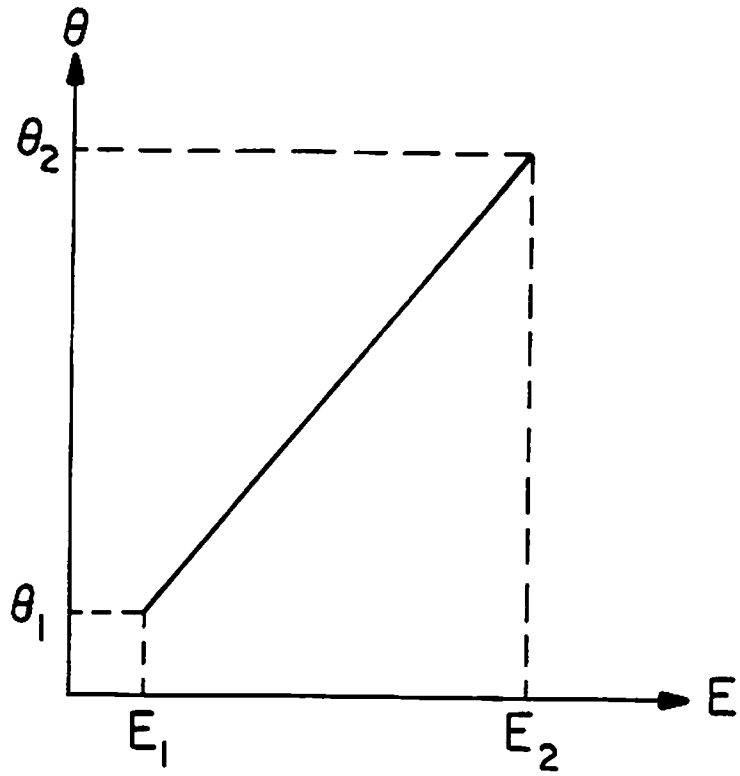

Fig. 5.7 Linear θ-E curve

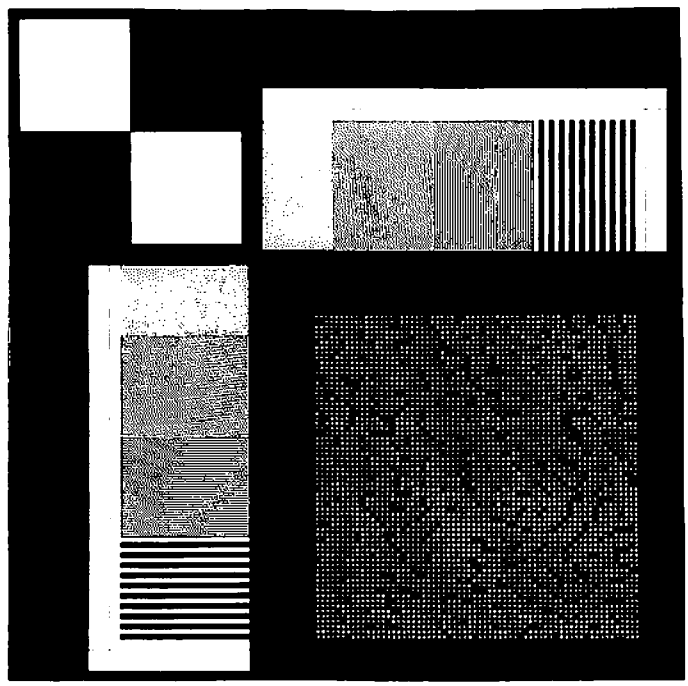

Fig. 5.8 A binary pattern for making continuous hologram

The gratings besides the pattern are for alignment purposes. The Moiré produced by these gratings can be used for fine position adjustment. However we have found that the two cross hairs beside the gratings are sufficient for accurate alignment. The binary squares at the top left can be used to determine how good the binary pattern is (in terms of the binary transmittance values and the sharpness of the aperture contour).

5.3 Some practical considerations

5.3.1 Sampling rate

Let $Ae^{j\theta}$ be the Fourier transform of the impulse response and assume it is sampled at a rate not less than the Nyquist rate. Therefore different orders of the reconstruction, or $\mathfrak{F}^{-1}\{Ae^{j\theta}\}$, do not overlap. Since

$$\mathfrak{F}^{-1}\{Ae^{j\theta}\}=\mathfrak{F}^{-1}\{A\} * \mathfrak{F}^{-1}\{e^{j\theta}\} \qquad (5\text{-}7)$$

the bandwidth of $Ae^{j\theta}$ (i.e., width of $\mathfrak{F}^{-1}\{Ae^{j\theta}\}$) is the sum of the bandwidths of A and $e^{j\theta}$. Therefore the bandwidth of A or $e^{j\theta}$ is smaller than the bandwidth of $Ae^{j\theta}$ and the same sampling rate for $Ae^{j\theta}$ can be used for both A and $e^{j\theta}$ without introducing aliasing error. That is, given an array of samples of $Ae^{j\theta}$, the amplitude and phase parts of this array A and $e^{j\theta}$ can be used directly in making binary patterns for continuous hologram.

However the patterns we actually use may not be proportional to A or $e^{j\theta}$ depending on the characteristic functions we use. For the amplitude part we have used a piecewise linear t-E curve. For simplicity we assume that the curve is linear and we make the pattern according to the first part of Eq. (5-4). Then the function E has the same bandwidth as A and the original sampling rate is sufficient.

For the phase part, we are using the linear θ-E curve and Eq. (5-6) is used to make the phase pattern. The exposure E (or the aperture size) has the same bandwidth as θ. However $e^{j\theta}$ can be expanded as

$$e^{j\theta} \approx 1 + j\theta - \frac{1}{2}\theta^2 - j\frac{1}{6}\theta^3 + \ldots \qquad (5\text{-}8)$$

therefore θ has smaller bandwidth than $e^{j\theta}$ and so does E. Again we have shown that the original sampling rate is also sufficient for the phase pattern.

When the impulse response is well diffused, A(u,v) is nearly flat and $\mathcal{F}^{-1}\{A(u,v)\}$ approaches a δ function. Equivalently we can say that A(u,v) has a fairly small bandwidth. In this case we can sample the amplitude pattern coarser than the phase pattern. By doing this we have more quantization levels for each sample and therefore increase the dynamic range. However in the filter plane

the different orders corresponding to the amplitude pattern will become closer. If the same low-pass filter is used for both amplitude and phase patterns then higher orders of the amplitude pattern will go through if the phase pattern is to be properly filtered. Therefore we have to adjust the filter size for amplitude and phase exposures unless a special color filter is used which passes red light in a smaller low-pass area and passes blue and green light in a larger low-pass area.

5.3.2 Scaling effect due to different colors

In the set-up of Fig. 5.1 let d_0 denote the distance between the binary pattern and the second lens and d_i the image distance. Then it can be shown that without the presence of the low-pass filter, if the input pattern is $E(x,y)$ then the output is $E(-\frac{x}{M},-\frac{y}{M})$ where $M = d_i/d_0$ is the magnification factor. We see that there is no wavelength factor in this result. Therefore as long as the object distance d_0 is the same for both the amplitude pattern and phase pattern, no scaling problem occurs.

However in the filter plane the scale of the transform does change with color. In Section 5.3.1 we have shown that the transforms from the amplitude and phase patterns have a size less than the original array size. Let us assume the worst case that both of them are equal to the

original array size. Due to the sampled nature of the pattern the transform is repeated in both directions. For simplicity, Fig. 5.9 shows the repetition in one direction only and does not show the attenuation effects due to the finite sample size either. This figure clearly shows the overlap of different orders resulting from red and blue light. If a low-pass filter is to pass all the zero order in red then some portion of the high order in blue also goes through. On the other hand, if the filter is to pass the zero order in blue only,then some portion of the zero order in red is discarded. Therefore we can either use different size low-pass filters or use a color filter similar to the one described in Section 5.3.1 when the amplitude pattern is to be sampled on a coarser scale. However these methods are more cumbersome and we prefer to use one size of low-pass filter. This can be achieved by limiting the size of the impulse response in the original array so that the zero order in red will not overlap with the high orders in blue.

Suppose that the extreme wavelengths we use are λ_R(632.8 nm) and λ_B(457.9 nm) and the size of one order in λ_R is D_R in the filter plane with the impulse response constrained to CD_R ($C < 1$). Then the corresponding sizes in λ_B are $\frac{\lambda_B}{\lambda_R}D_R$ and $C\frac{\lambda_B}{\lambda_R}D_R$. These dimensions are shown in Fig. 5.10. It is obvious that $C = \lambda_B/\lambda_R$ can be used.

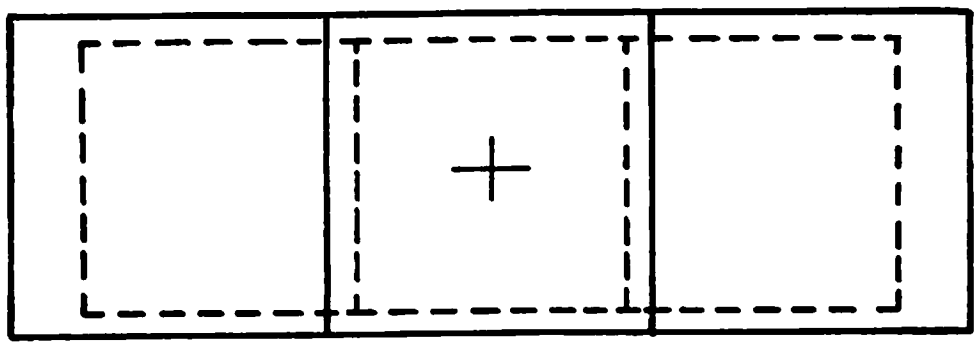

Fig. 5.9 Overlap of different orders in the transform plane due to different colors. "+" denotes the optical axis. Large squares indicate the transform in red, and small squares in blue

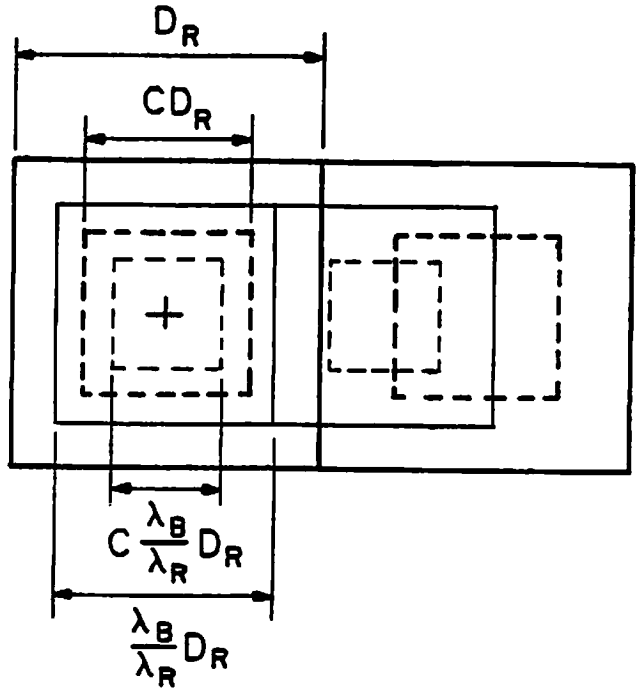

Fig. 5.10 Dimension of different orders with constrained impulse response

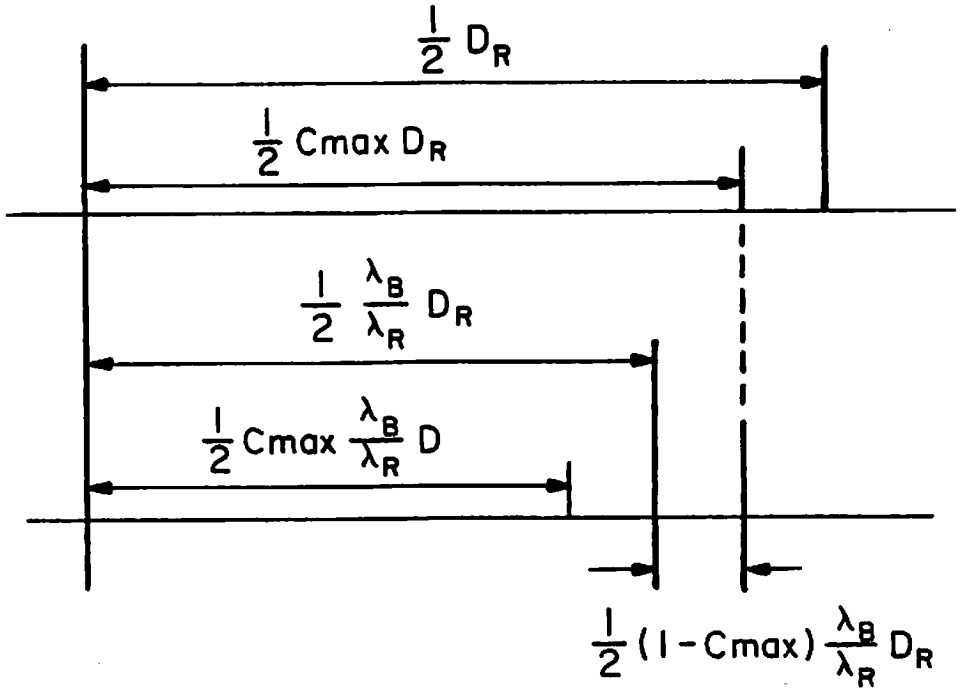

Fig. 5.11 Condition for C_{max}

However we want to find the maximum value of C, C_{max}, such that no overlapping occurs. As illustrated in Fig. 5.11, C_{max} can be obtained if

$$\frac{1}{2}C_{max}D_R = \frac{1}{2}\frac{\lambda_B}{\lambda_R}D_R+\frac{1}{2}\frac{\lambda_B}{\lambda_R}(1-C_{max})D_R. \qquad (5\text{-}9)$$

Therefore we have

$$C_{max} = \frac{2\lambda_B}{\lambda_B+\lambda_R}, \qquad (5\text{-}10)$$

For $\lambda_B = 457.9$ nm $\lambda_R = 632.8$ nm we have $C_{max} \simeq 0.83$. This is bigger than the intuitive estimation of $C = \frac{\lambda_B}{\lambda_R} \simeq 0.72$. Therefore we must constrain the size of the impulse response to less or equal to 83% of the array in each direction. The filter can always have a width of $C_{max}D_R$ no matter what value of C is actually used as long as $C \leq Cmax$.

In practice if the impulse response is diffused then the transform from the amplitude pattern is close to a δ function and it never overlaps with the higher orders from the phase pattern. We can therefore use the whole array for the impulse response and use a phase filter pattern corresponding to the size $\frac{\lambda_B}{\lambda_R}D_R$ of the zero order,

5.3.3 Cross talk and its compensation

To make a continuous ROACH with the correct amplitude transmittance function and phase variation, we have to consider the cross talk between amplitude and phase. The cross talk occurs in two ways. First of all we can not expose one layer without affecting the other layer. Furthermore, each layer after development may affect both amplitude transmittance and phase shift instead of just having one effect. These effects are called exposure cross talk and dye layer cross talk respectively. From a practical point of view all we need to know are how the amplitude controlling exposure affects the phase shift and how the phase controlling exposure affects the amplitude transmittance instead of the details of how these cross talk effects arise. The result of the sampled ROACH [5-1] indicated that the phase-to-amplitude cross talk can be neglected while the amplitude-to-phase cross talk has to be compensated for. In fact the amplitude-to-phase cross talk is primarily due to dye layer cross talk.

To compensate for the phase shift effect due to the amplitude exposure, we have to determine the relationship between amplitude exposure and the phase shift. In principle we can make a phase pattern like Fig. 5.5 in red and use the Mach-Zehnder interferometer to measure the

phase shift. However since not much light goes through the low transmittance areas the fringes are hard to visualize and measurement of the phase shift is impossible. To solve this problem we can flood the film with green light in addition to the phase pattern exposure in red and then use the Mach-Zehnder interferometer operated under green light to measure the phase shift. The phase shift obtained is in terms of green light and has to be converted to the value in red. To simplify the analysis, we assume that there is only one layer on the film as shown in Fig. 5.12. The single layer has a thickness of d_1 with an index of refraction n_1. After exposure by a certain level of light E and processing, the thickness is reduced to d_1-d with an index of refraction n_2 (in general $n_2 < n_1$). When the film is illuminated by a plane wave the transmitted wave in the unexposed region has the phase θ_1

$$\theta_1 = -kn_1d_1 \tag{5-11}$$

where $k = 2\pi/\lambda$ is the wave number. Meanwhile the phase in the exposed region is given by

$$\theta_2 = -[kn_2(d_1-d)+kd]. \tag{5-12}$$

Using θ_1 as a reference we have

$$\begin{aligned} \theta &= \theta_2-\theta_1 \\ &= k[(n_1-n_2)d_1+(n_2-1)d] \quad . \end{aligned} \tag{5-13}$$

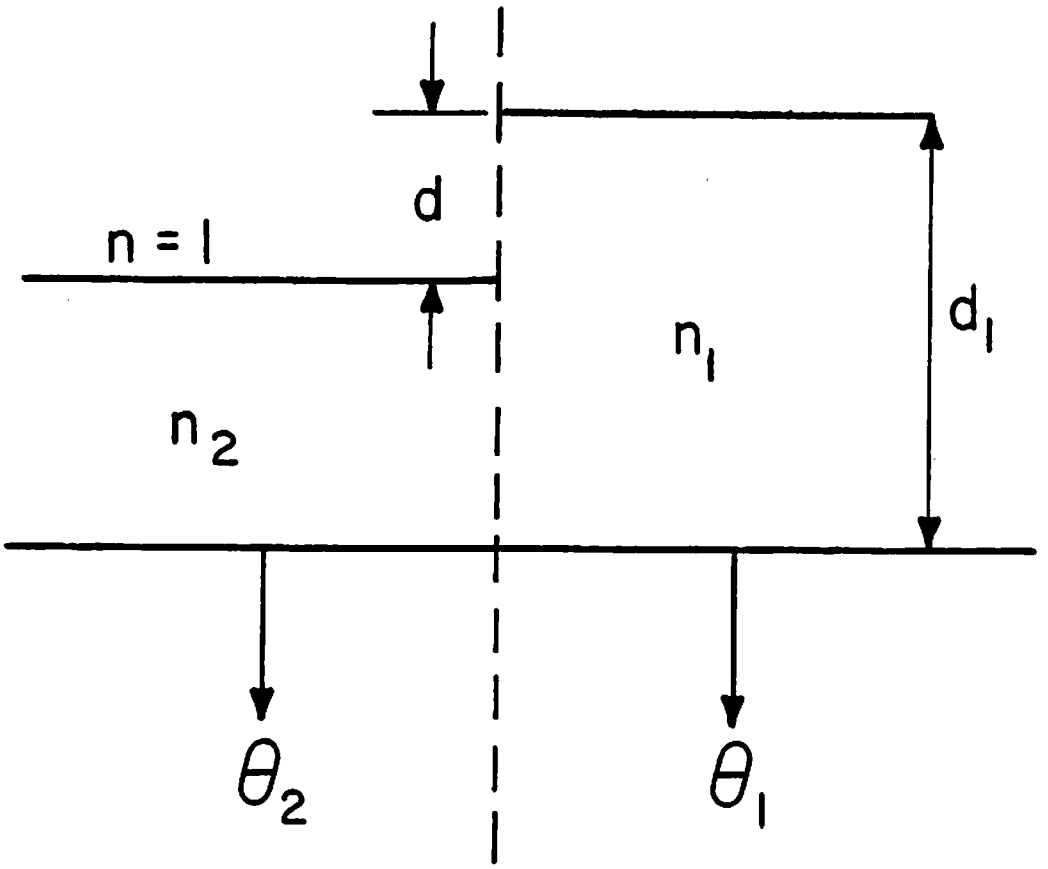

Fig. 5.12 One layer model of film for computing phase shift

Since $n_1 \geq n_2 \geq 1$ we have $\theta \geq 0$. The first term is the result of index change and is commonly called the index image. The second term is the result of the thickness change and is called the relief image. It is known that most of the phase change is the result of the relief image. This can be shown by using a liquid gate which eliminates the effect of the relief image.

The wave number $k = 2\pi/\lambda$ and n_1, n_2 are functions of λ and therefore θ would be different for different colors. Here we consider red light and green light and use subscripts R and G to indicate different quantities. Therefore Eq. (5-13) becomes

$$\theta_R = \frac{2\pi}{\lambda_R} [(n_{1R}-n_{2R})d_1+(n_{2R}-1)d] \qquad (5\text{-}14)$$

and

$$\theta_G = \frac{2\pi}{\lambda_G} [(n_{1G}-n_{2G})d_1+(n_{2G}-1)d] \quad . \qquad (5\text{-}15)$$

Suppose n_{1R}, n_{2R}, n_{1G}, n_{2G} and d_1 are known. Then after obtaining θ_G from the experiment we can obtain d from Eq. (5-15) and then θ_R from Eq. (5-14). Unfortunately, those parameters are not known. Even though these values can be measured by other methods, the indices of refraction n_{2R} and n_{2G} are functions of exposure level E and it is impractical to obtain indices of refraction for different

values of E.

One approximation of θ_R can be obtained by considering the ratio $\frac{\theta_R}{\theta_G}$

$$\frac{\theta_R}{\theta_G} = \frac{\lambda_G}{\lambda_R} \frac{[(n_{1R}-n_{2R})d_1+(n_{2R}-1)d]}{[(n_{1G}-n_{2G})d_1+(n_{2G}-1)d]} \simeq \frac{\lambda_G}{\lambda_R} \frac{(n_{2R}-1)}{(n_{2G}-1)} \quad . \tag{5-16}$$

This approximation is the result of the observation that the index image can be neglected when compared with the relief image. When substituting λ_G = 514.5 nm, λ_R = 632.8 nm, n_{2R} = 1.525 and n_{2G} = 1.531 [5-7], Eq. (5-16) becomes

$$\frac{\theta_R}{\theta_G} \simeq \frac{514.5}{632.8} \frac{0.525}{0.531} \simeq \frac{\lambda_G}{\lambda_R} \quad . \tag{5-17}$$

The wavelength factor apparently dominates and we obtain the simple relation in Eq. (5-17).

A more complete model assumes three layers with each of them similar to the one shown in Fig. 5.12. Then instead of Eq. (5-13) we have

$$\theta = k \sum_{i=1}^{3} [(n_1^{(i)}-n_2^{(i)})d_1^{(i)}+(n_2^{(i)}-1)d^{(i)}] \tag{5-18}$$

where the superscripts indicate different layers. However due to the fact that the exposure cross talk is negligible

the one layer model in Fig. 5.12 is sufficient. Therefore when the phase shift in green θ_G is obtained we can get θ_R by

$$\theta_R = \theta_G \frac{\lambda_G}{\lambda_R} \quad . \tag{5-19}$$

The phase thus determined has similar characteristics as the phase variation in the phase controlling layer as described in Section 5.2.2. To compensate for the phase shift in the amplitude layer, Eq. (5-6) is modified as

$$E = \frac{E_2 - E_1}{2\pi} (\theta - \theta_R)_{\text{Mod}2\pi} + E_1 \tag{5-20}$$

where θ_R is the phase shift resulting from the amplitude exposure.

Although the exposure cross talk can be neglected in general, it can be reduced if desired. Instead of using white light in the set-up of Fig. 5.1, we can use laser sources to expose the film. For example a He-Ne laser (632.8 nm) can be used for amplitude control and an Argon laser (514.5 nm) can be used for phase control. In order to avoid the coherent noise, moving diffusers should be used in this set-up. The dye layer cross talk, however, still exists and has to be precompensated as described above.

We can also eliminate all kinds of cross talk by using two separate films. One film contains only the amplitude information and the other contains only the phase information. Two films are aligned carefully with the aid of some reference marks and then fixed together permanently. The phase variation due to the thickness change on the amplitude controlling film can be eliminated by using the same gelatin as the emulsion to glue two films together as shown in Fig. 5.13.

Even though these improvements are possible, they involve more complicated processes to make the hologram. Experimental results (as will be shown in Section 5.5) show that the reconstructon is acceptable with only the precompensation of amplitude-to-phase cross talk described in this section.

5.4 Errors in the continuous holograms and computer simulations

In this section we analyze errors associated with continuous holograms either inherent or resulting from the production process. These errors are further illustrated by computer simulations.

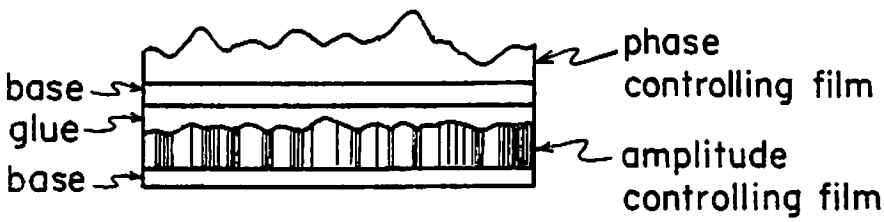

Fig. 5.13 ROACH making by two separate films

5.4.1 Interpolation error

To make a continuous hologram, we can low-pass filter the sampled hologram and get a continuous wavefront which is the sinc interpolation of the sampled one. Unfortunately even if we do get this continuous wavefront, there is no way to record the complex information except by an interference method. Therefore we have to manipulate the amplitude and phase information separately and use the set-up of Fig. 5.1 as described in Section 5.1. The result is the interpolation in terms of amplitude and phase separately rather than the ideal case of interpolation with complex values. Furthermore the interpolation is actually related to the amplitude and phase indirectly through the nonlinear relationship between exposure E and the amplitude A and phase θ as discussed in Section 5.2. For example for the amplitude part we may have a piecewise linear t-E curve (where t is proportional to A) or linear D-log E curve and for the phase part we may have linear θ-E curve or linear θ-log E curve. Even if we choose linear functions for both amplitude and phase, we still don't have the desired interpolation. First of all the ideal interpolation is in terms of amplitude and phase together. Furthermore even if we consider the phase part only, as in a kinoform, the function to be interpolated should be $e^{j\theta}$ instead of θ as we have here. This also leads to errors with phase

discontinuities from 0 to 2π or vice versa.

Instead of using low-pass filtering, it is possible to use the defocusing method as an alternative to make the continuous hologram. However due to the use of point source for illumination, the depth of focus is large and the extent of defocusing is hard to control quantitatively. Experimental results show that the low-pass filtering is much better. As a matter of fact the defocusing method does not simplify the complexity of the method. The binary patterns, calibration, and alignment etc. are still required.

5.4.2 Other errors

Other errors include the noise due to the phase coding which has been discussed in Chapter 2. During the manufacture of the hologram we may further get amplitude and phase distortions and alignment errors.

The amplitude and phase distortions are the result of variations in exposure from one experiment to the other. The variation of the effective exposure arises from changes in the brightness of the light source, the film speed, and the photographic processing. For simplicity let us assume that these distortions change the amplitude and phase by a constant factor. That is, a desired function $Ae^{j\theta}$ has an

actual representation of $aAe^{jM\theta}$. Apparently the factor a does not affect the fidelity of the reconstruction while M does. When $M \neq 1$ it is usually called phase mismatch and is analyzed by Kermisch [5-8] for the case of a kinoform. His result shows that the intensity of the desired reconstruction is proportional to $\text{sinc}^2(M-1)$ while the nth order term, $\mathfrak{F}^{-1}\{e^{jn\theta}\}$, has an intensity proportional to $\text{sinc}^2(M-n)$. When M = 1 we have the desired reconstruction only since $\text{sinc}^2(1-n) = 0$ for all $n \neq 1$. For the undermodulated case (M < 1) the bright spot at the center starts to show up and for the overmodulated case (M > 1) the convolution of reconstruction with itself starts to dominate which occupies twice of the width of the desired reconstruction. Computer simulation of these mismatches will be shown in Section 5.4.3.

When making a continuous hologram by using the set-up in Fig. 5.1, we have to align the two patterns carefully. Two pairs of cross hairs are plotted near the opposite corners of the pattern (Fig. 5.8) for the alignment purposes. Assuming the following Fourier transform pairs $h(x,y) \Leftrightarrow H(u,v) = A(u,v)e^{j\theta(u,v)}$, $h_1(x,y) \Leftrightarrow A(u,v)$, and $h_2(x,y) \Leftrightarrow e^{j\theta(u,v)}$ then the convolution theorem yields

$$h(x,y) = \iint_{-\infty}^{\infty} A(u,v)e^{j\theta(u,v)}e^{j2\pi(ux+vy)}dudv$$
$$= h_1(x,y)*h_2(x,y) \quad . \tag{5-21}$$

Now in the case of a slight translation error we have $A(u-a,v-b)$, where a,b are small compared with the size of the hologram, and $h_1(x,y)$ becomes $h_1(x,y)e^{j2\pi(ax+by)}$. The reconstruction is now given by

$$h'(x,y) = [e^{j2\pi(ax+by)}h_1(x,y)]*h_2(x,y)$$
$$\simeq\{[1+j2\pi(ax+by)-4\pi^2(ax+by)^2+\ldots] \tag{5-22}$$
$$h_1(x,y)\}*h_2(x,y)$$

where the high orders of the expansion can be dropped since a,b are small. If the impulse response $h(x,y)$ is phase coded then $h_1(x,y)$ is very close to a delta function. Therefore the large values of x,y do not contribute much in the expansion and we have

$$[1+j2\pi(ax+by)-4\pi^2(ax+by)^2+\ldots]h_1(x,y)$$
$$\simeq h_1(x,y) \tag{5-23}$$

and

$$h'(x,y) \simeq h(x,y) \quad . \tag{5-24}$$

Other alignment errors include magnification and rotation errors. The experimental work has shown that satisfactory results can be obtained by using the two pairs of cross

hairs for alignment.

5.4.3 Computer simulations

Computer simulation has been performed on the interpolation of different functions (amplitude and phase) by embedding the inverse Fourier transform of the patterns in a big zero array and then transforming back. This is equivalent to a sinc interpolation of the holograms (as described in Chapter 4) assuming the hologram is extended periodically. For simplicity we assume a linear t-E curve and θ-E curve so that the interpolation can be performed on amplitude (A) and phase (θ) directly. The interpolated amplitude and phase are then combined together to reconstruct the impulse response.

Figure 5.14 shows the computer simulations of the sampled ROACH and continuous ROACH. The high orders of the reconstruction from the sampled ROACH are strongly attenuated by the sinc function but are still visible. The reconstruction from the continuous ROACH, however, has only one single order present with some background noise due to the non-ideal interpolation. Notice the two dots located to the right and to the bottom of the letter 'P' which also appear in the optical reconstruction as will be shown in Section 5.5.

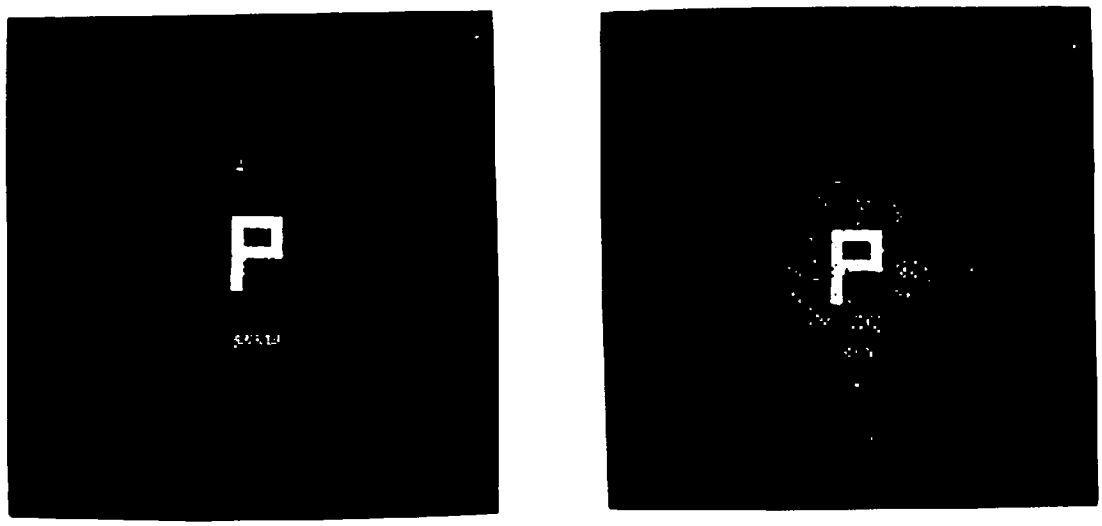

(a) sampled ROACH (b) continuous ROACH

Fig. 5.14 Computer simulations of sampled ROACH and continuous ROACH

The effect of phase mismatch is also studied by simulation. These results confirm the analysis by Kermisch [5-8]. Figure 5.15 shows the computer simulation of phase mismatch on sampled kinoform. A similar simulation is then performed for continuous kinoform as shown in Fig. 5.16. These results show that when $M < 1$ (undermodulation) the bright spot dominates and when $M > 1$ (overmodulation) the convolution terms start to show up.

5.5 Experimental results

In the set-up of Fig. 5.1 we may use lasers of different wavelengths to illuminate the amplitude pattern and phase pattern. In fact this would reduce the exposure cross talk as we discussed in Section 5.3.3. Unfortunately the image produced by using a laser has unavoidable coherent noise due to the defects and dust in the imaging system. This noise can be eliminated by using a moving diffuser. However this set-up requires two lasers and two diffusers and makes the system more complicated. Therefore we use a 75 watt Xenon arc lamp which has a nearly uniform spectrum in the visible region. The arc lamp has a arc length of 300 μ and is considered a good point source. Actually the output from the arc lamp contains much scattered light and therefore we have the beam illuminating a diffuser through a diaphragm. A better point source then

(a) M=0.5

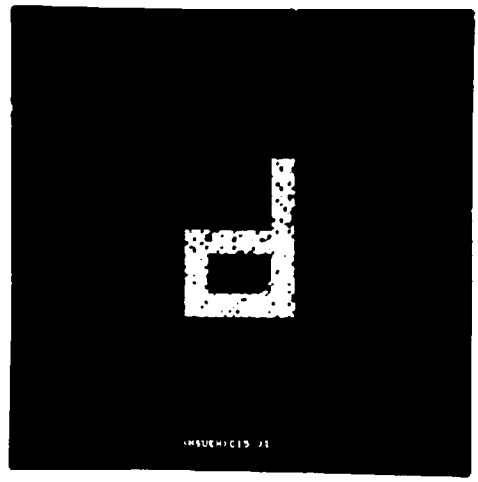

(b) M=-1

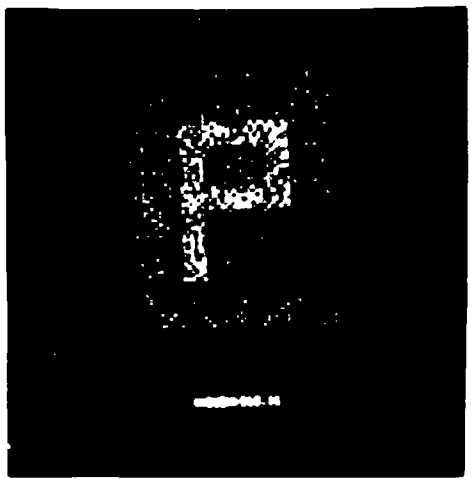

(c) M=1.5

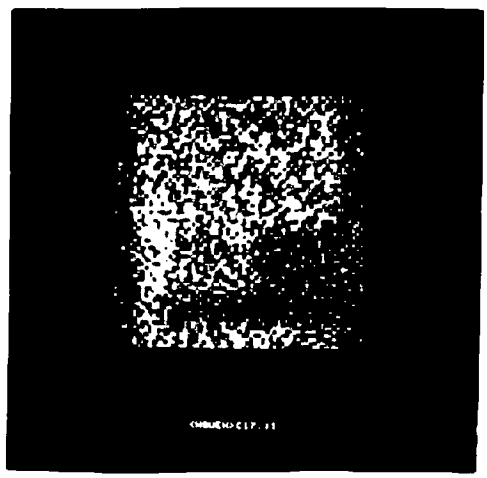

(d) M=2

Fig. 5.15 Computer simulations of phase mismatch (sampled kinoform)

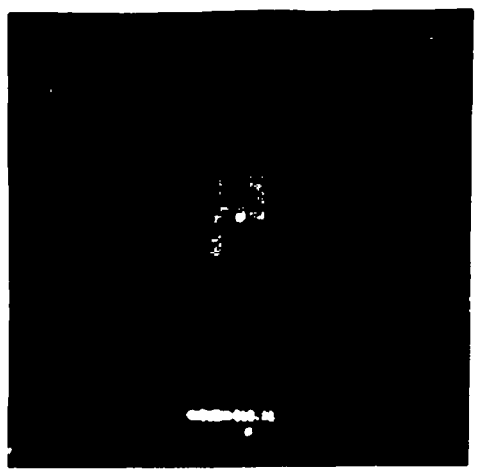

(a) M=0.5

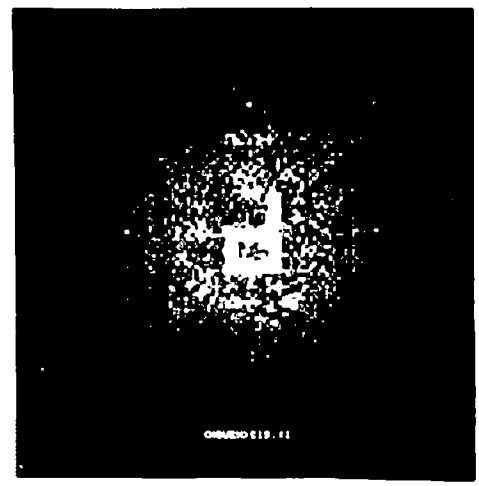

(b) M=-1

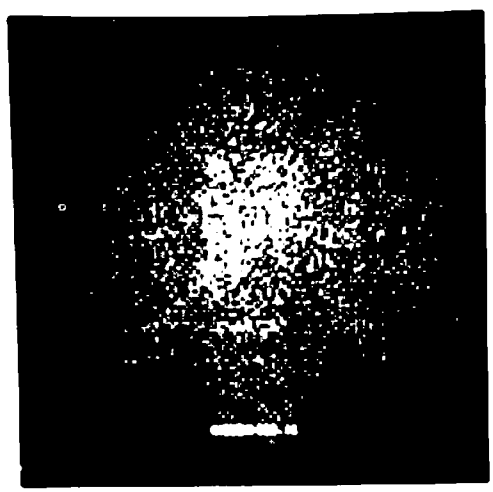

(c) M=1.5

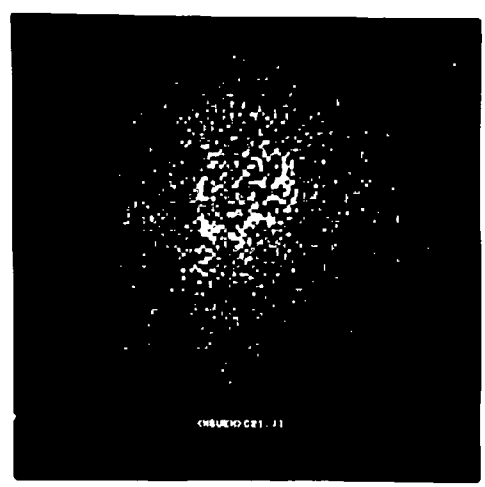

(d) M=2

Fig. 5.16 Computer simulations of phase mismatch (continuous kinoform)

can be obtained by controlling the diaphragm. Spatial filtering can be accomplished easily by using this source while coherent noise is eliminated. Different colors in the two paths are obtained by inserting two Kodak Wratten filters (No. 25 for red and No. 38A for blue and green).

After the characteristic curves for the amplitude and phase are obtained from the calibration, the binary patterns are made according to these curves using the same method as we used to make the binary holograms in Chapter 3. These patterns are put into the set-up of Fig. 5.1 to make continuous holograms. Sampled holograms are also made by using the Dicomed D-47 Image Recorder for comparisons with continuous holograms.

Figures 5.17 and 5.18 are the reconstructions of the sampled ROACH and continuous ROACH respectively for a phased coded object. Figure 5.18 has only a single order with some background noise. Notice that the two bright spots to the right and at the bottom also appear in the computer simulation (Fig. 5.14(b)). Due to the nature of phase coding (as discussed in Chapter 2), speckle-like noise appears in both reconstructions. The reconstructions look smoother for the zero phase object as shown in Figs. 5.19 and 5.20. However both have difficulty in representing the amplitude due to the large dynamic range

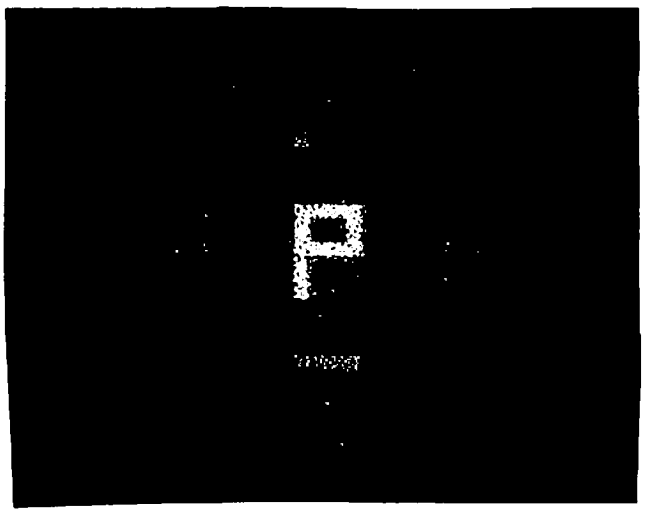

Fig. 5.17 Reconstruction of sampled ROACH (phase coded object)

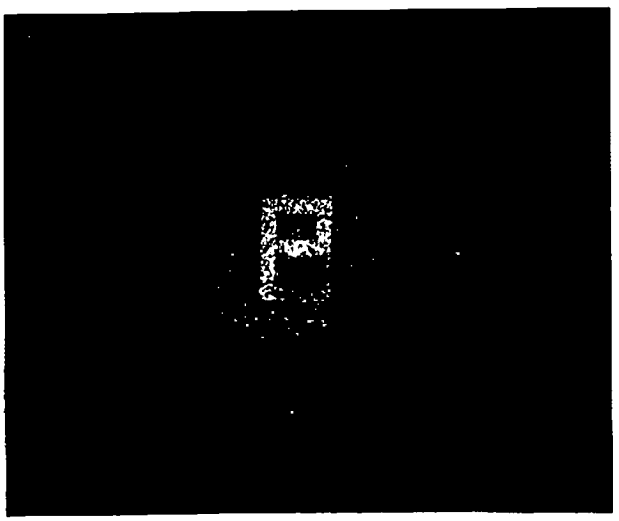

Fig. 5.18 Reconstruction of continuous ROACH (phase coded object)

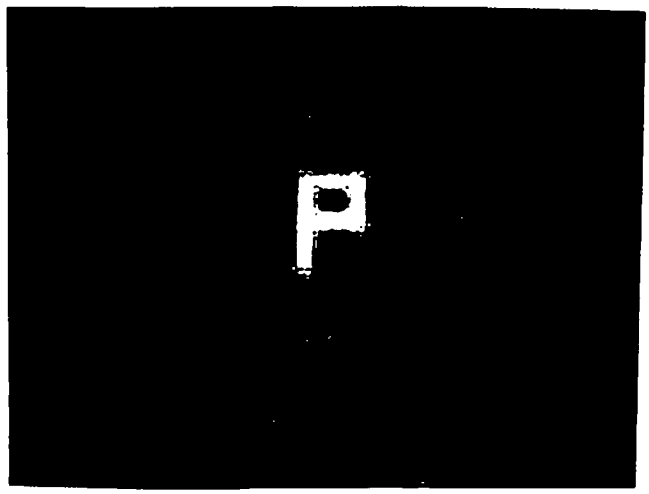

Fig. 5.19 Reconstruction of sampled ROACH (zero phase object)

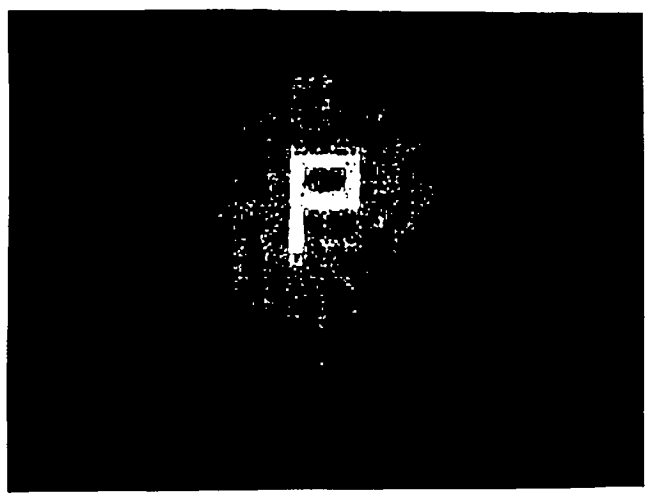

Fig. 5.20 Reconstruction of continuous ROACH (zero phase object)

required and the fact that most of the Fourier components are small.

The continuous hologram requires extra care to align the images of the two patterns. Experiment shows that the two pairs of cross hairs (Fig. 5.8) are sufficient for alignment purpose. Figures 5.21 and 5.22 show the reconstructions of holograms with translation, and rotation errors made intentionally. The translation error is 1.75 pixels outofa total of 64 pixels in one direction and the rotation error is 4 degrees. Images are degraded due to these errors.

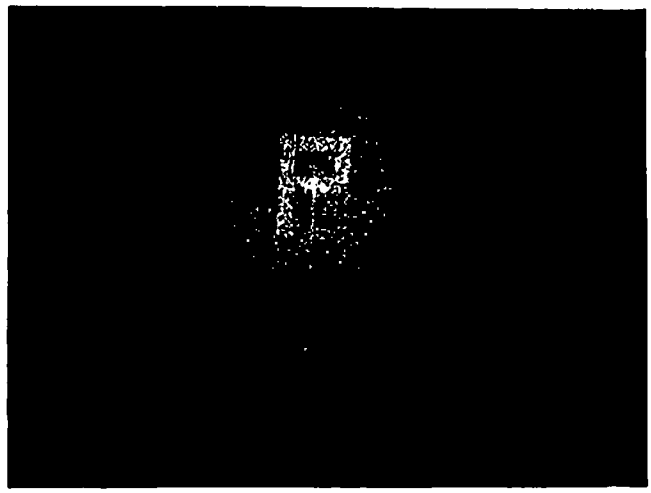

Fig. 5.21 Reconstruction of continuous ROACH with translation error

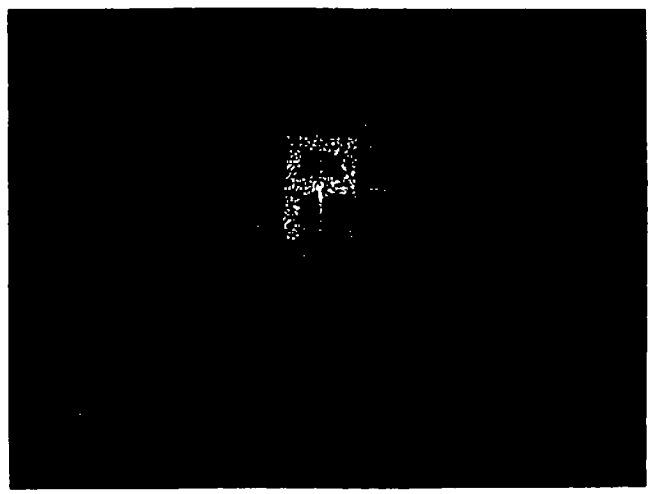

Fig. 5.22 Reconstruction of continuous ROACH with rotation error

CHAPTER 6

APPLICATION: MATCHED FILTERS

6.1 Introduction

As we have discussed in the previous chapters, when a computer-generated sampled hologram is used as a filter in a filtering system, the size of the input to this system has to be constrained so that different orders in the output plane do not overlap. This problem can be alleviated by using a two-step method [6-1, 6-2, 6-3]. In the two-step method a computer-generated hologram is made first at the sampling rate determined by the impulse response. The interference pattern of one order of the reconstruction and a separately generated reference wave is then recorded as the desired filter. In this way the filter can be generated with low spatial frequency and then modulated onto an arbitrarily high carrier frequency. Bartelt et al. [6-4] developed a technique that uses a step-and-repeat camera to replicate a binary hologram in order to increase the carrier frequency of the hologram. Yatagai [6-5] has described an interpolation method to achieve the same goal.

All these methods have relaxed the constraint on the size of the input but basically the constraint still exists. The continuous hologram described in Chapter 5 essentially eliminates this problem. In this chapter we will demonstrate this by applying the hologram to an optical character recognition system. Since Vander Lugt's [6-6] invention of the optical matched filtering, character recognition can be done optically at the speed of light. The computer-generated hologram [6-7, 6-8] further increases the flexibility of optical filtering by allowing one to design a filter for better recognition. Incoherent systems [6-9, 6-10] have also been proposed which eliminate the problems of the incoherent-to-coherent conversion and the critical filter alignment in the coherent system. In related work the use of principal components [6-11, 6-12, 6-13] has reduced the number of filters required for optical character recognition. Using this idea only five filters rather than thirty-two filters are required for identifying a set of thirty-two characters.

Although many better methods are available for character recognition, we will use the matched filter in this chapter to demonstrate how the continuous hologram solves the problem associated with the sampled hologram. Some modifications related to the matched filter which improve the performance will be discussed.

6.2 Matched filters

6.2.1 System description

A character recognition system may be described in the following manner. The input g to the system may consist of any one of N possible characters $s_1,\ldots,s_N$ and the task of the system is to determine the particular input character. A system using matched filters for this purpose has been described by Goodman [6-14]. Figure 6.1 shows the block diagram of the system. It consists of N matched filters $S_1^*,\ldots,S_N^*$, where S_n^* is the complex conjugate of the Fourier transform of s_n followed by a normalization operation to account for the different energy of each possible character. The center value of the squared moduli of the output are then compared. Note that the normalization operation can be built-in as part of the filter or compensated at the detector. If the input g happens to be s_k then the kth output will give the largest response. Let V_n be the output of the nth channel in Fig. 6.1 then V_n is given by

$$V_n(x,y) = \frac{\displaystyle\iint_{-\infty}^{\infty} s_k(\xi,\eta)\, s_n^*(\xi-x,\eta-y)\, d\xi d\eta}{\left[\displaystyle\iint_{-\infty}^{\infty} |s_n(\xi,\eta)|^2 d\xi d\eta\right]^{\frac{1}{2}}} \qquad (6\text{-}1)$$

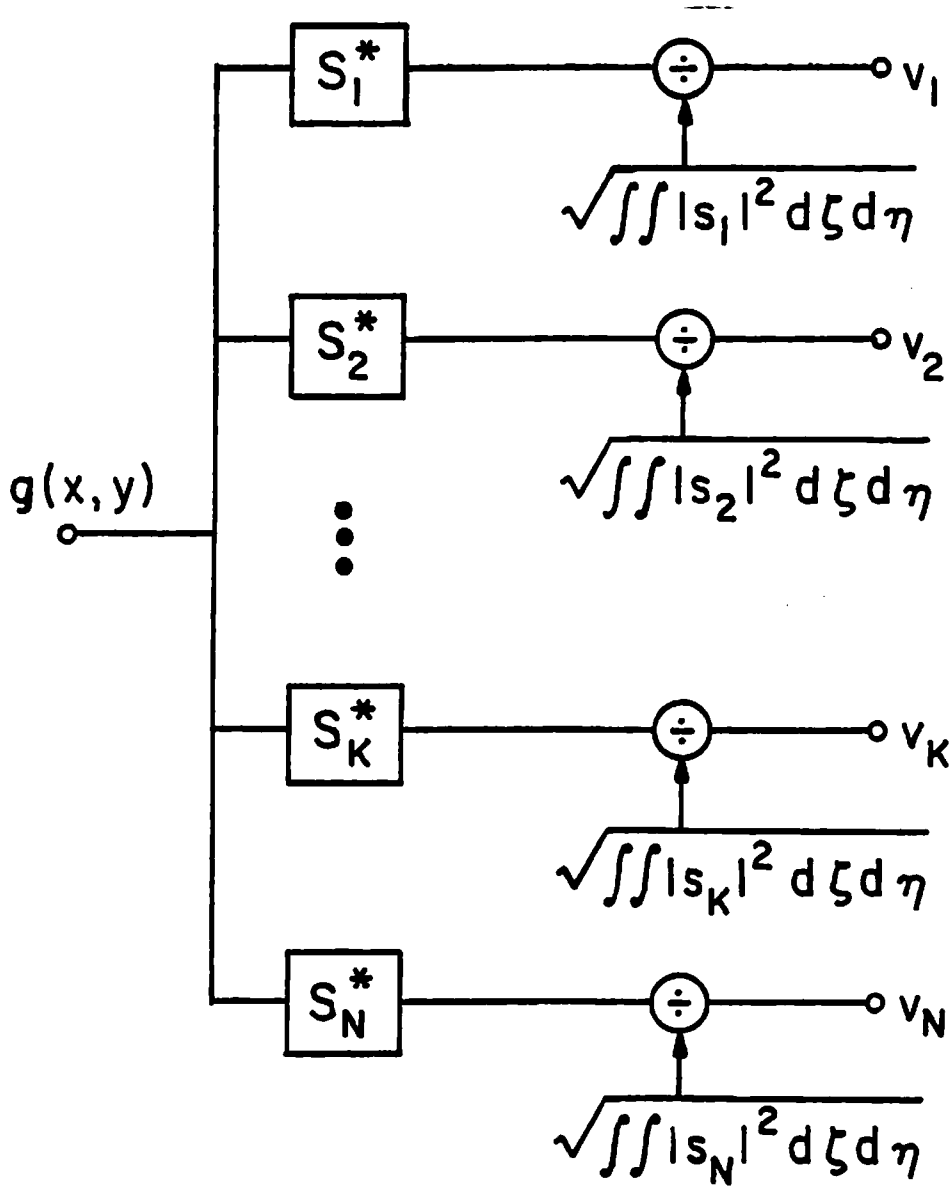

Fig. 6.1 Block diagram of a character recognition system with single input

The squared modulus at the center (x=y=0) is given by

$$|V_n(0,0)|^2 = \frac{\left|\int\int_{-\infty}^{\infty} s_k(\xi,\eta)\, s_n^*(\xi,\eta)\, d\xi d\eta\right|^2}{\int\int_{-\infty}^{\infty} |s_n(\xi,\eta)|^2 d\xi d\eta} \qquad (6\text{-}2)$$

the output $|V_k(0,0)|^2$ of the correct matched filter has a simpler form

$$\begin{aligned} |V_k(0,0)|^2 &= \frac{\left[\int\int_{-\infty}^{\infty} |s_k(\xi,\eta)|^2 d\xi d\eta\right]^2}{\int\int_{-\infty}^{\infty} |s_k(\xi,\eta)|^2 d\xi d\eta} \\ &= \int\int_{-\infty}^{\infty} |s_k(\xi,\eta)|^2 d\xi d\eta \quad . \end{aligned} \qquad (6\text{-}3)$$

By using Schwarz' inequality, we have

$$\begin{aligned} &\left|\int\int_{-\infty}^{\infty} s_k(\xi,\eta)\, s_n^*(\xi,\eta)\, d\xi d\eta\right|^2 \\ &\leq \int\int_{-\infty}^{\infty} |s_k(\xi,\eta)|^2 d\xi d\eta \quad \int\int_{-\infty}^{\infty} |s_n(\xi,\eta)|^2 d\xi d\eta \quad . \end{aligned} \qquad (6\text{-}4)$$

It follows that

$$|V_n(0,0)|^2 \leq \iint_{-\infty}^{\infty} |s_k(\xi,\eta)|^2 d\xi d\eta = |V_k(0,0)|^2 \qquad (6\text{-}5)$$

with equality if and only if

$$s_n(x,y) = c\, s_k(x,y) \qquad (6\text{-}6)$$

where c is a constant.

Therefore the input character can be recognized by comparing the center values of the outputs.

Another optical character recognition system involves detecting a certain key word on a page. This system is shown in the diagram of Fig. 6.2. Instead of a single input we now have an input of N characters with a single filter. In this case the use of a sampled hologram as a filter may produce an overlap problem because of the fact that the input has large format and the sampled filter produces periodic responses of period distance less than the format extent. Due to the possible different energies of each input signal, normalization is also necessary. In contrast to the first system, this normalization can only be done at the detector rather than being built into the filter. The normalization value can be obtained by using another imaging system and integrating the energy over the corresponding area. Although there are N filters shown in

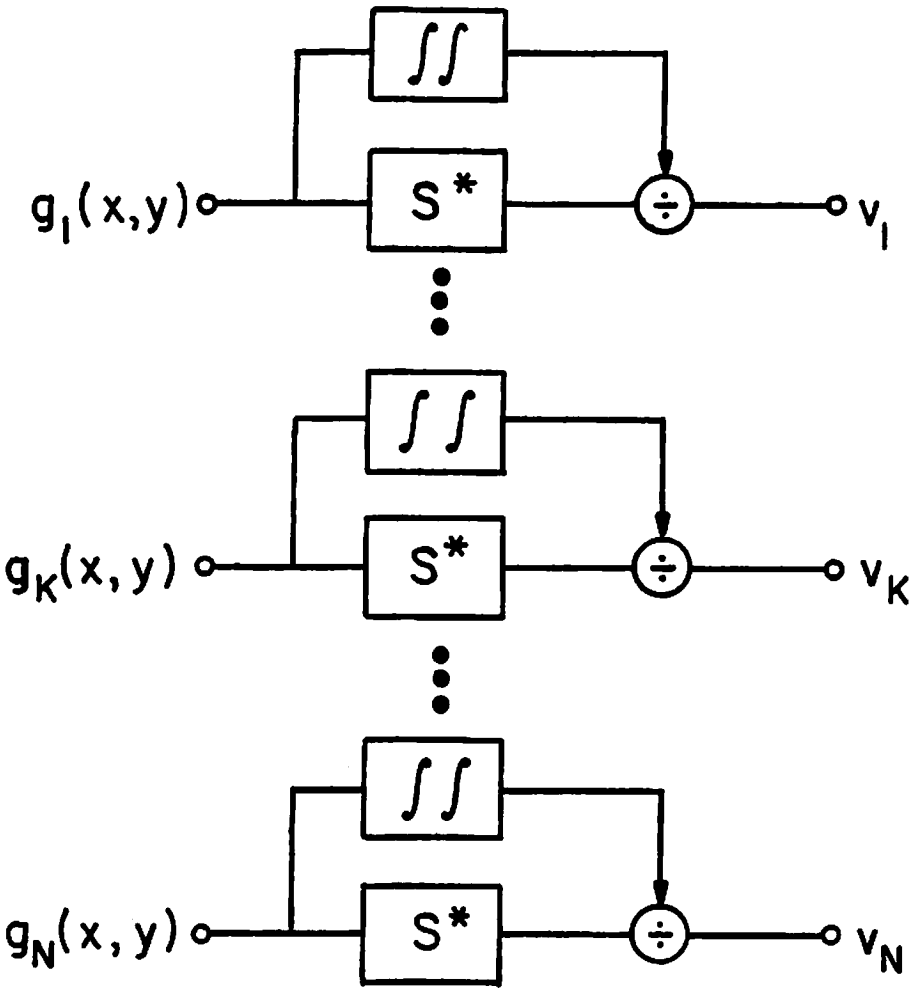

Fig. 6.2 Block diagram of a character recognition system with multiple inputs

Fig. 6.2 for clarity, only one filter is sufficient since different outputs will appear at different locations in the output plane. The performance of this system can be shown similarly as the first system except the roles of the input and the impulse response are exchanged. We now have input $s_n(x,y)$, n=1,...,N and impulse response $s_k^*(-x,-y)$. The subscripts n and k in the numerator of Eq. (6-2) and in Eq. (6-4) are exchanged. The results similar to Eqs. (6-5) and (6-6) are then obtained.

6.2.2 Basic set-up

The filtering operation in each channel of Figs. 6.1 and 6.2 can be implemented in different ways. Here we choose a set-up which can be operated under coherent or incoherent illumination without any change [6-15]. Figure 6.3 shows the set-up along with the input s(x,y) and the matched filter $S^*(u,v)$ where (u,v) are the coordinates in the Fourier transform domain. In the incoherent case the input s(x,y) is either self-luminous or illuminated by an extended source. To show that the same set-up can be used under the incoherent illumination, we first consider the input intensity

$$I_s(x,y) = |s(x,y)|^2 \qquad (6-7)$$

since the incoherent system is linear in intensity. Let

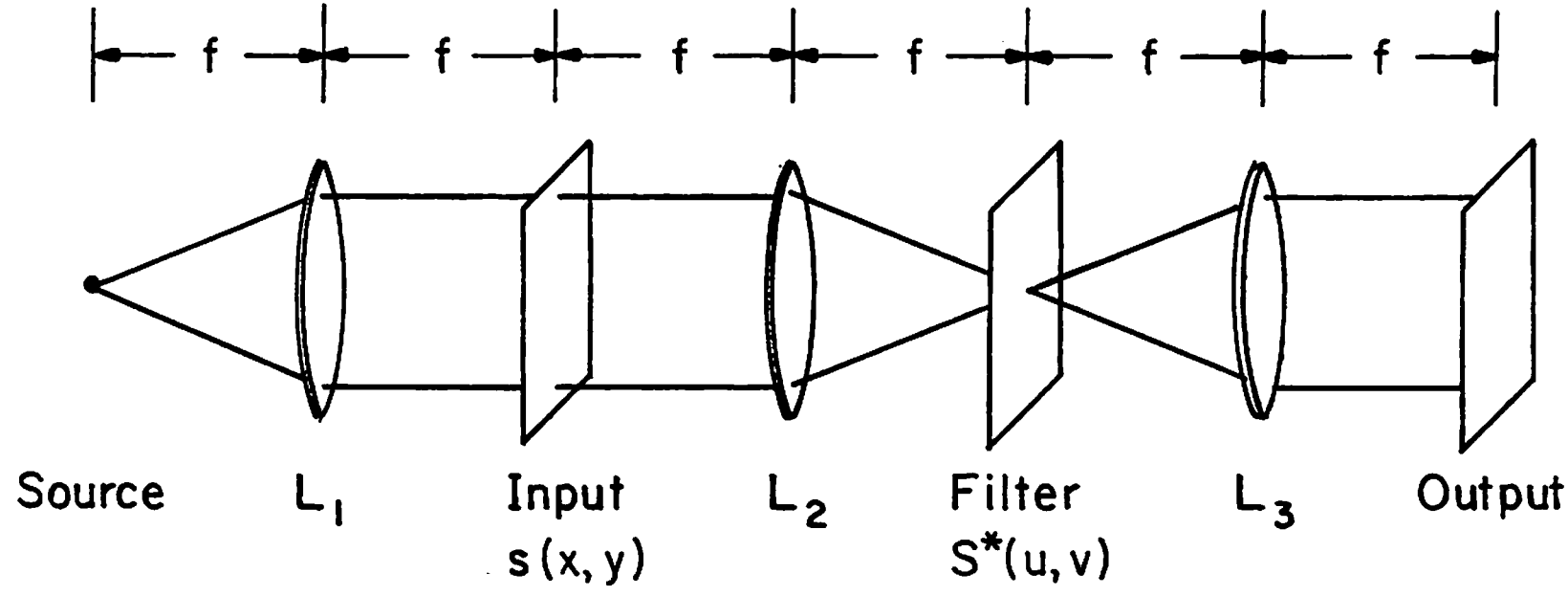

Fig. 6.3 Matched filtering set-up

$\tilde{I}_s(u,v)$ be the Fourier transform of $I_s(x,y)$, then the matched filter should have an OTF proportional to the complex conjugate of $\tilde{I}_s(u,v)$. The corresponding impulse response is given by

$$\mathfrak{F}^{-1}\{\tilde{I}_s^*(u,v)\} = I_s^*(-x,-y) = I_s(-x,-y) \quad . \quad (6\text{-}8)$$

Here we have neglected the constant factor. The last equality follows by the fact that intensity is non-negative, $I_s(x,y) \geq 0$. The complex transmittance of the impulse response is given by

$$\{I_s^{1/2}(-x,-y)e^{-j\phi(-x,-y)}\} \quad (6\text{-}9)$$

where we have added the phase $-\phi(-x,-y)$ which does not affect the impulse response (in intensity) and can be assigned arbitrarily. Therefore we have the matched filter given by

$$S_m(u,v) = \mathfrak{F}\{I_s^{1/2}(-x,-y)e^{-j\phi(-x,-y)}\} \quad . \quad (6\text{-}10)$$

When $s(x,y)$ is real and non-negative we can choose $\phi(x,y)=0$ and the quantity in brackets becomes

$$I_s^{1/2}(-x,-y)e^{-j\phi(-x,-y)} = s^*(-x,-y) \quad . \quad (6\text{-}11)$$

Even if $s(x,y)$ is a complex function, we can still satisfy Eq. (6-11) by assigning

$$\phi(x,y) = \frac{s(x,y)}{|s(x,y)|} \quad (6\text{-}12)$$

that is, the phase angle of $s(x,y)$. By substituting Eq. (6-11) in Eq. (6-10) we get

$$S_m(u,v) = \mathcal{F}\{s^*(-x,-y)\} = S^*(u,v) \quad . \tag{6-13}$$

Therefore the same filter can be used in incoherent illumination. Although we can use the same filter for an incoherent system, it is more practical to use phase coding to improve the light efficiency [6-9] of the system.

Equation (6-10) can be further simplified to an expression in terms of $I_s^{1/2}(x,y)$

$$\begin{aligned} S_m(u,v) &= \int_{-\infty}^{\infty}\int \{I_s^{1/2}(-x,-y)e^{-j\phi(-x,-y)}\}e^{-j2\pi(ux+vy)}dxdy \\ &= \int_{-\infty}^{\infty}\int \{I_s^{1/2}(x',y')e^{-j\phi(x',y')}\} \\ &\qquad e^{-j2\pi(-ux'-vy')}dx'dy' \\ &= \mathcal{F}\{I_s^{1/2}(x,y)e^{-j\phi(x,y)}\}_{u,v \to -u,-v} \quad . \end{aligned} \tag{6-14}$$

That is, we can phase code $I_s^{1/2}(x,y)$, take the Fourier transform then reverse the coordinates in the transform domain. We can also write Eq. (6-14) as

$$S_m(u,v) = \iint_{-\infty}^{\infty} I_s^{1/2}(x,y)e^{-j\phi(x,y)}e^{j2\pi(ux+vy)}dxdy$$

$$= [\iint_{-\infty}^{\infty} I_s^{1/2}(x,y)e^{j\phi(x,y)}e^{-j2\pi(ux+vy)}dxdy]^* \quad (6\text{-}15)$$

$$= [\mathfrak{F}\{I_s^{1/2}(x,y)e^{j\phi(x,y)}\}]^* \quad .$$

Therefore the matched filter can also be obtained by phase coding $I_s^{1/2}(x,y)$ followed by transformation and conjugation. From Eq. (6-14) to Eq. (6-15) we have taken advantage of the fact that $\phi(x,y)$ can be manipulated arbitrarily. The phase terms $e^{-j\phi(x,y)}$ and $e^{j\phi(x,y)}$ in Eqs. (6-14) and (6-15) are complex conjugate in form, however, due to the use of phase coding they could actually be the same.

6.2.3 Phase-only matched filter

The two systems described in Section 6.2.1 use the same principle. The input is classified by measuring the energy at the center of the responses from different channels. Unfortunately the center may not be well defined in the real situation. Referring to Fig. 6.3, suppose the input is $g(x,y)$ with the Fourier transform $G(u,v)$ then the wavefront exiting from the filter is $G(u,v)S^*(u,v)$. In the output plane we have $\mathfrak{F}^{-1}\{G(u,v)S^*(u,v)\}$. If the input is matched to the filter, i.e. $g(x,y)=s(x,y)$, then

$$G(u,v)S^*(u,v) = |S(u,v)|^2 \qquad (6\text{-}16)$$

and the wavefront has zero phase. Therefore the output $\mathcal{F}^{-1}\{|S(u,v)|^2\}$ has a maximum at the center and we can simply measure the peak value of the output. However, if the input is not matched, then the product $G(u,v)S^*(u,v)$ does not have zero phase. The maximum may not occur at the center and the measurement of peak value may give values larger than expected. Therefore it is more practical to design a filter which produces a sharp peak response for the correct input and we can simply look for a sharp peak in the output plane to locate the desired character with the possible use of energy normalization.

In most of these applications the input $s(x,y)$ has zero phase and therefore its Fourier transform $S(u,v)$ has a very large dynamic range with most of the energy concentrated at low frequency components. The wavefront exiting from the matched filter is the squared modulus of $S(u,v)$ and has an even sharper peak approximating a delta function. Therefore, in the output plane even though the maximum is still at the center, the shape of the response may not look very sharp and classification is more difficult to make. In the ideal case we would like to have a delta function present in the output plane for the correct input. Therefore instead of using a matched filter

$S^*(u,v)$, we require a new filter $H(u,v)$ such that

$$S(u,v)H(u,v) = \text{constant}. \tag{6-17}$$

By choosing the constant equal to 1 we have

$$H(u,v) = \frac{1}{S(u,v)} \tag{6-18}$$

which is the inverse filter. The inverse filter is impractical in the presence of noise [6-16] and has low light efficiency (see Appendix B).

In fact there is a compromise between the matched filter and inverse filter. Note that the matched filter is given by

$$S^*(u,v) = \frac{S^*(u,v)}{|S(u,v)|^0} \tag{6-19}$$

and the inverse filter is given by

$$\frac{1}{S(u,v)} = \frac{S^*(u,v)}{S(u,v)S^*(u,v)} = \frac{S^*(u,v)}{|S(u,v)|^2} \tag{6-20}$$

In between we may choose a filter

$$H(u,v) = \frac{S^*(u,v)}{|S(u,v)|} \tag{6-21}$$

which is the phase part of the matched filter and will be called a "phase-only matched filter". Let us assume

$$r(x,y) = \mathcal{F}^{-1}\{|S(u,v)|\} \tag{6-22}$$

then in the output plane the inverse filter gives

$$\mathcal{F}^{-1}\{S(u,v)\cdot \frac{1}{S(u,v)}\} = \delta(x,y) \tag{6-23}$$

while the phase-only matched filter and matched filter give

$$\begin{aligned}\mathcal{F}^{-1}\{S(u,v)\cdot \frac{S^*(u,v)}{S(u,v)}\} &= \mathcal{F}^{-1}\{|S(u,v)|\} \\ &= r(x,y)\end{aligned} \tag{6-24}$$

and

$$\begin{aligned}\mathcal{F}^{-1}\{S(u,v)S^*(u,v)\} &= \mathcal{F}^{-1}\{|S(u,v)|^2\} \\ &= r(x,y)*r(x,y)\end{aligned} \tag{6-25}$$

respectively. It can be shown (see Appendix B) that the light efficiency and the sharpness of the peak are improved in the phase-only matched filter case. Furthermore the new filter is easy to make by the on-axis hologram technique. For example, no cross talk occurs when we use the ROACH method. Kadkly [6-17] has compared the performance of different optical matched filters, namely pure amplitude, pure phase, and complex filters, for the simple case of an isolated single slit. He also concluded that the pure phase filter has better efficiency and the peak value falls off rapidly when the slit width departs from the ideal one.

The pure phase filter is easy to make in the single slit case since it contains only bands of 0 and π phase shift. It is worth noting that the inverse filter or phase-only matched filter can not be made with the holographic method since the impulse response does not exist physically. However it is possible to make the filter using the two-step method [6-1, 6-2, 6-3].

The above analysis shows that the phase-only matched filter is preferable in the application of character recognition. It has also been observed [6-18, 6-19] that since most of the characters have similar low frequency spectrum, it is possible to increase the selectivity by suppressing the low frequency components. Similar goalscan be achieved by applying edge enhancement techniques before the filtering [6-20] since the edge structures are different for different characters. The phase-only matched filter assumes constant amplitude in the frequency domain and therefore naturally enhances the high frequency components of the input. Therefore in a sense the phase-only matched filter embodies those techniques. However the phase-only matched filter is derived by considering the wavefront exiting from the filter and has the advantages of high light efficiency and ease of fabrication which other techniques do not have. Further improvement of the performance can be achieved by

suppressing the low frequency components at the expense of increasing the sensitivity to the size, orientation and quality of the input characters [6-18]. Although the phase-only matched filter is most suitable for implementation by on-axis holograms, it is possible to apply it to other types of computer-generated holograms such as the Lohmann hologram.

6.3 Computer simulations

In this section, the performance of different filters will be compared by using computer simulation. They will be tested by applying different inputs. The performance of the filter can be evaluated in terms of its efficiency and selectivity. The peak value of the correct response will be used as the measure of the efficiency. The selectivity of the filter can be determined by comparing the location of the peak and the sharpness of the peak for various inputs. It is desirable that when the filter matches the input, the output has a very sharp peak at the right location, while when the input is not matched the system should not respond with a sharp peak. The effects of errors introduced during the manufacture of the filters, such as quantization and phase mismatch, are also considered in these simulations. As discussed in Chapter 2, the use of phase coding introduces speckle-like

noise. The effect of this noise on the filtering result is also studied.

6.3.1 Performance of different filters in coherent systems

We first compare the performance of different types of filters. In general, even though the input object to be classified has zero phase, a complex signal can be recognized in a coherent system. Here we use a 32x32 array representing the letter P with zero phase as the desired letter to be detected. The matched filter, phase-only matched filter and its high-pass version are then used. The inverse filter will not be used as it is known to have low efficiency and sensitivity to noise.

To test the selectivity of the filters, two incorrect letters are also applied to the system. They are the letter P with a random phase and the letter M with zero phase. Figure 6.4 shows plots of the input intensities for letters P and M. The results obtained from the matched filter are shown in Fig. 6.5. The correct input gives a sharp peak shown in Fig. 6.5(a) while others do not, as shown in Figs. 6.5(b) and 6.5(c). Note that these perspective plots have been normalized to the same height and their absolute and relative peak values are listed in columns 2 and 3 of Table 6.1. The incorrect input results in much lower response. The ratio of the maximum value to

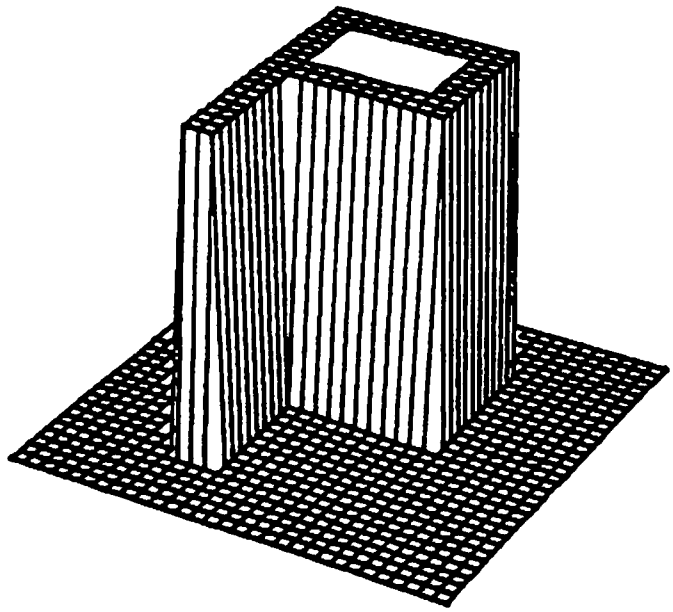

(a) letter P

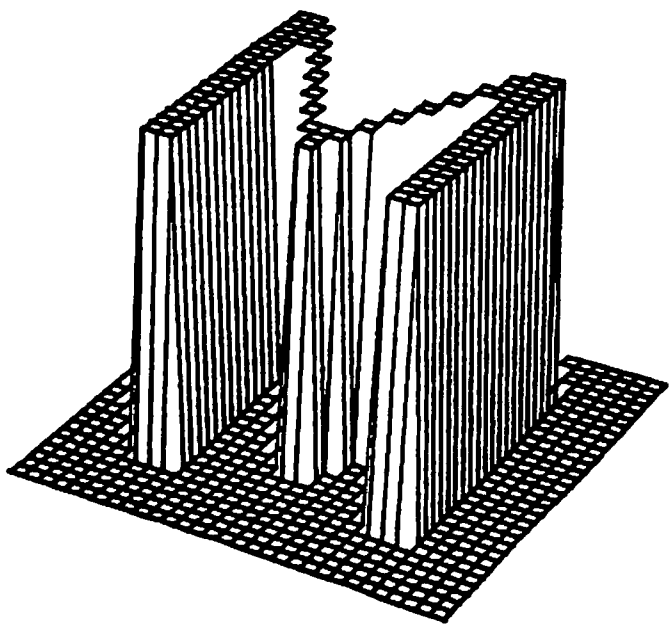

(b) letter M

Fig. 6.4 Inputs to be tested in the character recognition system

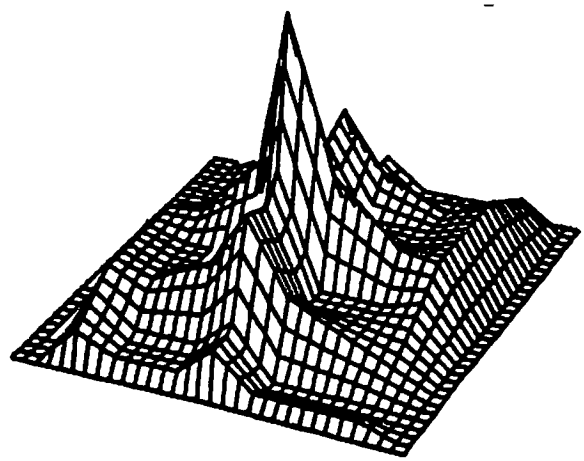

(a) P (zero phase)

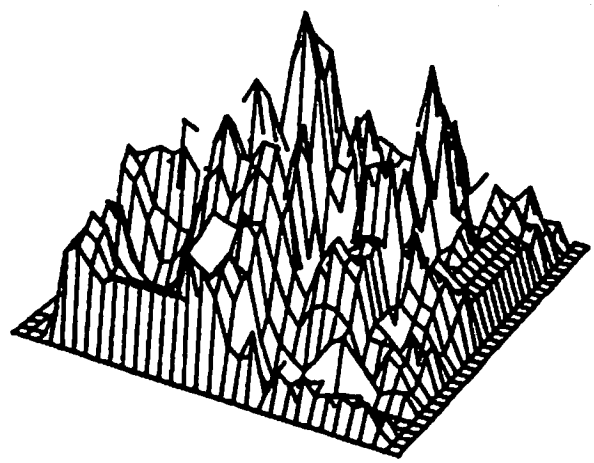

(b) P (random phase)

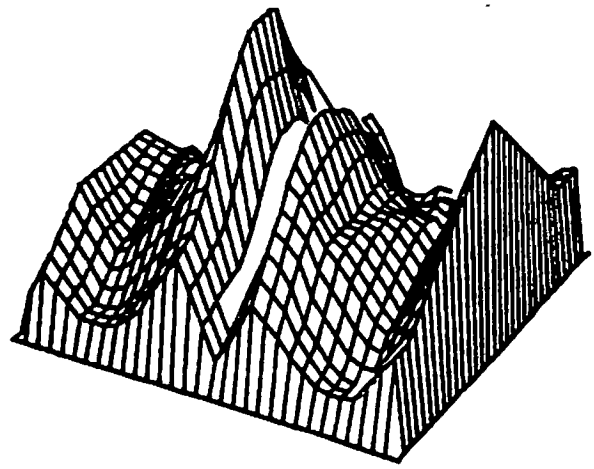

(c) M (zero phase)

Fig. 6.5 Results of the matched filter with different inputs

TABLE 6.1 RESULTS OF THE MATCHED FILTER

INPUT	MAX	MAX(rel.)	MAX/MAX2	Peak Location
P (zero phase)	86.24	1.0	1.185	(17,17)
P (random phase)	9.73	0.113	1.087	(17,18)
M (zero phase)	41.06	0.476	1.014	(14,18)

TABLE 6.2 RESULTS OF THE PHASE-ONLY MATCHED FILTER

INPUT	MAX	MAX(rel.)	MAX/MAX2	Peak Location
P (zero phase)	456.4	1.0	1.875	(17,17)
P (random phase)	119.7	0.262	1.009	(14,15)
M (zero phase)	176.0	0.386	1.116	(14,17)

TABLE 6.3 RESULTS OF THE HIGH-PASS VERSION OF THE PHASE-ONLY MATCHED FILTER

INPUT	MAX	MAX(rel.)	MAX/MAX2	Peak Location
P (zero phase)	233.3	1.0	3.754	(17,17)
P (random phase)	111.0	0.476	1.125	(14,15)
M (zero phase)	91.7	0.390	1.041	(31,17)

the second largest value in the output is also calculated. This gives an indication of the sharpness of the peak. These values are listed in column 4. Finally in column 5 we have the location of the peak value. The correct input gives a peak response at (17,17), which is the center of the 32x32 array, while the others do not give sharp peaks.

The results of the phase-only matched filter are shown in Fig. 6.6 and Table 6.2. Comparing the peak values in Tables 6.1 and 6.2, we note that the efficiency is much improved for the phase-only matched filter. The peak is also sharper as indicated by the values of MAX/MAX2 (1.875 vs. 1.185) and as shown in Fig. 6.6(a). Furthermore the phase-only matched filter tends to destroy the structure of the response from an incorrect input. This is a desired property since it makes the correct response stand out and reduces the possibility of any faulty detection when the machine is used to search for sharp peaks.

It is known [6-18, 6-19] that most characters have similar low frequency spectra so that the selectivity can be increased by suppressing the low frequency part of the matched filter. The same idea can be applied to the phase-only matched filter. Figure 6.7 and Table 6.3 show the result of the phase-only matched filter with the central 11x11 elements of the 32x32 array blocked. The

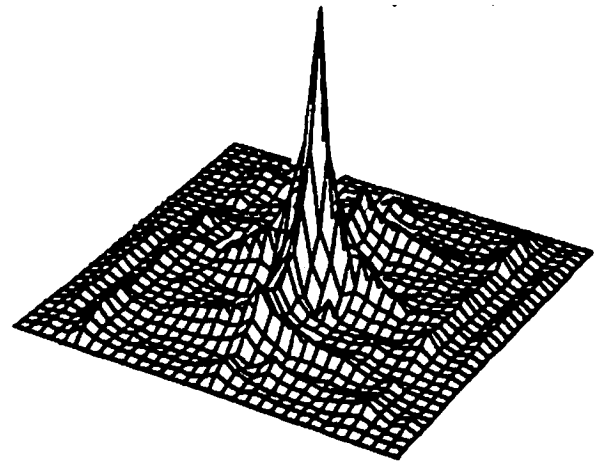

(a) P (zero phase)

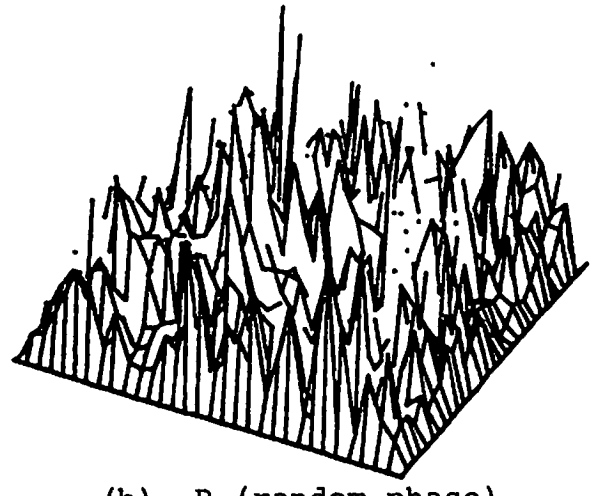

(b) P (random phase)

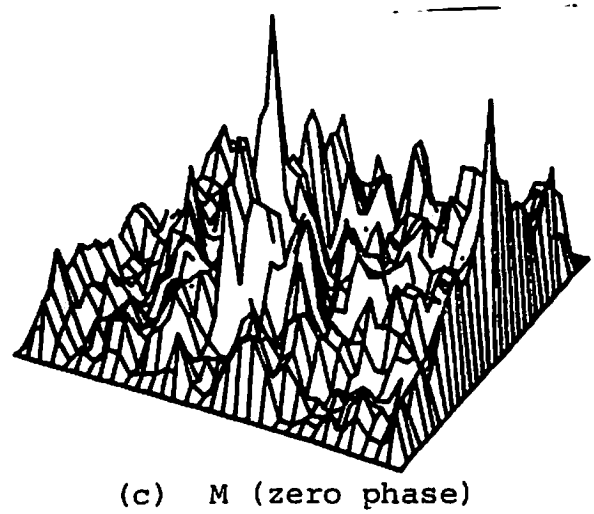

(c) M (zero phase)

Fig. 6.6 Results of the phase-only matched filter with different inputs

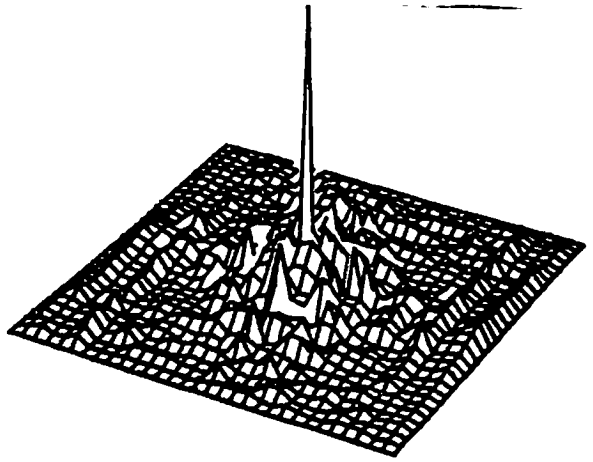

(a) P (zero phase)

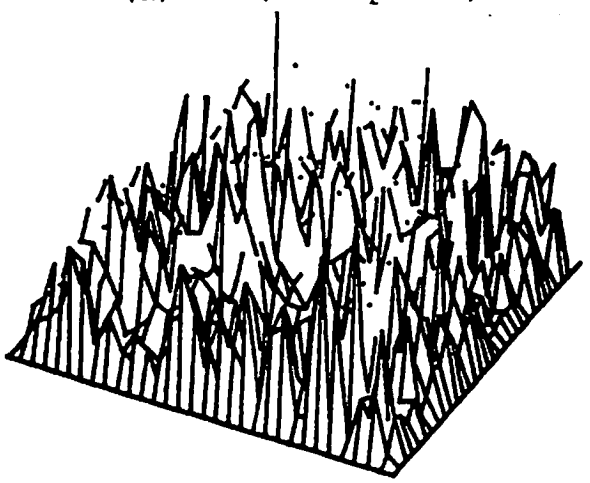

(b) P (random phase)

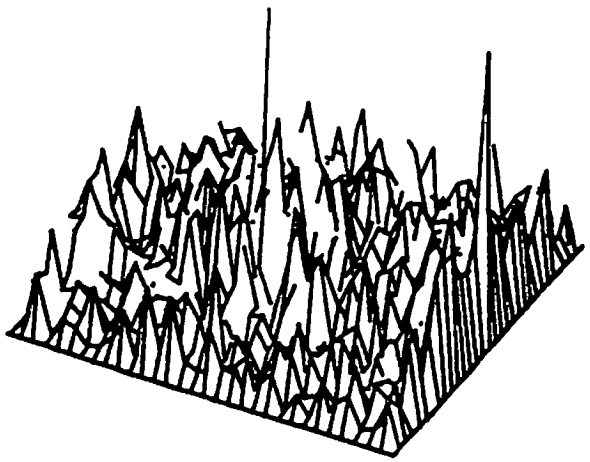

(c) M (zero phase)

Fig. 6.7 Results of the high-pass version of the phase-only matched filter with different inputs

peak values are reduced, however, the sharpness is improved as indicted by the value of MAX/MAX2=3.754 and as shown in Fig. 6.7(a). In addition, the responses in Figs. 6.7(b) and 6.7(c) have even less structure.

The above simulations show that the phase-only matched filter or its high-pass version is definitely superior to the traditional matched filter. The efficiency is increased and the selectivity is improved by making the correct response sharper while destroying the structure of the incorrect responses.

6.3.2 The effect of quantization and phase mismatch

The computer-generated holograms (or filters) suffer from quantization error due to the finite number of quantization levels and, in the case of the ROACH, amplitude error and phase mismatch may also occur. Here we use the phase-only matched filter as an example to investigate the effects of quantization and phase mismatch on the filtering result.

Let $S(u,v)=|S(u,v)|e^{j\theta(u,v)}$ denote the Fourier transform of the input signal $s(x,y)$, then the corresponding phase-only matched filter is given by

$$H(u,v) = e^{-j\theta(u,v)} \quad . \qquad (6\text{-}26)$$

Due to the quantization error or phase mismatch we have a non-ideal filter

$$H'(u,v) = e^{-j\alpha(u,v)\theta(u,v)} \quad , \qquad (6\text{-}27)$$

where $\alpha(u,v)\theta(u,v)$ is the phase obtained after quantization and phase mismatch. In the ideal case we have $\alpha(u,v)=1$. Therefore in the output plane we get

$$\iint_{-\infty}^{\infty} S(u,v)H'(u,v)e^{j2\pi(ux+vy)}dudv$$

$$= \iint_{-\infty}^{\infty} |S(u,v)|e^{j(1-\alpha(u,v))\theta(u,v)}e^{j2\pi(ux+vy)}dudv. \qquad (6\text{-}28)$$

It is obvious that the value at the center (x=y=0) reaches the maximum when no phase error occurs ($\alpha(u,v)=1$). Therefore the errors introduced by quantization and phase mismatch tends to reduce the center value as shown in columns 3 and 4 of Table 6.4. The error in phase ($\alpha(u,v)\neq 1$) may cause the peak to occur somewhere other than the center. However for those parameters we have tried in Table 6.4, the correct detection is still obtained. Figure 6.8 shows the responses for phase-only matched filters with 30% phase mismatch (phase factor=0.7) and four quantization levels respectively. Sharp peaks are still obtained in the output plane even though the peak values and the sharpness are reduced. Finally in Fig. 6.9 and

TABLE 6.4 THE EFFECT OF QUANTIZATION AND PHASE MISMATCH ON THE FILTERING RESULT

Quantization Levels	Phase Factor	MAX	MAX(rel.)	MAX/MAX2	Peak Location
----	1.0	456.4	1.0	1.875	(17,17)
----	0.8	419.2	0.918	1.752	(17,17)
----	0.7	374.9	0.821	1.683	(17,17)
17	1.0	453.2	0.993	1.865	(17,17)
5	1.0	410.5	0.899	1.837	(17,17)
4	1.0	373.1	0.817	1.716	(17,17)
17	0.8	417.4	0.915	1.753	(17,17)

TABLE 6.5 RESULTS OF THE PHASE-ONLY MATCHED FILTER WITH 17 QUANTIZATION LEVELS AND PHASE FACTOR OF 0.8

INPUT	MAX	MAX(rel.)	MAX/MAX2	Peak Location
P (zero phase)	417.4	1.0	1.753	(17,17)
P (random phase)	109.4	0.262	1.043	(16,17)
M (zero phase)	149.8	0.359	1.004	(31,17)

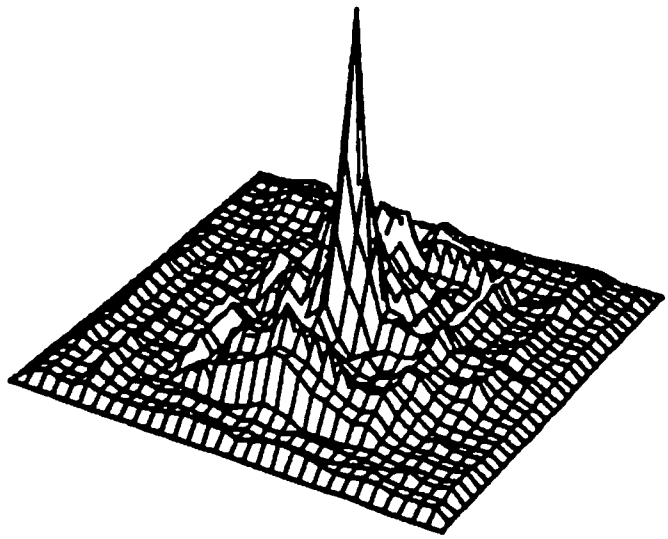

(a) 30% phase mismatch

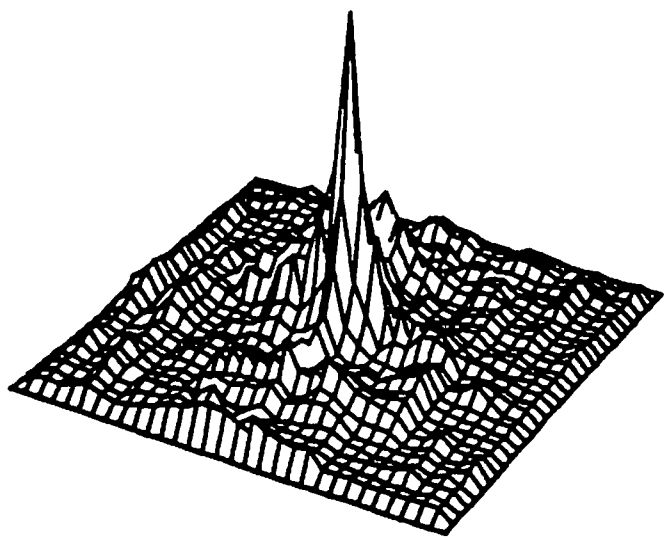

(b) four quantization levels

Fig. 6.8 Results of the phase-only matched filter with phase mismatch or quantization

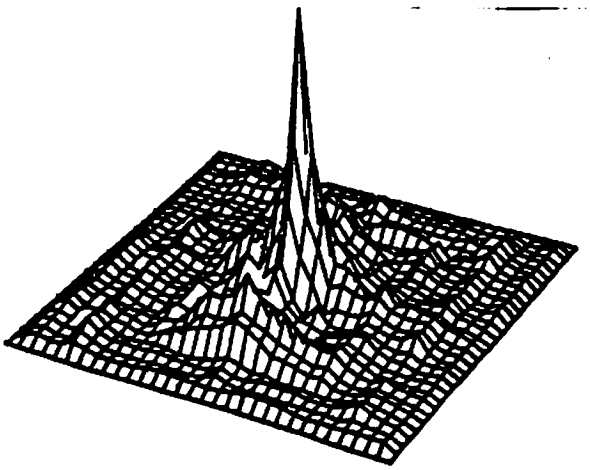

(a) P(zero phase)

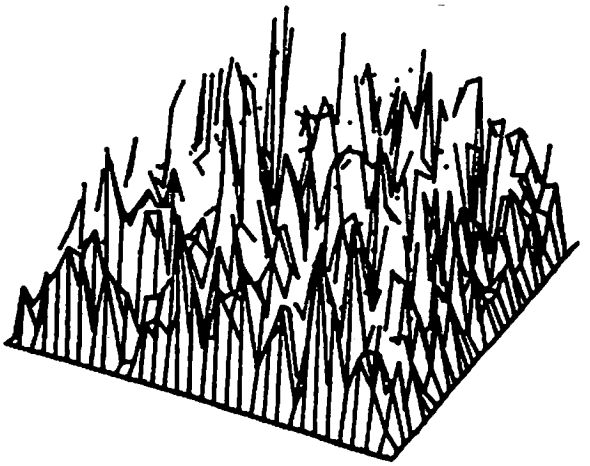

(b) P (random phase)

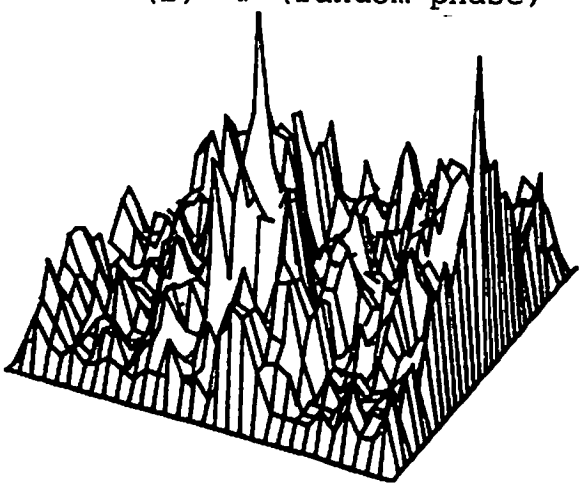

(c) M (zero phase)

Fig. 6.9 Results of the phase-only matched filter with 17 quantization levels and 20% phase mismatch

Table 6.5 shows the results of the phase-only matched filter with seventeen quantization levels and 20% phase mismatch when different inputs are applied. These results are comparable with those obtained from ideal phase-only matched filter shown in Fig. 6.6 and Table 6.2.

6.3.3 Filters for incoherent systems

As noted in Section 6.2.2, the matched filter used in the coherent system can also be used in an incoherent system. Furthermore we can take advantage of the freedom to choose the phase arbitrarily since only the intensity is of concern in the incoherent system. We can therefore apply phase coding to the desired object and make a matched filter according to Eq. (6-15) in order to increase the efficiency of the filter. When applying letters P and M to these filters we have the responses with shapes very similar to Figs. 6.5(a) and 6.5(c) and they are not repeated here. This happens because the input letters are binary (having only two grey levels) and the Fourier transforms of the amplitude and intensity are of the same form. Table 6.6 shows the results of incoherent matched filtering. The values are in units of irradiance. Table 6.7 is the result when phase coding is applied before the matched filter is made according to Eq. (6-15). Obviously the phase coding does improve the efficiency as indicated

TABLE 6.6 RESULTS OF THE MATCHED FILTER IN AN INCOHERENT SYSTEM

INPUT	MAX	MAX(rel.)	MAX/MAX2	Peak Location
P	626.3	1.0	1.185	(17,17)
M	298.2	0.476	1.0	(14,18)

TABLE 6.7 RESULTS OF THE MATCHED FILTER OBTAINED FROM EQ. (6-15) IN AN INCOHERENT SYSTEM

INPUT	MAX	MAX(rel.)	MAX/MAX2	Peak Location
P	10490	1.0	1.185	(17,17)
M	4992	0.476	1.014	(14,18)

TABLE 6.8 RESULTS OF THE PHASE-ONLY MATCHED FILTER IN AN INCOHERENT SYSTEM

INPUT	MAX	MAX(rel.)	MAX/MAX2	Peak Location
P	43750	1.0	1.012	(17,16)
M	28820	0.659	1.057	(13,16)

TABLE 6.9 RESULTS OF THE PHASE-ONLY MATCHED FILTER OBTAINED FROM EQ. (6-15) IN AN INCOHERENT SYSTEM

INPUT	MAX	MAX(rel.)	MAX/MAX2	Peak Location
P	73690	1.0	1.172	(17,17)
M	35940	0.488	1.002	(14,20)

by the peak values.

Since the matched filter for coherent systems can be applied to the incoherent system directly, the question arises as to whether or not the phase-only matched filter can be applied as well. Unfortunately, these results are not encouraging as shown in Fig. 6.10 and Table 6.8. The correct input can not even be located by the peak value. However the phase part of the matched filter obtained by phase coding the letter first (Eq. (6-15)) has been proved to be successful. This is not surprising because the letter has been phase coded and the reconstruction from the phase part of its Fourier transform should resemble the original letter. Again the responses are very similar to Figs. 6.5(a) and 6.5(c) in shape and are not shown here. Table 6.9 shows the measurement of the result. The efficiency is much improved with not much change in the appearance of the response.

We also tried to apply the phase-only matched filter idea to the incoherent system. This implies that we have a phase-only OTF. However the impulse response corresponding to this ideal phase-only OTF is not non-negative (or not even real) except for trivial cases and therefore the OTF does not exist. An iterative method similar to the input-output approach described in Chapter 2 has been used

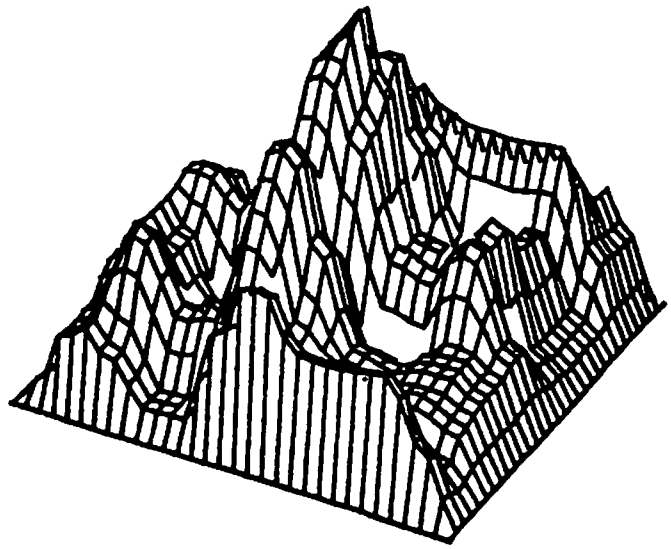

(a) P

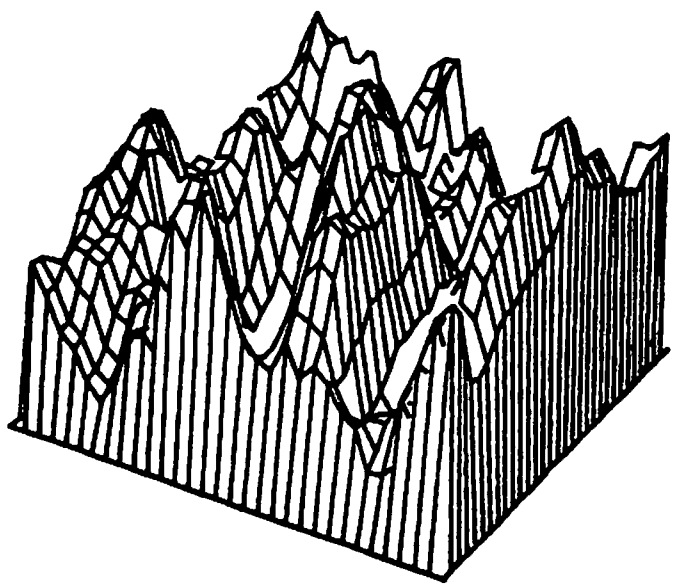

(b) M

Fig. 6.10 Results of the phase-only matched filter in an incoherent system with different inputs

to find a realizable OTF close to the ideal one. Unfortunately the best result we can get is still very similar to what we have for the matched filter. In fact this result is not surprising. Recall that the impulse response for incoherent system is non-negative and the OTF tends to have high dynamic range with most of the large components at low frequencies. However the phase-only OTF requires that the OTF be flat over the whole plane. These two goals conflict with each other. Therefore only a non-ideal filter can be obtained which may not perform well as we experienced in the simulation.

Finally we consider the effect of the speckle-like noise as discussed in Chapter 2. The two filters used here are the matched filter made by phase coding the letter first and the phase part of this filter. To include the effect of speckles we have embedded the 32x32 array in a 128x128 zero array. Table 6.10 summarizes the results. The shapes of the two responses look similar and only one of them is shown in Fig. 6.11. The shape resembles what we have obtained for the matched filter as shown in Fig. 6.5(a) except that it looks smoother. Comparing the peak values, the phase-only filter does better as we would expect. The values of MAX/MAX2 are all close to 1 which simply results from the fact that we are sampling more points and does not mean that the peaks are less sharp as

TABLE 6.10 THE EFFECT OF PHASE CODING ON THE INCOHERENT FILTERING

Filter	MAX	MAX/MAX2	Peak Location
Matched filter (phase coded)	37560	1.001	(66,67)
Phase only	263800	1.0	(66,66)

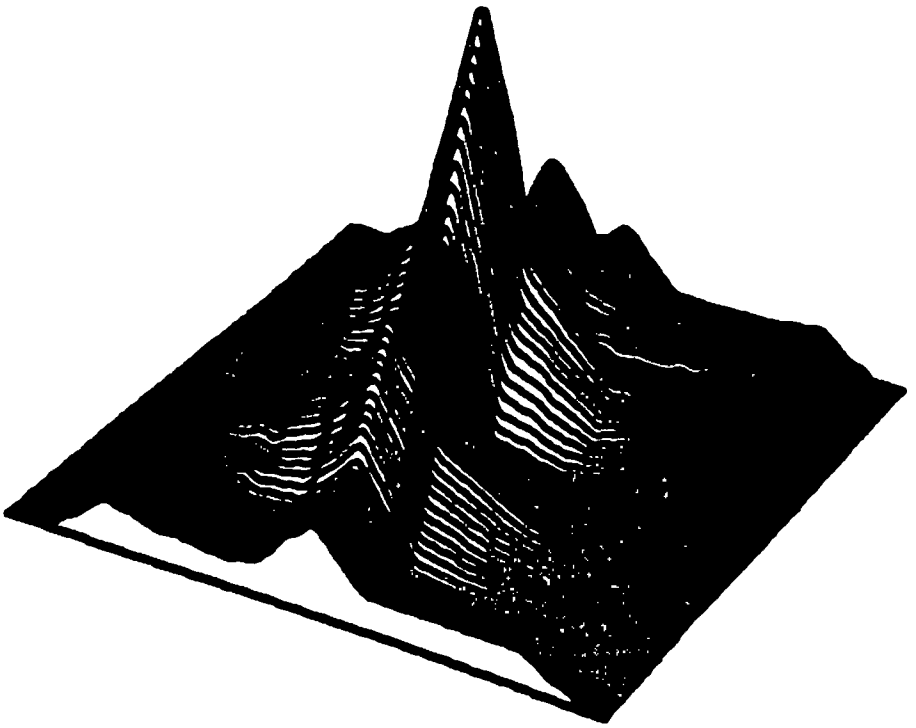

Fig. 6.11 The effect of phase coding on the incoherent filtering

we can see in Fig. 6.11. The correct response should appear at (65,65) which is the center of the 128x128 array. However both results of (66,67) and (66,66) are acceptable since the array has been expanded four times in each direction and the peak value appearing at $65-2 \leq x,y \leq 65+2$ is considered as correct. Therefore the phase coding does not affect the performance.

6.3.4 Conclusions

In this section we have examined the performance of different filters in the coherent character recognition system. The phase-only matched filter or its high-pass version are the best. Both have high efficiency and good selectivity. Quantization errors and phase mismatches introduced in making the filter do not affect the result significantly.

For incoherent filtering, the phase part of the matched filter obtained by phase coding the desired letter first does the best and the aliasing error caused by phase coding has little effect on the performance.

6.4 Experimental results

Instead of using the filtering set-up shown in Fig. 6.3, here we use a simpler system with the use of two lenses as shown in Fig. 6.12. The filter is located in the

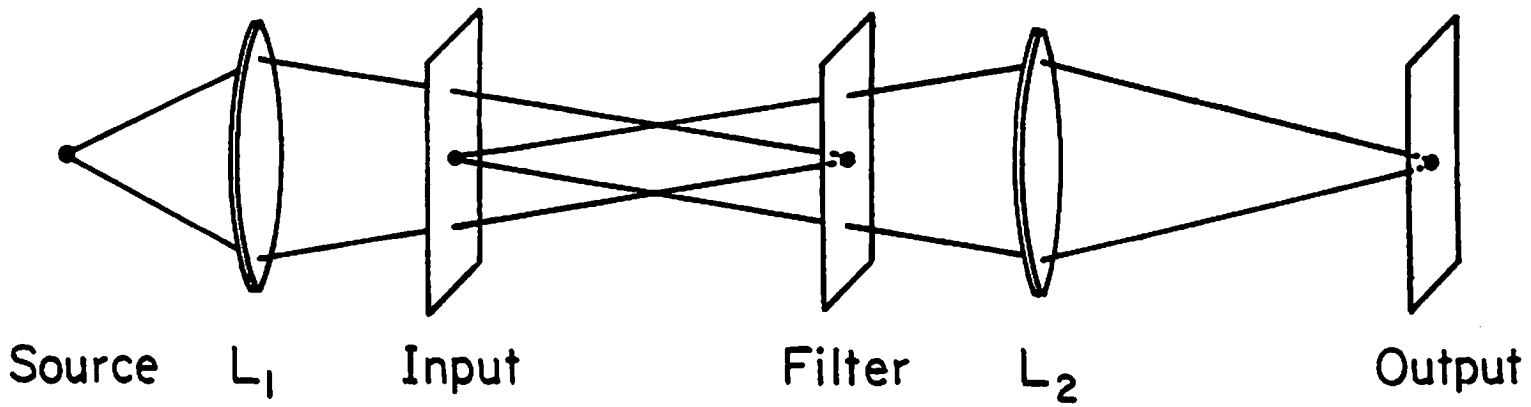

Fig. 6.12 Simplified filtering set-up

image plane of the point source and the input is imaged to the output plane by the second lens.

Figure 6.13 shows the input pattern which consists of different sizes of letters P and M. The phase-only matched filter corresponding to the second large P is put in the filter plane. Both the sampled filter and the continuous filter made on color film using the ROACH method are used. Figures 6.14 and 6.15 show the filtered result obtained from the sampled filter and the continuous filter respectively. The continuous filter tends to diffuse the outputs which correspond to incorrect inputs. This is a nice property since it reduces the possibility of false detection when a machine is used in reading these filtered outputs.

Besides the zero phase input letters, we also use phase coded letters as the input. Figure 6.16 shows the computer simulated kinoform reconstructions plotted on color film. Again a phase-only matched filter corresponding to the second large P is made which is the conjugate of the kinoform. Ideally this would give a perfect δ function response at the location corresponding to the second large P. The filtered results from the sampled filter and continuous filter are shown in Figs. 6.17 and 6.18 respectively. In Fig. 6.17 besides the

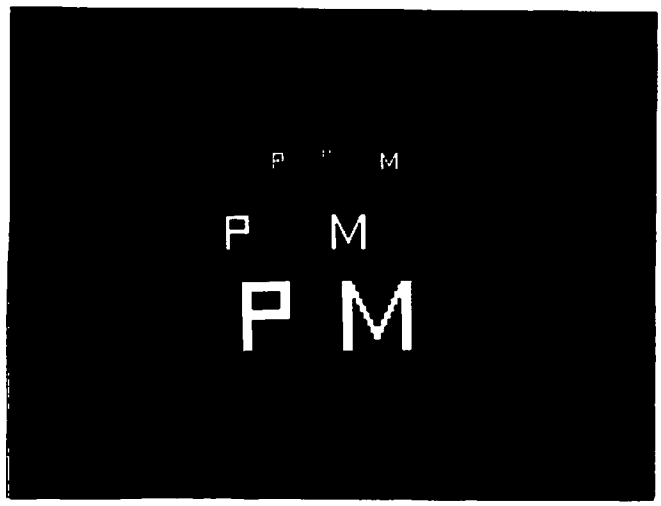

Fig. 6.13 Input pattern to the filtering system

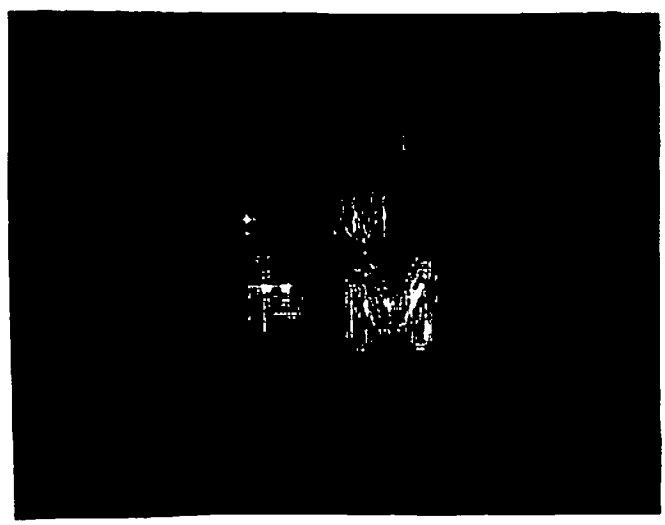

Fig. 6.14 Filtered result from the sampled filter

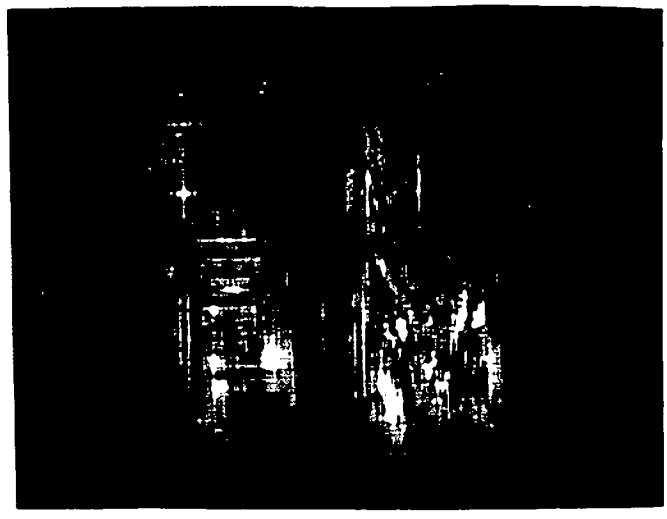

Fig. 6.15 Filtered result from the continuous filter

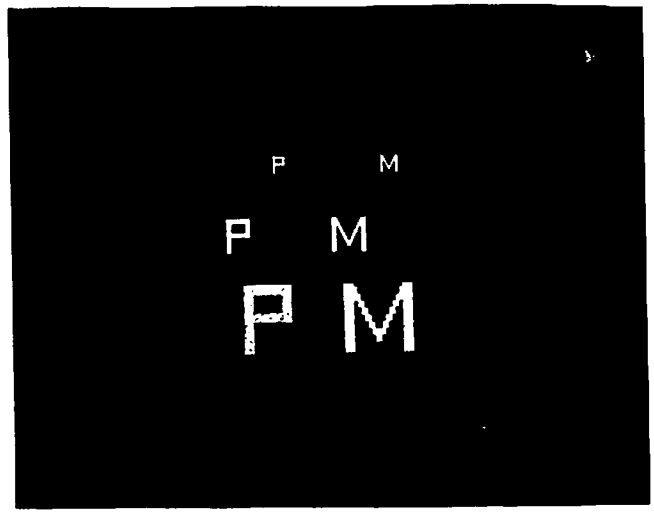

Fig. 6.16 Another input pattern to the filtering system (inputs are phase coded)

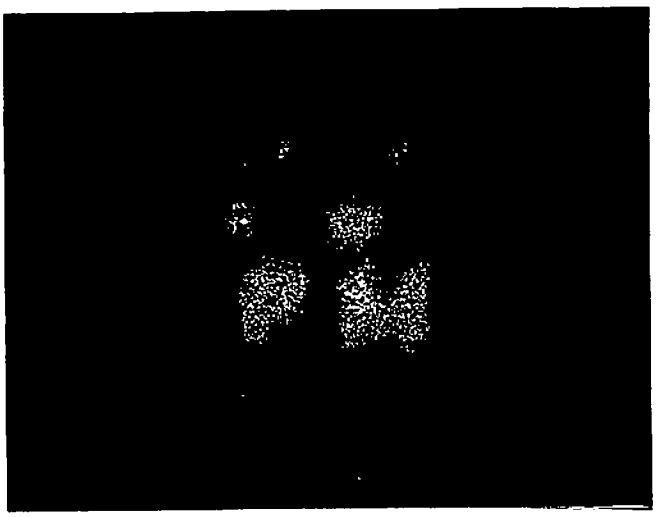

Fig. 6.17 Filtered result from the sample filter when phase coded objects are used

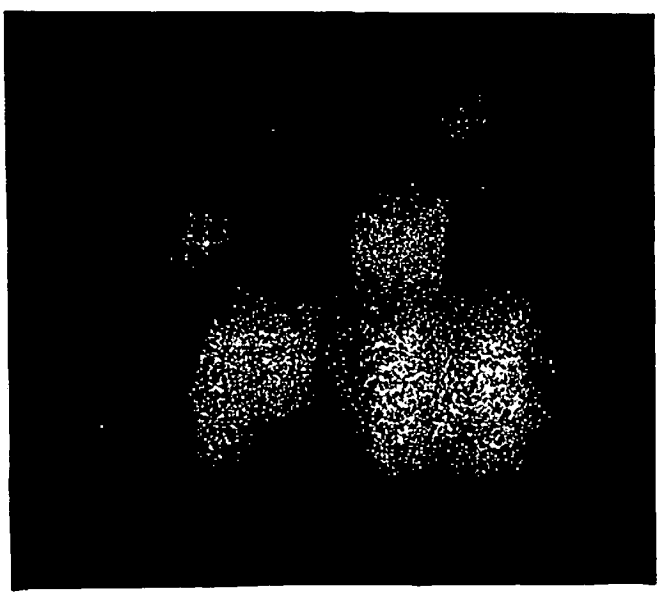

Fig. 6.18 Filtered result from the continuous filter when phase coded objects are used

central bright spot we also see two higher order spots due to the use of the sampled filter. Even though these two spots have a lower intensity and can be easily distinguished by eye, they may be detected as low intensity inputs when a machine is used to search for those isolated peaks. On the other hand these higher order spots are less visible in Fig. 6.18 when a continuous filter is used. The higher order problem shown here may not be very serious for character recognition, however, in other applications where the output is not just a bright spot, the problem may become serious and continuous filters are more suitable.

CHAPTER 7

SUMMARY AND CONCLUSIONS

In this work we have proposed several ways of making holograms that are suitable for a filtering system with a large input format.

Binary holograms have the advantages of easy fabrication and high signal-to-noise ratio. A new type of binary hologram called the double-phase hologram (DPH) is proposed. In one of the configurations, the hologram produces a reconstruction further away from the bright central spot and is more desirable than other binary holograms in a filtering system.

The on-axis hologram has its reconstruction at the zero order and has high light efficiency. It also uses the space-bandwidth product of the hologram more efficiently than the binary hologram. The higher orders are attenuated by a sinc function factor resulting from the finite cell size. These higher orders can be further reduced by a cell size expansion method without changing the resolution size. The higher orders can also be moved further away by

hologram interpolation with the DFT.

We also proposed a way of making a continuous hologram from two sampled patterns, one pattern for amplitude and one for phase control. These two patterns are low-pass filtered and recorded on the film separately by using different color illuminations. This hologram reconstructs a single order only. However due to the non-ideal interpolation, background noise and high order dots are present. In the ideal interpolation amplitude and phase are functions of both sampled amplitude and phase. Therefore it is believed that better results can be obtained by considering both amplitude and phase at the sampling points when either one of the binary patterns is made.

Phase coding methods are discussed with emphasis on the aliasing errors. It is found that a modified iterative phase coding method with constrained bandwidth can reduce the aliasing error considerably while maintaining good light efficiency. Further study of these methods applied to more complicated objects or even two-dimensional objects is of interest. The computer simulation is essential before any particular hologram is made for a filtering system.

For character recognition, a phase-only matched filter is found to be better than the traditional matched filter. The phase-only matched filters are implemented by means of a sampled kinoform and continuous kinoform. Although the high order spots are more visible in the output plane when the sampled filter is used, the problem is not very serious for character recognition. However in other applications where the output is not just a bright spot, the high order response may become serious and the continuous filters are more suitable. Applications of the continuous holograms to other filtering systems with the consideration of the inherent noise in the continuous hologram and the phase coding noise should be studied extensively in the future.

APPENDIX A

ON THE SHIFT PROPERTY OF THE FOURIER TRANSFORM

Let us consider the following Fourier transform pair $h(x) \Leftrightarrow H(u)$ where the two functions are related by

$$H(u) = \int_{-\infty}^{\infty} h(x) e^{-j2\pi ux} dx \quad . \tag{A-1}$$

We also define $H'(u) = H(u+\alpha)$, then

$$\begin{aligned} H'(u) = H(u+\alpha) &= \int_{-\infty}^{\infty} h(x) e^{-j2\pi (u+\alpha)x} dx \\ &= \int_{-\infty}^{\infty} [h(x) e^{-j2\pi\alpha x}] e^{-j2\pi ux} dx \end{aligned} \tag{A-2}$$

that is, $H(u+\alpha)$ can be obtained by evaluating the value of the Fourier transform of $h(x)e^{-j2\pi\alpha x}$ at the frequency u. Similarly, for the discrete case we have $h_n \Leftrightarrow H_k$ related by an N point DFT.

$$H_k = \frac{1}{\sqrt{N}} \sum_{n=0}^{N-1} h_n e^{-j2\pi kn/N} \quad . \tag{A-3}$$

Defining $H'_k = H_{k+\alpha}$, $0 \leq \alpha \leq 1$, we have

$$H'_k = H_{k+\alpha} = \frac{1}{\sqrt{N}} \sum_{n=0}^{N-1} h_n e^{-j2\pi(k+\alpha)n/N}$$

$$= \frac{1}{\sqrt{N}} \sum_{n=0}^{N-1} [h_n e^{-j2\pi\alpha n/N}] e^{-j2\pi kn/N} \quad . \tag{A-4}$$

Again this shows that $H_{k+\alpha}$ can be obtained by looking at the kth value of the DFT of $h_n e^{-j2\pi\alpha n/N}$. However, if we use this method to evaluate the interpolated values, then it turns out that the reconstruction is shifted around and also slightly off-axis. Let us go through the proof in Chapter 4 (Eqs. (4-29) through (4-40)) by using the result in Eqs. (A-4). Instead of Eq. (4-26) now we have

$$h_n^{(m)} = h_n e^{-j2\pi mn/MN} \tag{A-5}$$

Using the inverse transform relationship of Eq. (4-29) and Eq. (A-5), Eq. (4-32) becomes

$$Q_{pN+n'} = \sum_{m=0}^{M-1} \frac{1}{\sqrt{M}} h_{n'}^{(m)} e^{j2\pi mn'/MN} e^{j2\pi mp/M}$$

$$= \sum_{m=0}^{M-1} \frac{1}{\sqrt{M}} h_{n'} e^{-j2\pi mn'/MN} e^{j2\pi mn'/MN} e^{j2\pi mp/M} \tag{A-6}$$

$$= \frac{1}{\sqrt{M}} h_{n'} \sum_{m=0}^{M-1} e^{j2\pi mp/M} \quad .$$

Using the result of Eqs. (4-36)-(4-38), we get

$$Q_{pN+n'} = \begin{cases} \sqrt{M}h_{n'} & p = 0 \\ 0 & p = 1,2,\ldots,M-1. \end{cases} \qquad (A-7)$$

Therefore instead of getting the results shown in Fig. 4.8 we have a wrong result shown in Fig. A.1. The reconstruction is shifted around and also slightly off-axis.

In fact the result in Fig. A.1 can be fixed by shifting the impulse response around and moving it to the center. If we work backwards, we can obtain the correct procedure given by Eqs. (4-26)-(4-28).

The new inputs $h_n^{(m)}$ for $m = 0,\ldots,M-1$ are given by Eq. (4-26)

$$h_n^{(m)} = h_n e^{-j2\pi m[(n+N/2)_{ModN}-N/2]/MN} \quad . \qquad (4-26)$$

This is obtained by multiplying the original impulse response shown in Fig. 4.7(a) with

$$e^{-j2\pi mn/MN} \qquad n = -\frac{N}{2},\ldots,0,\ldots,\frac{N}{2}-1 \qquad (4-25)$$

then shifted by half period.

To show that this new sequence can be expressed by Eq. (4-26), we start with Eq. (4-26) and show that it is equivalent to the new sequence. For $n = 0,\ldots,\frac{N}{2}-1$, Eq. (4-26) becomes

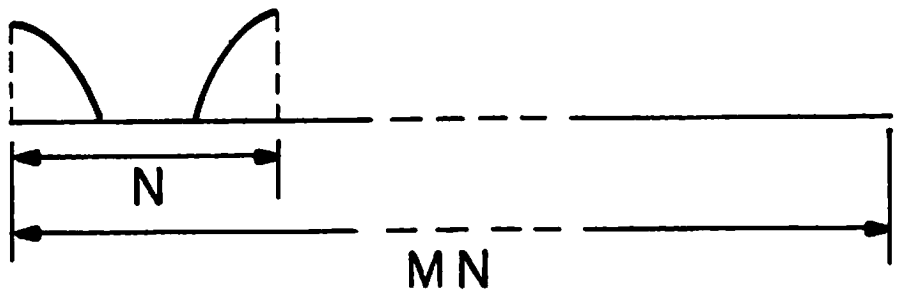

(a) output sequences Q_n, n=0,...,MN-1, when linear phase is used

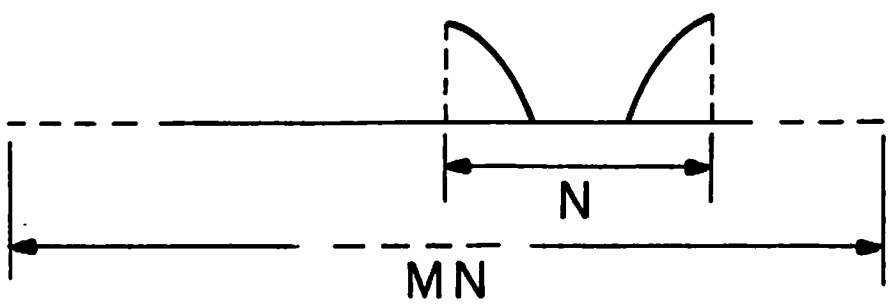

(b) Reconstruction

Fig. A.1 Results of DFT interpolation when using Eq.(A-4)

$$h_n^{(m)} = h_n e^{-j2\pi m(n+N/2-N/2)/MN}$$
$$= h_n e^{-j2\pi mn/MN} \quad . \tag{A-8}$$

This is exactly what we would have from Eq. (4-25). For $n = \frac{N}{2},\ldots,N-1$ we have

$$h_n^{(m)} = h_n e^{-j2\pi m(n+N/2-N-N/2)/MN}$$
$$= h_n e^{-j2\pi m(n-N)/MN} \quad . \tag{A-9}$$

If we redefine $n' = n-N$, $h_{n'}' = h_{n'+N}$, and $h_{n'}'^{(m)} = h_{n'+N}^{(m)}$ then Eq. (A-9) becomes

$$h_{n'}'^{(m)} = h_{n'}' e^{-j2\pi mn'/MN} \quad . \tag{A-10}$$

Note that n' is negative and Eq. (A-10) is what we would obtain from Eq. (4-25).

This result shows that the correct procedure resembles the shift property of continuous Fourier transform (Eq. (A-2)) rather than the DFT (Eq. (A-4)).

APPENDIX B

COMPARISONS OF DIFFERENT FILTERS FOR CHARACTER RECOGNITION

The matched filter, phase-only matched filter and inverse filter will be compared in terms of the peak value and the sharpness of the peak when the input is matched.

Referring to Fig. 6.3, let s(x,y) be the input with its Fourier transform S(u,v) and H(u,v) be the filter. The output is given by

$$\alpha(x,y) = \int\int_{-\infty}^{\infty} S(u,v)H(u,v)e^{j2\pi(ux+vy)}dudv \quad . \qquad (B\text{-}1)$$

Due to physical limitations of the material, the filter can only have a maximum transmittance value t, where $0 \leq t \leq 1$. Given that S(u,v) has a maximum absolute value S_{max} and a minimum absolute value S_{min}, the matched filler is given by

$$H_1(u,v) = t\,\frac{S^*(u,v)}{S_{max}} \qquad (B\text{-}2)$$

since the maximum transmittance value is t. The peak value (also the center value) in the output is found to be

$$\alpha_1(0,0) = \iint_{-\infty}^{\infty} S(u,v) \cdot t \frac{S^*(u,v)}{S_{max}} \, dudv$$

$$= t \iint_{-\infty}^{\infty} \frac{|S(u,v)|^2}{S_{max}} \, dudv \quad . \tag{B-3}$$

For the phase-only matched filter we have filter

$$H_2(u,v) = t \frac{S^*(u,v)}{|S(u,v)|} \tag{B-4}$$

and the peak value is given by

$$\alpha_2(0,0) = \iint_{-\infty}^{\infty} S(u,v) \cdot t \frac{S^*(u,v)}{|S(u,v)|} \, dudv$$

$$= t \iint_{-\infty}^{\infty} |S(u,v)| dudv \quad . \tag{B-5}$$

Finally for the inverse filter we have

$$H_3(u,v) = t \frac{\frac{1}{S(u,v)}}{\left|\frac{1}{S(u,v)}\right|_{max}} = t \frac{S_{min}}{S(u,v)} \tag{B-6}$$

and

$$\alpha_3(0,0) = \iint_{-\infty}^{\infty} S(u,v) \cdot t \frac{S_{min}}{S(u,v)} \, dudv$$

$$= t \iint_{-\infty}^{\infty} S_{min} dudv \tag{B-7}$$

Since $S_{max} \geq |S(u,v)|$ we have from Eqs. (B-3) and (B-5) that

$$\alpha_2(0,0) \geq \alpha_1(0,0) \tag{B-8}$$

Comparing Eqs. (B-5) and (B-7) we also have

$$\alpha_2(0,0) \geq \alpha_3(0,0) \tag{B-9}$$

since $|S(u,v)| \geq S_{min}$. Therefore the phase-only matched filter has better efficiency than either the matched filter or the inverse filter.

We also compare the sharpness of the peak. It is known that the inverse filter produces a δ function in the output plane and is the best in sharpness. However the inverse filter is sensitive to the noise and has low light efficiency as we have shown above. We will prove in the following that the phase-only matched filter gives a sharper peak than the matched filter. In addition to the better light efficiency, this will make the phase-only matched filter more preferable.

The outputs due to the matched filter and the phase-only matched filter are given by

$$\alpha_1(x,y) = t \iint_{-\infty}^{\infty} \frac{|S(u,v)|^2}{S_{max}} e^{j2\pi(ux+vy)} dudv$$

$$= t\, S_{max} \iint_{-\infty}^{\infty} \frac{|S(u,v)|^2}{S^2_{max}} e^{j2\pi(ux+vy)}\, dudv \quad \text{(B-10)}$$

and

$$\alpha_2(x,y) = t \iint_{-\infty}^{\infty} |S(u,v)|\, e^{j2\pi(ux+vy)} dudv$$

$$= t\, S_{max} \iint_{-\infty}^{\infty} \frac{|S(u,v)|}{S_{max}} e^{j2\pi(ux+vy)} dudv \quad . \text{(B-11)}$$

To simplify the proof we will consider α_1 and α_2 as one-dimensional functions. Since tS_{max} is the common factor, we can drop it and also redefine $|S(u)|$ as a normalized quantity to get

$$\alpha_1(x) = \int_{-\infty}^{\infty} |S(u)|^2 e^{j2\pi ux} du \quad \text{(B-12)}$$

and

$$\alpha_2(x) = \int_{-\infty}^{\infty} |S(u)| e^{j2\pi ux} du \quad \text{(B-13)}$$

with $0 \leq |S(u)| \leq 1$. Since the quantity to be measured is intensity we will define

$$I_1(x) = |\alpha_1(x)|^2 \quad \text{(B-14)}$$

and

$$I_2(x) = |\alpha_2(x)|^2 \tag{B-15}$$

and compare the sharpness of $I_1(x)$ and $I_2(x)$ at the center ($x = 0$). $I_1(x)$ can be expressed explicitly as

$$\begin{aligned} I_1(x) &= \alpha_1(x) \cdot \alpha_1^*(x) \\ &= \int_{\infty}^{\infty} |S(u_1)|^2 e^{j2\pi u_1 x} du_1 \int_{\infty}^{\infty} |S(u_2)|^2 e^{-j2\pi u_2 x} du_2 . \end{aligned} \tag{B-16}$$

The first derivative of $I_1(x)$ is given by

$$\begin{aligned} I_1'(x) = j2\pi &\int_{\infty}^{\infty} u_1 |S(u_1)|^2 e^{j2\pi u_1 x} du_1 \int_{\infty}^{\infty} |S(u_2)|^2 e^{-j2\pi u_2 x} du_2 \\ -j2\pi &\int_{\infty}^{\infty} u_2 |S(u_2)|^2 e^{-j2\pi u_2 x} du_2 \\ &\int_{\infty}^{\infty} |S(u_1)|^2 e^{j2\pi u_1 x} du_1 \end{aligned} \tag{B-17}$$

and

$$I_1'(0) = 0 \quad . \tag{B-18}$$

The second derivative of $I_1(x)$ is found to be

$$I_1''(x) = -4\pi^2 \int_{-\infty}^{\infty} u_1^2 |S(u_1)|^2 e^{j2\pi u_1 x} du_1 \int_{-\infty}^{\infty} |S(u_2)|^2 e^{-j2\pi u_2 x} du_2$$

$$-4\pi^2 \int_{-\infty}^{\infty} u_2^2 |S(u_2)|^2 e^{-j2\pi u_2 x} du_2 \int_{-\infty}^{\infty} |S(u_1)|^2 \qquad \text{(B-19)}$$

$$e^{j2\pi u_1 x} du_1$$

$$+8\pi^2 \int_{-\infty}^{\infty} u_1 |S(u_1)|^2 e^{j2\pi u_1 x} du_1 \int_{-\infty}^{\infty} u_2 |S(u_2)|^2 e^{-j2\pi u_2 x} du_2$$

with

$$I_1''(0) = -8\pi^2 \int_{-\infty}^{\infty} u_1^2 |S(u_1)|^2 du_1 \int_{-\infty}^{\infty} |S(u_2)|^2 du_2$$

$$+8\pi^2 \left[\int_{-\infty}^{\infty} u_1 |S(u_1)|^2 du_1\right]^2 \quad . \qquad \text{(B-20)}$$

We want to show that

$$\int_{-\infty}^{\infty} u_1 |S(u_1)|^2 du_1 = 0 \qquad \text{(B-21)}$$

To show this let us consider the first derivative of $\alpha_1(x)$

$$\alpha_1'(x) = j2\pi \int_{-\infty}^{\infty} u |S(u)|^2 e^{j2\pi u x} du \qquad \text{(B-22)}$$

and

$$\alpha_1'(0) = j2\pi \int_{-\infty}^{\infty} u |S(u)|^2 du \quad . \qquad \text{(B-23)}$$

If s(x) is real then S(u) is conjugate symmetric and $|S(u)|$, $|S(u)|^2$ are symmetric functions. We then conclude that Eq. (B-21) holds. However it is less obvious when s(x) is not real. However it is clear from Eq. (B-12) that $\alpha_1(x)$ has maximum at x = 0. Therefore the first derivative $\alpha_1'(x)$ at x = 0 is either zero or does not exist. Assuming that the first derivative exists at x = 0 then we have $\alpha_1'(0) = 0$ and Eq. (B-21) follows. Therefore we have from Eq. (B-20) that

$$I_1''(0) = -8\pi^2 \int_{-\infty}^{\infty} u_1^2 |S(u_1)|^2 du_1 \int_{-\infty}^{\infty} |S(u_2)|^2 du_2 < 0 \quad . \text{(B-24)}$$

From this result and Eq. (B-18) we conclude that $I_1(x)$ has a maximum at x =0. In fact this conclusion can be easily obtained by considering Eq. (B-16). However the absolute value of $I_1''(0)$ gives another measurement of the sharpness of the peak and we have

$$|I_1''(0)| = 8\pi^2 \int_{-\infty}^{\infty} u_1^2 |S(u_1)|^2 du_1 \int_{-\infty}^{\infty} |S(u_2)|^2 du_2 \quad \text{(B-25)}$$

Replacing $|S(u_i)|^2$ by $|S(u_i)|$ in Eq. (B-16) where i = 1,2, and going through the same derivation we have a similar result with

$$|I_2''(0)| = 8\pi^2 \int_{-\infty}^{\infty} u_1^2 |S(u_1)|\, du_1 \int_{-\infty}^{\infty} |S(u_2)|\, du_2 \quad . \qquad \text{(B-26)}$$

Since $0 \leq |S(u)| \leq 1$ we conclude that

$$|S(u)| \geq |S(u)|^2 \qquad \text{(B-27)}$$

and therefore

$$|I_2''(0)| \geq |I_1''(0)| \qquad \text{(B-28)}$$

This shows that the phase-only matched filter gives a sharper peak in the output and is easier to detect. Comparing both the peak value and the sharpness of the peak, we then conclude that the phase-only matched filter has the best performance.

REFERENCES

[1-1] Special issue on Optical Computing, Proc. IEEE, Vol. 65, 1977.

[1-2] D. Casasent, "A Hybrid Image Processor," Optical Engineering, Vol. 13, pp. 228-234, 1974.

[1-3] S.R. Dashiell and A.A. Sawchuk, "Nonlinear Optical Processing: Analysis and Synthesis," Applied Optics, Vol. 16, pp. 1009-1025, 1977.

[1-4] A. Armand, "Real-Time Nonlinear Optical Information Processing," Ph.D. Dissertation, EE Department, USC, 1979.

[1-5] T.C. Strand and A.A. Sawchuk, "Space-Variant Processing with Polychromatic Light," Proceedings of ICO-11 Conference, Madrid, Spain, 1978, pp. 269-272.

[1-6] J.J. Burch, "A Computer Algorithm for the Synthesis of Spatial Frequency Filters," Proc. IEEE, Vol. 55, pp. 599-601, 1967.

[1-7] T.S. Huang and B. Prasada, "Considerations on the Generation and Processing of Holograms by Digital Computers," MIT Res. Lab. of Electr., Quart. Prog. Rep., No. 91, pp. 189-205, 1966.

[1-8] B.R. Brown and A.W Lohmann, "Complex Spatial Filtering with Binary Marks," Applied Optics, Vol. 5, pp. 967-969, 1966.

[1-9] A.W. Lohmann and D.P. Paris, "Binary Fraunhofer Holograms, Generated by Computer," Applied Optics, Vol. 6, pp. 1739-1748, 1967.

[1-10] W.H. Lee, "Sampled Fourier Transform Hologram Generated by Computer," Applied Optics, Vol. 9, pp. 639-643, 10970.

[1-11] C.B. Burckhardt, "A Simplification of Lee's Method of Generating Holograms by Computer," Applied Optics, Vol. 9, p. 1949, 1970.

[1-12] P. Chavel and J.P. Hugonin, "High Quality Computer Holograms: The Problem of Phase Representation," J. Opt. Soc. Am., Vol. 66, pp. 989-996, 1976.

[1-13] R.E. Haskell and B.C. Culver, "New Coding Technique for Computer Generated Holograms," Applied Optics, Vol. 11, pp. 2712-2714, 1972.

[1-14] R.E. Haskell, "Computer-Generated Holograms with Minimum Quantization," J. Opt. Soc. Am., Vol. 63, p. 504, 1973.

[1-15] J.P. Allebach and J.J. Keegan, "Computer Synthesis of Binary Fourier Transform Holograms Using Ordered Dither," J. Opt. Soc. Am., Vol. 68, p. 1440, 1978.

[1-16] L.B. Lesem, P.M. Hirsch and J.A. Jordan, Jr., "The Kinoform: A New Wavefront Reconstruction Device," IBM J. Res. Develop., Vol. 13, pp. 150-155, 1969.

[1-17] D. Kermisch, "Image Reconstruction from Phase Information Only," J. Opt. Soc. Am., Vol. 60, pp. 15-17, 1970.

[1-18] D.C. Chu and J.W. Goodman, "Spectrum Shaping with Parity Sequences," Applied Optics, Vol. 11, pp. 1716-1724, 1972.

[1-19] D.C. Chu and J.R. Fienup, "Recent Approaches to Computer Generated Holograms," Optical Engineering, Vol. 13, pp 189-195, 1974.

[1-20] D.C. Chu, J.R. Fienup and J.W. Goodman, "Multiemulsion On-Axis Computer Generated Hologram," Applied Optics, Vol. 12, pp. 1386-1388, 1973.

[1-21] L.B. Lesem, P.M. Hirsch and J.A. Jordan, Jr., "Computer Synthesis of Holograms for 3-D Display," Comm. of the ACM, Vol. 11, pp. 661-674, 1968.

[1-22] B.R. Brown and A.W. Lohmann, "Computer-Generated Binary Holograms," IBM J. Res. Develop., Vol. 13, pp. 160-168, 1969.

[1-23] J.R. Fienup and J.W. Goodman, "New Ways to Make Computer-Generated Color Holograms," Nouv. Rev. Optique, Vol. 5, pp. 269-275, 1974.

[1-24] A.J. MacGovern and J.C. Wyant, "Computer-Generated Holograms for Testing Optical Elements," Applied Optics, Vol. 10, pp. 619-624, 1971.

[1-25] T.S. Huang, "Digital Holography," Proc. IEEE, Vol. 59, pp. 1335-1346, 1971.

[1-26] A.W. Lohmann, D.P. Paris, and H.W. Werlich, "A Computer Generated Spatial Filter, Applied to Code Translation," Applied Optics, Vol. 6, pp. 1139-1140, 1967.

[1-27] M. Severcan, "Computer Generation of Coherent Optical Filters with High Light Efficiency and Large Dynamic Range," Ph.D. Dissertation, EE Department, Stanford University, 1973.

[1-28] A. Kozma, W.H. Lee, and P.J. Peters, "Holographic Recording and Retrieval System," IEEE/OSA Conference on Laser Engineering and Applications, 1971.

[1-29] J.R. Fienup, "Improved Synthesis and Computational Methods for Computer-Generated Holograms," Ph.D. Dissertation, EE Department, Stanford University, 1975.

[1-30] J.W. Goodman, Introduction to Fourier Optics, McGraw-Hill, New York, 1968, pp. 177-184.

[1-31] S. Lowenthal and P. Chavel, "Reduction of the Number of Samples in Computer Holograms for Image Processing," Applied Optics, Vol. 13, pp. 718-720, 1974.

[1-32] W.H. Lee and M.O. Greer, "Matched Filter Optical Processor," Applied Optics, Vol. 13, pp. 925-930, 1974.

[1-33] H. Bartelt, W.J. Dallas and A.W. Lohmann, "Computer Generated Spatial Filters for Large Object Formats," Optics Communications, Vol. 20, pp. 50-55, 1977.

[1-34] T. Yatagai, "Interpolation Method of Computer-Generated Filters for Large Object Formats," Optics Communications, Vol. 23, pp. 347-351, 1977.

[1-35] J.P. Allebach, N.C. Gallagher, and B. Liu, "Aliasing Error in Digital Holograhy," Applied Optics, Vol. 15, pp. 2183-2188, 1976.

[1-36] W.J. Dallas, "Deterministic Diffusers for Holography," Applied Optics, Vol. 12, pp. 1179-1187, 1973.

[1-37] N.C. Gallagher and B. Liu, "Method for Computing Kinoforms that Reduces Image Reconstruction Error," Applied Optics, Vol. 12, pp. 2328-2335, 1973.

[1-38] C.K. Hsueh and A.A. Sawchuk, "Computer-Generated Double-Phase Holograms," Applied Optics, Vol. 17, pp. 3874-3883, 1978.

[2-1] J.P. Allebach, N.C. Gallagher, and B. Liu, "Aliasing Error in Digital Holography," Applied Optics, Vol. 15, pp. 2183-2188, 1976.

[2-2] E.N. Leith and J. Upatnieks, "Wavefront Reconstruction with Diffused Illumination and Three-Dimensional Objects," J. Opt. Soc. Am., Vol. 54, pp. 1295-1301, 1964.

[2-3] C.B. Burckhardt, "Use of a Random Phase Mask for the Recording of Fourier Transform Holograms of Data Masks," Applied Optics, Vol. 9, pp. 695-700, 1970.

[2-4] W.J. Dallas, "Deterministic Diffusers for Holography," Applied Optics, Vol. 12, pp. 1179-1187, 1973.

[2-5] J.R. Fienup, "Checkerboard Real-Imaginary Phase Code," J. Opt. Soc. Am., Vol. 68, p. 1444, 1978.

[2-6] P.M. Hirsch, J.A. Jordan, and L.B. Lesem, U.S. Patent No. 3,619,022, 1971.

[2-7] N.C. Gallagher and B. Liu, "Method for Computing Kinoforms that Reduces Image Reconstruction Error," Applied Optics, Vol. 12, pp. 2328-2335, 1973.

[2-8] R.W. Gerchberg and W.O. Saxton, "A Practical Algorithm for the Determination of Phase from Image and Diffraction Plane Pictures," Optik, Vol. 35, p. 237-246, 1972.

[2-9] J.R. Fienup, "Improved Synthesis and Computational Methods for Computer-Generated Holograms," Ph.D. Dissertation, EE Department, Stanford University, 1975.

[2-10] J.R. Fienup, "Reduction of Quantization Noise in Kinoforms and Computer-Generated Holograms," J. Opt. Soc. Am., Vol. 64, p. 1395, 1974.

[2-11] J.R. Fienup, "Reconstruction of an Object from the Modulus of its Fourier Transform," Optics Letters, Vol. 3, pp. 27-29, 1978.

[2-12] J.P. Allebach and B. Liu, "Minimax Spectrum Shaping with a Bandwidth Constraint," Applied Optics, Vol. 4, pp. 3062-3072, 1975.

[2-13] R.A. Gonsalves, "Phase Retrieval from Modulus Data," J. Opt. Soc. Am., Vol. 66, pp. 961-964, 1976.

[2-14] A. Labeyrie, "Attainment of Diffraction Limited Resolution in Large Telescopes by Fourier Analysing Speckle Patterns in Star Images," Astron. & Astrophys., Vol. 6, pp. 85-87, 1970.

[2-15] B. Liu and N.C. Gallagher, "Convergence of a Spectrum Shaping Algorithm," Applied Optics, Vol. 13, pp. 2470-2471, 1974.

[2-16] N.C. Gallagher and D.W. Sweeney, "Infrared Holographic Optical Elements with Applications to Laser Material Processing," to appear in IEEE Journal of Quantum Electronics, December 1979.

[2-17] D.G. Luenberger, Introduction to Linear and Nonlinear Programming, Addison-Wesley, Reading, Mass., 1973.

[2-18] C.K. Hsueh and A.A. Sawchuk, "Computer-Generated Double-Phase Holograms," Applied Optics, Vol. 17, pp. 3874-3883, 1978.

[2-19] N.C. Gallagher and B. Liu, "Statistical Properties of the Fourier Transform of Random Phase Diffusers," Optik, Vol. 42, pp. 65-86, 1975.

[2-20] H.S. Hou and H.C. Andrews, "Least Squares Image Restoration using Spline Basis Functions," IEEE Trans. Comput., Vol. C-26, pp. 856-873, 1977.

[2-21] H.S. Hou and H.C. Andrews, "Cubic Splines for Image Interpolation and Digital Filtering," IEEE Trans. Acoust., Speech, Signal Processing, Vol. ASSP-26, pp. 508-517, 1978.

[2-22] M.J. Peyrovian, "Image Restoration by Spline Functions," Ph.D. Dissertation, EE Department, USC, 1976.

[2-23] R.T. Gregory and D.L. Karney, A Collection of Matrices for Testing Computational Algorithms, John Wiley, p. 48, 1969.

[2-24] B.R. Hunt, "A Matrix Theory Proof of the Discrete Convolution Theorem," IEEE Trans. Audio and Electroacoustics, Vol. AU-19, pp. 285-288, 1971.

[3-1] N.C. Gallagher, Jr., et al., "Binary Phase Digital Reflection Holograms: Fabrication and Potential Applications," Applied Optics, Vol. 16, pp. 413-417, 1977.

[3-2] B.R. Brown and A.W. Lohmann, "Complex Spatial Filtering with Binary Masks," Applied Optics, Vol. 5, pp. 967-969, 1966.

[3-3] A.W. Lohmann and D.P. Paris, "Binary Fraunhofer Holograms, Generated by Computer," Applied Optics, Vol. 6, pp. 1739-1748, 1967.

[3-4] W.H. Lee, "Sampled Fourier Transform Hologram Generated by Computer," Applied Optics, Vol. 9, pp. 639-643, 1970.

[3-5] C.B. Burckhardt, "A Simplification of Lee's Method of Generating Holograms by Computer," Applied Optics, Vol. 9, p. 1949, 1970.

[3-6] T.S. Huang, "Digital Holography," Proc. IEEE, Vol. 59, pp. 1335-1346, 1971.

[3-7] J.W. Goodman, Introduction to Fourier Optics, McGraw-Hill, New York, 1968.

[3-8] C.K. Hsueh and A.A. Sawchuk, "Computer-Generated Double-Phase Holograms," Applied Optics, Vol. 17, pp. 3874-3883, 1978.

[3-9] R.E. Haskell and B.C. Culver, "New Coding Technique for Computer Generated Holograms," Applied Optics, Vol. 11, pp. 2712-2714, 1972.

[3-10] M. Severcan, "Computer Generation of Coherent Optical Filters with High Light Efficiency and Large Dynamic Range," Ph.D. Dissertation, EE Department, Stanford University, 1973.

[3-11] D.C. Chu and J.W. Goodman, "Spectrum Shaping with Parity Sequences," Applied Optics, Vol. 11, pp. 1716-1724, 1972.

[3-12] D.C. Chu and J.R. Fienup, "Recent Approaches to Computer Generated Holograms," Optical Engineering, Vol. 13, pp. 189-195, 1974.

[3-13] E.K. Shmarev, "Kinoform in Filtering and Image-Synthesis Systems," Opt. Spectrosc., Vol. 41, pp. 535-536, 1976.

[3-14] J. Bucklew and N. Gallagher, Jr., "Detour Phase Error in the Lohmann Hologram," Applied Optics, Vol. 18, pp. 575-580, 1979.

[3-15] J. Bucklew and N.C. Gallagher, Jr., "Comprehensive Error Models and A Comparative Study of Some Detour-Phase Holograms," Applied Optics, Vol. 18, pp. 2861-2869, 1979.

[3-16] D. Kermisch, "Image Reconstruction from Phase Information Only," J. Opt.Soc. Am., Vol. 60, pp. 15-17, 1970.

[3-17] N.C. Gallagher, Jr., "Optimum Quantization in Digital Holography," Applied Optics, Vol. 17, pp. 109-115, 1978.

[3-18] B.R. Brown and A.W. Lohmann, "Computer-Generated Binary Holograms," IBM J. Res. Develop., Vol. 13, pp. 160-168, 1969.

[3-19] P. Chavel and J.P. Hugonin, "High Quality Computer Holograms: The Problem of Phase Representation," J. Opt. Soc. Am., Vol. 66, pp. 989-996, 1976.

[4-1] L.B. Lesem, P.M. Hirsch and J.A. Jordan, Jr., "The Kinoform: A New Wavefront Reconstruction Device," IBM J. Res. Develop., Vol. 13, pp. 150-155, 1969.

[4-2] J.R. Fienup, "Improved Synthesis and Computational Methods for Computer-Generated Holograms," Ph.D. Dissertation, EE Department, Stanford University, 1975.

[4-3] W.J. Dallas, "Deterministic Diffusers for Holography," Applied Optics, Vol. 12, pp. 1179-1187, 1973.

[4-4] N.C. Gallagher and B. Liu, "Method for Computing Kinoforms that Reduces Image Reconstruction Error," Applied Optics, Vol. 12, pp. 2328-2335, 1973.

[4-5] S. Lowenthal and P. Chavel, "Reduction of the Number of Samples in Computer Holograms for Image Processing," Applied Optics, Vol. 13, pp. 718-720, 1974.

[4-6] P. Chavel and S. Lowenthal, "A Method of Incoherent Optical-Image Processing Using Synthetic Holograms," J. Opt. Soc. Am., Vol. 66, pp. 14-23, 1976.

[4-7] H. Bartelt, W.J. Dallas and A.W. Lohmann, "Computer Generated Spatial Filters for Large Object Formats," Optics Communications, Vol. 20, pp. 50-55, 1977.

[4-8] P. Chavel and J.P. Hugonin, "High Quality Computer Holograms: The Problem of Phase Representation," J. Opt. Soc. Am., Vol. 66, pp. 989-996, 1976.

[4-9] T. Yatagai, "Interpolation Method of Computer-Generated Filters for Large Object Formats," Optics Communicatons, Vol. 23, pp. 347-351, 1977.

[4-10] W.T. Cochran, et al., "What is the Fast Fourier Transform?" IEEE Trans. Audio, Vol. 15, pp. 45-55, 1967.

[5-1] J.R. Fienup, "Improved Synthesis and Computational Methods for Computer-Generated Holograms," Ph.D. Dissertation, EE Department, Stanford University, 1975.

[5-2] L.B. Lesem, P.M. Hirsch and J.A. Jordan, Jr., "The Kinoform: A New Wavefront Reconstruction Device," IBM J. Res. Develop., Vol. 13, pp. 150-155, 1969.

[5-3] S. Lowenthal and P. Chavel, "Reduction of the Number of Samples in Computer Holograms for Image Processing," Applied Optics, Vol. 13, pp. 718-720, 1974.

[5-4] P. Chavel and S. Lowenthal, "A Method of Incoherent Optical-Image Processing using Synthetic Holograms," J. Opt. Soc. Am., Vol. 66, pp. 14-23, 1976.

[5-5] W.H. Lee and M.O. Greer, "Matched Filter Optical Processor," Applied Optics, Vol. 13, pp. 925-930, 1974.

[5-6] M.J. Bastiaans, "A Generalized Sampling Theorem with Application to Computer-Generated Transparencies," J. Opt. Soc. Am., Vol. 67, pp. 1666-1671, 1977.

[5-7] F.A. Jenkins and H.E. White, Fundamentals of Optics, p. 465, McGraw-Hill, New York, 1957. We use the refractive indices of telescope crown.

[5-8] D. Kermisch, "Image Reconstructon from Phase Information Only," J. Opt. Soc. Am., Vol. 60, pp. 15-17, 1970

[6-1] S. Lowenthal and P. Chavel, "Reduction of the Number of Samples in Computer Holograms for Image Processing," Applied Optics, Vol. 13 pp. 718-720, 1974.

[6-2] P. Chavel and S. Lowenthal, "A Method of Incoherent Optical-Image processing using Synthetic Holograms," J. Opt. Soc. Am., Vol. 66, pp. 14-23, 1976.

[6-3] W.H. Lee and M.O. Greer, "Matched Filter Optical Processor," Applied Optics, Vol. 13, pp. 925-930, 1974.

[6-4] H. Bartelt, W.J. Dallas and A.W. Lohmann, "Computer Generated Spatial Filters for Large Object Formats," Optics Communications, Vol. 20, pp. 50-55, 1977.

[6-5] T. Yatagai, "Interpolation Method of Computer-Generated Filters for Large Object Formats," Optics Communications, Vol. 23, pp. 347-351, 1977.

[6-6] A. Vander Lugt, "Signal Detection by Complex Spatial Filtering" IEEE Trans. Inform. Theory, Vol. IT-10, pp. 139-145, 1964.

[6-7] B.R. Brown and A.W. Lohmann, "Complex Spatial Filtering with Binary Masks," Applied Optics, Vol. 5, pp. 967-969, 1966.

[6-8] A.W. Lohmann and D.P. Paris, "Binary Fraunhofer Holograms, Generated by Computer," Applied Optics, Vol. 6, pp. 1739-1748, 1967.

[6-9] A.W. Lohmann, "Matched Filtering with Self-Luminous Objects," Applied Optics, Vol. 7, pp. 561-563, 1968.

[6-10] A.W. Lohmann and H.W. Werlich, "Incoherent Matched Filtering with Fourier Holograms," Applied Optics, Vol. 10, pp. 670-672, 1971.

[6-11] B. Braunecker and A.W. Lohmann, "Character Recognition by Digital Holography," Optics Communications, Vol. 11, pp. 141-143, 1974.

[6-12] B. Braunecker, R. Hauck, and A.W. Lohmann, "Hybrid Image Processing," Photographic Science and Engineering, Vol. 21, pp. 278-281, 1977.

[6-13] B. Braunecker, R. Hauck and A.W. Lohmann, "Optical Character Recognition Baed on Nonredundant Correlation Measurements," Applied Optics, Vol. 18, pp. 2746-2753, 1979.

[6-14] J.W. Goodman, Introduction to Fourier Optics, McGraw-Hill, New York, 1968, pp. 177-184.

[6-15] A.W. Lohmann, "Several Optical Correlation Methods," Int. Opt. Comp. Conf., April 1975, Washington D.C., pp. 142-144.

[6-16] J.W. Wozencraft and I.M. Jacobs, Principles of Communication Engineering, Wiley, New York, 1965, pp. 242-244.

[6-17] A.A.Q. Kadkly, "Performance of Optical Matched Filters," Optica Acta, Vol. 26, pp. 461-482, 1979.

[6-18] J.T. Tippett, et al., (eds.), Optical and Electro-Optical Information Processing, MIT Press, Cambridge, Mass., 1965, pp. 125-141.

[6-19] R.A. Binns, A. Dickinson, and B.M. Watrasiewicz, "Methods of Increasing Discrimination in Optical Filtering," Applied Optics, Vol. 7, pp. 1047-1051, 1968.

[6-20] W.K. Pratt, Digital Image Processing, Wiley, New York, 1978, pp. 553-566.